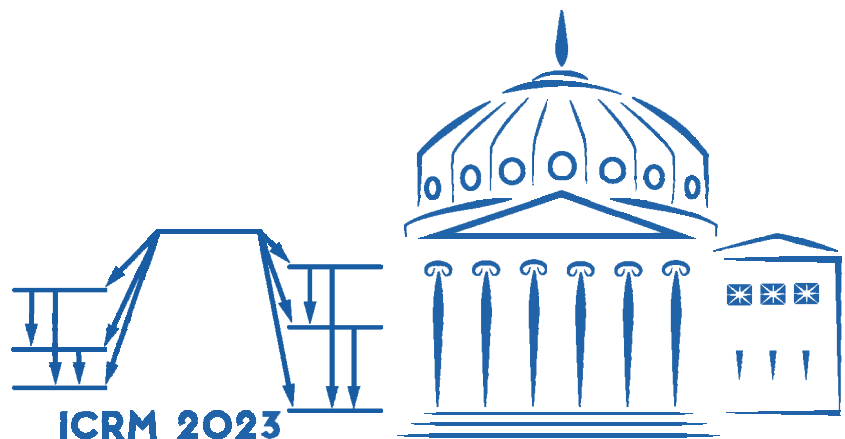**INTERNATIONAL COMMITTEE
FOR RADIONUCLIDE METROLOGY**

23rd International Conference on Radionuclide Metrology and its Applications (ICRM 2023) March 26-31, 2023, Bucharest, Romania

Editors

Aurelian Luca, Brian Zimmerman
and Denis Glavič-Cindro

ICRM 2023

23RD INTERNATIONAL CONFERENCE
ON RADIONUCLIDE METROLOGY
AND ITS APPLICATIONS

BUCHAREST
ROMANIA
26-31 MARCH 2023

The International Committee for Radionuclide Metrology (ICRM) is an association of radionuclide metrology laboratories whose membership is composed of delegates of these laboratories together with other scientists (associate members) actively engaged in the study and applications of radioactivity.

It explicitly aims at being an international forum for the dissemination of information on techniques, applications and data in the field of radionuclide metrology. This discipline provides a range of tools for tackling a wide variety of problems in numerous other fields, for both basic research and industrial applications. Radionuclide metrology continues to play an important role in the nuclear industry, supporting activities such as radionuclide production, nuclear medicine, measurement of environmental radioactivity and of radionuclides in food and drinking water, decommissioning of nuclear facilities, nuclear security and emergency preparedness, nuclear physics research, etc.

International Committee for Radionuclide Metrology (ICRM)
http://physics.nist.gov/ICRM/
Ljubljana, Slovenia

Contact information
Denis Glavič-Cindro
ICRM Secretary
E-mail: denis.cindro@ijs.si

Legal notice
Neither the International Committee for Radionuclide Metrology nor any person acting on behalf of the Committee is responsible for the use which might be made of this publication.

ICRM technical series on radionuclide metrology
ISSN 2522-4328
URL: https://physics.nist.gov/ICRM/ICRM_technicalseries_3.pdf

© International Committee for Radionuclide Metrology, 2024

Reproduction is authorised provided the source is acknowledged.

Contents

Proceedings of the
23rd International Conference on Radionuclide Metrology and its Applications (ICRM 2023), March 26-31, 2023, Bucharest, Romania

Editors: Aurelian Luca, Brian Zimmerman and Denis Glavič-Cindro

PREFACE

Aurelian Luca [1*], Brian Zimmerman [2], Denis Glavič-Cindro [3]

[1] *Horia Hulubei National Institute for R&D in Physics and Nuclear Engineering (IFIN-HH), DRMR Dept., Ionizing Radiation Metrology Laboratory (LMRI), Măgurele, Ilfov county, Romania, E-mail address*: aluca@nipne.ro

[2] *National Institute of Standards and Technology (NIST), Gaithersburg, MD, USA, E-mail address:* brian.zimmerman@nist.gov

[3] *Jožef Stefan Institute (IJS), Ljubljana, Slovenia, E-mail address:* denis.cindro@ijs.si

This third issue of the ICRM Technical Series on Radionuclide Metrology proceedings is devoted to the 23rd International Conference on Radionuclide Metrology and its Applications (ICRM 2023), organized during the period March 26-31, 2023, at the Radisson Blu Hotel, Bucharest, Romania, https://icrm2023.nipne.ro. Initially scheduled to be held in 2021, the conference was postponed to 2023 because of the Covid-19 pandemic. The local organisation was assured by the Horia Hulubei National Institute for Research and Development in Physics and Nuclear Engineering (IFIN-HH), http://www.nipne.ro. The coordination of the local organisation team was undertaken by the members of the Ionizing Radiation Metrology Laboratory (LMRI) from the Department of Radioisotopes and Radiation Metrology (DRMR). The conference venue, situated in downtown Bucharest, provided excellent facilities for the conference and the participants coming from 30 countries.

Radionuclide metrology brings together interdisciplinary research and development teams (physicists, chemists, biologists, mathematicians, engineers, etc.) with the main purpose of ensuring improved tools for the qualitative and quantitative characterization of the radionuclides. This work is important because radionuclide metrology has an impact on many applications for sustainable development: life sciences, climate change, environmental protection (clean air, water and soil; food safety), nuclear energy, ionizing radiation protection, radioactive waste management, and industry (new materials, radioactive standards, detectors etc.).

The International Committee for Radionuclide Metrology (ICRM), https://physics.nist.gov/ICRM/index.html, founded in Paris in 1974), is an association of radionuclide metrology laboratories represented by appointed delegates together with other scientists (associated members). The initiative of founding this international scientific association originates from the 1st International Summer School on Radionuclide Metrology, organized in 1972 at Herceg-Novi, Yugoslavia. More than 50 years later, an interesting article about this important event was published in the virtual special issue ICRM 2023 of Applied Radiation and Isotopes by Dr. Maria Sahagia (IFIN-HH, Romania) – one of the participants in this Summer School.

The ICRM promotes international collaboration in the field of radionuclide metrology. The membership of ICRM continues to increase: there were 46 institutional members at the time of ICRM 2023 conference. The biennial ICRM conferences, the ICRM Low Level Radionuclide Metrology Techniques (LLRMT) conferences (held every four years), the annual ICRM Working Groups meetings, and other actions, like training courses for young researchers, are open to all professionals (researchers, professors, engineers, technicians, etc.) and students interested in the radionuclide metrology and its applications. The previous ICRM conference was the 22nd International Conference on Radionuclide Metrology and its Applications (ICRM 2019), hosted by the University of Salamanca (Spain), during May 27-31, 2019, https://icrm.usal.es.

The 23rd International Conference on Radionuclide Metrology and its Applications (ICRM 2023) was the first ICRM conference organised in a hybrid format, with in-person participants and online participants. From the total number of 153 registered participants from 30 countries and 3 international organizations, 131 persons (about 85 % of the total number of participants) attended in-person the ICRM 2023 conference. Among the participants to ICRM 2023 there were experts from the Comprehensive Nuclear-Test-Ban Treaty Organization (CTBTO), the Bureau International des Poids et Mesures (BIPM) and the International Atomic Energy Agency (IAEA). During a specific conference session (Research in Industry) on Wednesday 29 March 2023, interesting presentations about some of the newest products available for the radionuclide metrology community were given by Gabriela Ilie (Mirion Technologies Inc., USA) and Matteo Corbo (CAEN SPA, Italy). The booths of these two companies, located in the coffee break area, allowed better interaction with the conference participants, presenting instruments and printed documents about their products and services. The online participants were not allowed to present papers at ICRM 2023, but they could follow all the invited and oral presentations broadcasted by ZOOM and ask questions using the chat facility. A few of the online participants had short presentations (by ZOOM) within the ICRM Working Group meetings. All the online participants received/downloaded the Abstract Book (pdf file) and other conference documents, and had online access to some of the posters provided by the authors.

From the total number of 111 abstracts submitted for the ICRM 2023 conference, 104 abstracts were accepted for ICRM 2023. During the conference, 97 papers were presented: 5 invited talks, 37 oral, and 55 poster presentations. Although 67 papers presented at the conference were accepted for submission to Applied Radiation and Isotopes, only about 70 % of these were submitted to the journal. The virtual special issue VSI:ICRM 2023 of Applied Radiation and Isotopes (see the Appendix) includes 40 articles, accepted after a rigorous reviewing process. Other papers presented at ICRM 2023 were published in Applied Radiation and Isotopes and Metrologia (not included in the special issue). Initially, there were 23 ICRM 2023 papers proposed to be published in the 3rd issue of the ICRM Technical Series on Radionuclide Metrology proceedings, but, in the end, nine papers were accepted for publication in the current issue after a peer-review process similar to the one for the papers published in Applied Radiation and Isotopes. This Preface includes the information presented in the Editorial of VSI:ICRM 2023, published by the same authors in Applied Radiation and Isotopes, volume 211, 2024, https://doi.org/10.1016/j.apradiso.2024.111385. The 3rd issue of the ICRM Technical Series on Radionuclide Metrology proceedings (2024) is posted on the ICRM website, https://www.physics.nist.gov/ICRM/ICRM_technicalseries_3.pdf (free download).

During the conference opening on Monday 27 March 2023, participants were welcomed by Dr. Nicolae Marius Mărginean, Director General of IFIN-HH, Dr. Aurelian Luca, Scientific Secretary of the Conference ICRM 2023 and by the ICRM President – Dr. Brian Zimmerman (Fig. 1). The scientific programme of the conference opened with an interesting invited talk by Dr. Maria Sahagia (IFIN-HH): *„Herceg-Novi Summer School, the starting point in the history of the International Committee for Radionuclide Metrology"*. The scientific programme continued with the first session of the conference – Aspects of International Metrology, and all the other sessions scheduled during five days, according to the conference agenda. The participants in the conference hall and the poster and coffee break area are presented in Fig. 2 and Fig. 3, respectively.

Fig. 1. Conference opening ceremony: Aurelian Luca, Scientific Secretary of ICRM 2023 (left), Brian Zimmerman, ICRM President (center) and Nicolae Marius Mărginean, Director General of IFIN-HH (right)

Fig. 2. Participants to ICRM 2023 in the conference hall

Fig. 3. Poster presentation and coffee break area at the ICRM 2023 conference

Two very important awards were presented on behalf of the journal Applied Radiation and Isotopes (ELSEVIER) by Dr. Denis Bergeron, Editor-in-Chief of Applied Radiation and Isotopes, during a special moment of the conference dinner on Wednesday 29 March 2023 (Fig. 4):

-the JARI MEDAL was awarded to Prof. Dr. Alan L. Nichols (University of Surrey, United Kingdom and Manipal Academy of Higher Education, India);

-the HUBBELL AWARD was granted to Dr. Xavier Mougeot (CEA/LNE-Laboratoire National Henri Becquerel, France).

Fig. 4. Alan L. Nichols (left) and Xavier Mougeot (right) presented the JARI Award 2023;
Hubbell Award 2023, respectively.

During the last day of the ICRM 2023 conference (Friday 31 March 2023) the traditional Best Poster Award, offered by the ICRM, was awarded to Ms. Yoonhee Jung (Korea Research Institute of Standards and Science (KRISS), Republic of Korea) for the poster no. P-42 entitled „Development of Reference

Material for Quality Control of Uranium Analysis in Marine Sediments". This poster was presented during the session Measurement Standards and Reference Materials (Fig. 5). The coauthors of the poster presentation were Sang-Han Lee and Min-Ju Lee (KRISS).

Fig. 5. The Best Poster Award was presented to Ms. Yoonhee Jung (KRISS, Republic of Korea)

On behalf of the management of IFIN-HH, Dr. Aurelian Luca presented a special award in memory of Dr. Leon Enric Grigorescu (1932-2020), founder of the Radionuclide Metrology Laboratory in IFIN-HH, more than 60 years ago. The LEON GRIGORESCU Award was presented to Dr. Maria Sahagia (Romania), Professor Emeritus Dr. Octavian Sima (Romania), Dr. Philippe Cassette (France) and Dr. Uwe Wätjen (Belgium).

Business meetings of all ICRM Working Groups were integrated in the conference programme. The General Meeting of the ICRM was organized on Friday 31 March 2023, during the afternoon.

The social programme of the conference included an informal reception and guided Bucharest city tour (Sunday 26 March 2023), guided visit at the Romanian Athenaeum on Monday 27 March 2023 (Fig. 6), Conference dinner (Wednesday 29 March 2023) and two optional visits to IFIN-HH / Extreme Light Infrastructure – Nuclear Physics (ELI-NP) and DRMR/Ionizing Radiation Metrology Laboratory on Tuesday 28 March 2023 and Thursday 30 March 2023 (Fig. 7). The conference dinner took place in Bucharest, at the Pescăruș restaurant from the King Michael I Park. A traditional Romanian music and dance show was presented by the professional folk dance ensamble Cindrelul – Junii Sibiului and entertained the dinner participants.

Fig. 6. Visit of the conference participants at the Romanian Athenaeum.

Fig. 7. Visit at IFIN-HH / ELI-NP on Thursday 30 March 2023

Special thanks are addressed to the editors and reviewers of the nine papers published in the current issue of the ICRM Technical Series on Radionuclide Metrology proceedings:

Editors: Steven Judge (retired from BIPM, UK), Michel Bruggeman (SCK-CEN, Belgium), Jeffrey Cessna (NIST, USA), Ryan Fitzgerald (NIST, USA), Christophe Bobin (CEA/LNE-LNHB, France), Marie-Christine Lépy (CEA/LNE-LNHB, France) and Lisa Karam (NIST, USA);

Reviewers: Lisa Karam (NIST, USA), Steven Judge (retired from BIPM, UK), Denis Glavič-Cindro (IJS, Slovenia), Michel Bruggeman (SCK-CEN, Belgium), Jeffrey Cessna (NIST, USA), Claude Bailat (IRA, Switzerland), Ryan Fitzgerald (NIST, USA), Sanghoon Hwang (KRISS, Republic of Korea), Marco Capogni (ENEA, Italy), Christophe Bobin (CEA/LNE-LNHB, France), Marie-Christine Lépy (CEA/LNE-LNHB, France), Octavian Sima (University of Bucharest; IFIN-HH, Romania), Virginia Peyres (CIEMAT, Spain), Simon Mark Jerome (NMBU, Norway) and Nuria Navarro (CIEMAT, Spain).

(a)

(b)

*Fig. 8. (a), (b) The Secretariat of the ICRM 2023 conference
and some members of the Local Organizing Committee from IFIN-HH*

At the present time, there are 47 institutions represented by delegates in the ICRM. There is no ICRM membership fee and no paid secretariat or other staff of the ICRM. Its overall direction is established by the delegates at General Meetings, which are held usually every two years. The delegates discuss and agree upon the organisational guidelines and directions for scientific and collaboration work programmes. During the ICRM General Meeting (GM) of 31 March 2023 in Bucharest, Romania, elections were organized for the ICRM President, two of the three Vice-Presidents, and the Secretary. After the General Meeting, the ICRM officers are the following:

President	Brian Zimmerman[1]
Vice-Presidents	Aurelian Luca[2]
	Carine Michotte[3]
	Raphael Galea[4]
Past President	Eduardo García-Toraño[5]
Secretary	Denis Glavič-Cindro[6]

---

[1] National Institute of Standards and Technology, 100 Bureau Drive, MS 8462, Gaithersburg, MD, 20899-8462, USA.

[2] Horia Hulubei National Institute for R&D in Physics and Nuclear Engineering, 30 Reactorului St., PO Box MG-6, Măgurele, Ilfov county, RO-077125, Romania.

[3] Bureau International des Poids et Mesures, Pavillon de Breteuil, F-92312, Sèvres Cedex, France.

[4] National Research Council of Canada – Ionizing Radiation Standards group, 1200 Montreal Road, Ottawa, K1A 0R6, Canada

[5] Centro de Investigaciones Energéticas, Medioambientales y Tecnológicas (CIEMAT), Avda. Complutense 40, Madrid 28040, Spain.

[6] Institut Jožef Stefan, Jamova 39, SI-1001 Ljubljana, Slovenia.

Most of the ICRM scientific activities are performed within its working groups (WG). Each working group is guided by a coordinator who acts as a centre for ideas and communications and has the possibility to organise conferences and workshops. There are now eight working groups with the following fields of interest and assigned coordinators:

(1) Radionuclide Metrology Techniques: Ryan Fitzgerald[1], Christophe Bobin[7], Steven Bell[8], Ole Nähle[9]

(2) Alpha-Particle Spectrometry: Stefaan Pommé[10]

(3) Gamma-Ray Spectrometry: Marie-Christine Lépy[7]

(4) Life Sciences: Jeffrey T. Cessna[1]

(5) Liquid Scintillation Counting: Karsten Kossert[9]

(6) Low-Level Measurement Techniques: Begoña Quintana Arnés[11] until December 2023, then Daniel Zapata[9]

(7) Beta-Particle Spectrometry: Xavier Mougeot[7]

(8) Nuclear Decay Data: Mark Kellett[7].

We express our thanks to Prof. Dr. Begoña Quintana Arnés (University of Salamanca, Spain), who coordinated the Low-Level Measurement Techniques WG during the period 2019-2023, with important contributions, including her involvement in the excellent organization of the ICRM Low-Level Radioactivity Measurement Techniques international conference (ICRM LLRMT 2022), which was held during May 2-6, 2022, in Assergi, Italy, https://icrm2022.lngs.infn.it.

The 11 scientific sessions of the ICRM 2023 conference were established according to the ICRM WGs mentioned above: Aspects of International Metrology, Quality Assurance and Proficiency Tests, Radionuclide Metrology in Life Sciences, Alpha- and Beta-Particle Spectrometry, Radionuclide Metrology Techniques, Gamma-Ray Spectrometry, Measurement Standards and Reference Materials, Source Preparation Techniques, Liquid Scintillation Counting Techniques, Nuclear Decay Data and Low Level Radioactivity Measurement Techniques.

Anyone wishing to participate to the different scientific activities of the ICRM or to receive more information about the ICRM can contact one or several of the ICRM officers mentioned above. Information about the ICRM and its Working Groups is available on the ICRM website: http://physics.nist.gov/icrm

The next ICRM conference (ICRM 2025) will be held in Paris, France, during the period May 19-23, 2025 and will be organized by the Laboratoire National Henri Becquerel (CEA/LNE-LNHB, Saclay, France). More information is available on the conference website https://icrm2025.org/. The people interested by this conference can also write to Dr. Mark A. Kellett – Scientific Secretary of ICRM 2025 and Chair of the Local Organizing Committee ICRM 2025 at the e-mail address mark.kellett@cea.fr. The Conference Secretariat can be contacted by e-mail at ICRM2025@cea.fr. For the 24th edition of the ICRM conference (ICRM 2025), we address our best wishes to the organizers and participants, with excellent scientific achievements, nice moments in the City of Lights and hope for the future of the ICRM. We are looking forward to meet you in Paris next year!

---

[7] CEA, LIST, Laboratoire National Henri Becquerel (LNE-LNHB), F-91191 Gif-sur-Yvette Cedex, France.
[8] National Physical Laboratory, Hampton Road, Teddington, Middlesex, TW11 0LW, UK.
[9] Physikalisch-Technische Bundesanstalt, Budesallee 100, D-38116 Braunschweig, Germany.
[10] European Commission, Joint Research Centre, Retieseweg 111, B-2440 Geel, Belgium.
[11] Laboratorio de Radiaciones Ionizantes-Datación, Universidad de Salamanca, Salamanca, Spain

Fig. 9. ICRM 2023 Conference Group photo in the conference hall at the Radisson Blu hotel in Bucharest, Romania.

Scientific Committee ICRM 2023 (alphabetical order)
Pablo Arenillas, CNEA, Argentina
Dirk Arnold, PTB, Germany
Steven Bell, NPL, UK
Christophe Bobin, LNE-LNHB, France
Michel Bruggeman, SCK·CEN, Belgium
Marco Capogni, ENEA, Italy
Philippe Cassette (Sofia Univ. St. Kliment Ohridski, Bulgaria)
Jeffrey Cessna, NIST, USA
Sean Collins, NPL, UK
Romain Coulon (BIPM, International)
Pierino De Felice, ENEA, Italy
Andrew Fenwick, NPL, UK
Ryan Fitzgerald, NIST, USA
Raphael Galea, NRC·CNRC, Canada
Eduardo García-Toraño, retired from CIEMAT, Spain
Denis Glavič-Cindro, IJS, Slovenia
Yoshio Hino, NMIJ/AIST, Japan
Mikael Hult, EC-JRC, EU
Simon Mark Jerome, NMBU, Norway
Steven Judge, retired from BIPM, International
Lisa Karam, NIST, USA
John Keightley, NPL, UK
Mark Kellett, LNE-LNHB, France
Matjaž Korun, retired from IJS, Slovenia
Karsten Kossert, PTB, Germany
Marie-Christine Lépy, LNE-LNHB, France
Haoran Liu, NIM, China
Aurelian Luca, IFIN-HH, Romania
Franz Josef Maringer, BOKU, Austria
Carine Michotte, BIPM, International
Xavier Mougeot, LNE-LNHB, France
Ohle Jens Nähle, PTB, Germany
Nuria Navarro, CIEMAT, Spain
Virginia Peyres, CIEMAT, Spain
Stefaan Pommé, EC-JRC-Geel, EU
Begoña Quintana Arnés, U. Salamanca, Spain
Miguel Roteta, CIEMAT, Spain
Octavian Sima, Univ. Bucharest, Romania
Freda van Wyngaardt, ANSTO, Australia
Akira Yunoki, NMIJ/AIST, Japan
Brian Zimmerman, NIST, USA.

Program Committee ICRM 2023
Dirk Arnold, PTB, Germany
Christophe Bobin, LNE-LNHB, France
Michel Bruggeman, SCK·CEN, Belgium
Jeffrey Cessna, NIST, USA
Pierino De Felice, ENEA, Italy
Ryan Fitzgerald, NIST, USA
Raphael Galea, NRC·CNRC, Canada
Eduardo García-Toraño, retired from CIEMAT, Spain
Denis Glavič-Cindro, IJS, Slovenia
Mikael Hult, EC-JRC, EU
Simon Mark Jerome, NMBU, Norway
Steven Judge, retired from BIPM, International
Lisa Karam, NIST, USA
John Keightley, NPL, UK
Mark Kellett, LNE-LNHB, France
Karsten Kossert, PTB, Germany
Marie-Christine Lépy, LNE-LNHB, France
Aurelian Luca, IFIN-HH, Romania
Franz Josef Maringer, BOKU, Austria
Carine Michotte, BIPM, International
Xavier Mougeot, LNE-LNHB, France
Stefaan Pommé, EC-JRC-Geel, EU
Begoña Quintana Arnés, U. Salamanca, Spain
Uwe Wätjen, retired from EC-JRC, Belgium
Brian Zimmerman, NIST, USA.

Coordinating referees:
Christophe Bobin, LNE-LNHB, France
Michel Bruggeman, SCK·CEN, Belgium
Jeffrey Cessna, NIST, USA
Ryan Fitzgerald, NIST, USA
Steven Judge, BIPM (retired), International
Lisa Karam, NIST, USA
Mark Kellett, LNE-LNHB, France
Karsten Kossert, PTB, Germany
Marie-Christine Lépy, LNE-LNHB, France
Stefaan Pommé, EC-JRC-Geel, EU
Begoña Quintana Arnés, U. Salamanca, Spain.

Transfer of developed pre-selection and free-release technology to decommissioning industries

Arūnas Gudelis[a], Petr Kovar[b], Jiri Suran[b], Virginia Peyres[c], Jose Carlos Saez Vergara[c], Lukas Skala[d], Tomas Grisa[d]

[a] FTMC, Lithuania
[b] CMI, Czech Republic
[c] CIEMAT, Spain
[d] NUVIA, Czech Republic

Abstract

Within the EURAMET JRP 16ENV09 project 'MetroDecom II', a pre-selection and free-release measurement facility was constructed for waste materials arising from decommissioning activities; operational, measurement, calibration and evaluation software were also prepared. A new project, 20SIP02, has been proposed that takes into consideration the needs related to outputs of the former MetroDecom II project. It provides results which enable 1) transferring the new technology and knowledge to a commercial business and 2) bringing the developed facility to a wide international market and for adoption by a large community of end-users.

Keywords: nuclear decommissioning; free release measurement facility; radioactive waste management; low-activity concrete

* Corresponding author, e-mail address: arunas.gudelis@ftmc.lt

1. Introduction

The first generation of nuclear power plants and reprocessing facilities are coming to the end of their working lives. The aim of the decommissioning process is to clear the site, while minimizing the risk to the public and the environment from the hazardous waste arising. Two essential steps in the decommissioning process are pre-selection of wastes to a repository or, potentially, free release to the environment, which requires careful measurements to verify free release criteria are met. These needs are set out in the EU Council Directive 2011/70/EURATOM, and new measurement techniques are needed to improve safe and effective management of radioactive wastes and overcome issues existing commercial systems have, e. g. low throughput, expensive lead shielding, insufficient sensitivity and uncertainty.

The overall aim of JRP 16ENV09 'MetroDecom II – In-situ metrology for decommissioning nuclear facilities' is to provide the metrology for decommissioning nuclear facilities. The project addresses achieving traceability to primary standards of activity of radionuclides and validating the calculation methods used for activity determination of radionuclides occurring in wastes either stored in radioactive waste repositories or free released to the environment.

Within the JRP 16ENV09 project, a new pre-selection and free-release measurement facility, with the flexibility of moveable detectors, was constructed and put into operation. Measurement, calibration and evaluation software were developed.

2. Design of the facility

One requirement for the facility was special modular shielding material made from a concrete with a low natural radionuclide content, to minimize the background radiation inside the measuring chamber of the facility and to lower the detection limits. Concrete segments (Fig. 1) were constructed, consisting of an aggregate of specific rock containing low amounts of natural radioactivity, and a special cement based on very old (pre-nuclear age) sediments from the bottom of the sea. The activity concentrations of natural radionuclides are about one order of magnitude lower than usual, thus lowering the background radiation inside the shielding significantly. The modular design allows flexibility and convenience in applications: shielding facilities can be constructed easily without having to pour concrete; it is possible to build large

facilities quickly and optimize them for an individual decommissioning site; it is easy to dismantle such facilities and reuse the segments at other sites; and the detector array and electronics can be set up within the shielded chamber (Suran et al., 2017).

Fig. 1: Low-activity concrete bricks developed for shielding. Typical activities are ^{226}Ra ≈ 0.6 Bq/kg, ^{228}Th ≈ 0.3 Bq/kg and ^{40}K ≈ 6 Bq/kg.
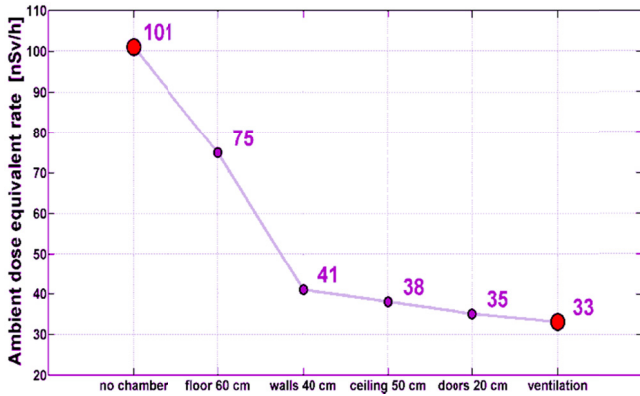
Fig. 2: Background ambient dose equivalent rate in the measuring chamber at different stages of construction.

Fig. 2 shows a decrease in the dose rate from a typical external natural background of about 100 nSv/h to a background of 33 nSv/h inside the chamber of the free-release measurement system at different stages of its construction. Fig. 3 shows a comparison of the background gamma-ray spectrum acquired by a high-purity germanium (HPGe) coaxial detector with a resolution (FWHM) of 1.8 keV and relative efficiency of 50 % for ^{60}Co (1332.5 keV) inside the shielded chamber and outside the chamber, without shielding, in the same position.
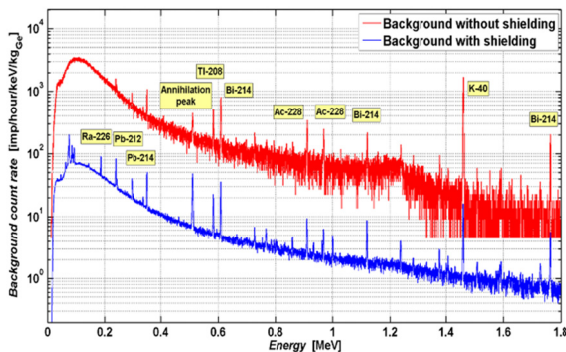

Fig. 3: Background with and without shielding (HPGe spectra).

A detailed Monte Carlo model of the facility was developed so that the geometry and parameters could be optimized (Solc et al., 2014, 2017) and validated (Solc et al., 2016; Suran et al., 2018; Peyres et al., 2021). The model takes into consideration the detectors and their collimators, the shielding blocks, the mechanical parts of the chamber, the hall parameters (e.g., content of radionuclides in the floor, ceiling, and walls), the natural background at the site, the natural radionuclide content in the air, the parameters of the measured material and the container in which it is placed. This construction allows the dimensions of the shielding segment, called the "tunnel," to have the following dimensions: 300 cm length, 140 cm inner width, 240 cm inner height (Solc et al., 2017).

The detector array consists of Stirling-cycle cooled gamma-ray spectrometric compact modules (typical detection efficiencies are shown in Fig. 4), plastic scintillators total gamma-ray modules and neutron modules. Detector arrays can be optimized for specific uses by integrating the individual detectors separately in the array or removing them if needed. New certified calibration and testing standard sources and reference materials were used to facilitate accurate, traceable measurement. Different standards and reference materials were prepared for the purposes of calibration, stability checking and verification of the Monte Carlo models (Suran et al., 2017). Using the MCNPX code, a Monte Carlo model was created for each measurement geometry and the full-energy peak efficiency

calculated as a function of photon energy. The model was validated using standard cylindrical sources for hot-spots, and reference materials representing metal wastes, building materials, and light materials, for homogeneous waste material. All the calibration sources and reference materials were traceable to national measurement standards.
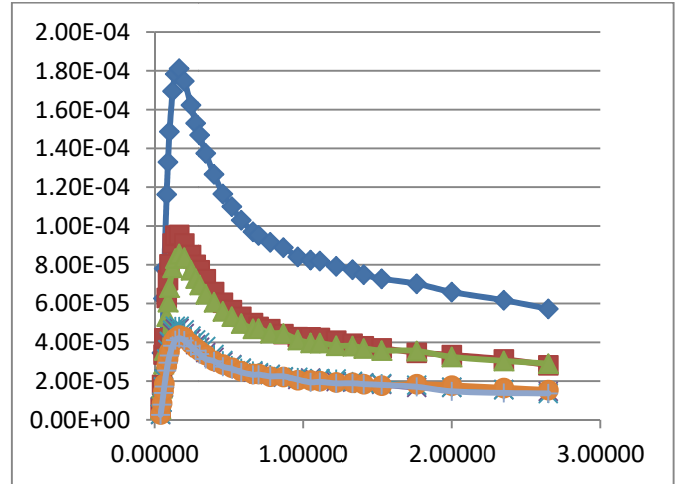
Fig. 4: Full-energy peak efficiencies for individual HPGe detectors, sum of 2 lower detectors, sum of 2 upper detectors and sum of 4 detectors. Energy on the X-axis is in MeV.
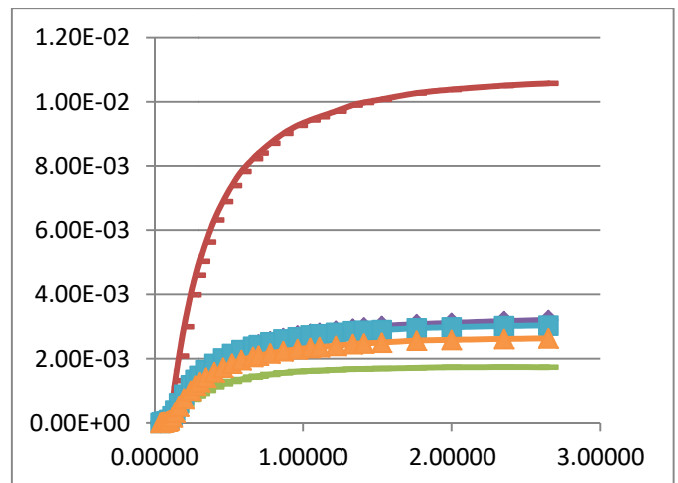
Fig. 5: Total efficiencies for individual plastic scintillation detectors and sum of 4 detectors. Energy on the X-axis is in MeV.

During the decommissioning process radioactive wastes are grouped according to their radionuclide content and the level of radioactivity. Pre-selection measurement is done to segregate waste into two streams, (i) those that cannot be released into the environment, and (ii) those that can be potentially released after a free release measurement. One application of the facility is to enable this segregation so that higher activity wastes go on for further analysis and lower activity wastes can be freely released. For radioactive waste segregation purposes, non-spectrometric plastic scintillator detectors (efficiencies shown in Fig. 5) employed as high, narrow prisms (Suran et al., 2017) to allow the optimization of their number and positions to be usually sufficient. Four detectors of the same type are used to ensure optimal detection geometry. In this way, it is possible to scan the containers in order to check the homogeneity of their radionuclide content and the presence of hot spots, with high measurement sensitivity (Suran et al., 2017).

During decommissioning, low-density materials (for example, filters, wood, fabric, paper) and high-density materials (e.g.,

concrete, graphite, steel tubes, wires, other metallic construction materials) are measured. The measurement systems currently available have fixed detector positions, so they cannot be optimized to measure lower amounts of high-density materials or higher amounts of low-density materials. In this new facility, upper detectors are mounted on a movable platform. Threaded bars and laser sensors ensure the vertical movement of the upper detector positions, so it is possible to measure two containers with a low-density material at the same time or one container with a high-density material in close measurement geometry (Suran et al., 2017). The other major differences with commercial units are: (i) unique shielding, (ii) unique arrangement of detectors, (iii) efficiency calibration for a wide range of types of waste, and (iv) comprehensive, flexible analysis software. With this array, detection limits below 1 Bq/kg were reached (^{60}Co and ^{137}Cs) for 100 s live time measurement of materials such as plastics, gravel and steel pipes.
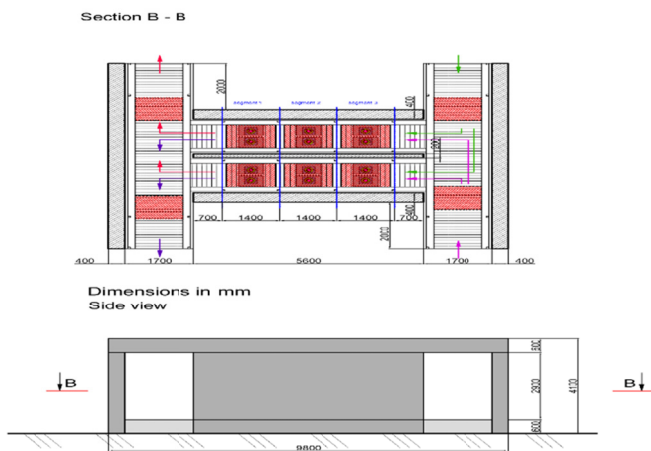

Fig. 6: The number of measurement modules can be chosen depending on the amount of waste to be measured. The diagram shows a typical six-module configuration.

Experience with the prototype system resulted in a fully modular concept for the industrial system shown in Fig. 6, permitting optimization based on the needs of individual decommissioning sites.

3. Conclusions and next steps

The work undertaken in the MetroDecom II project described in this paper provided results that will enable the technology and knowledge to be transferred to a commercial business, bringing the facility to a wide international market and a wide range of end users. The follow-on 20SIP02 project will result in reporting on the modification of pre-selection and free-release measurement facility for different types of nuclear facilities, and national and European legislations. Moreover, results of the project will enable detailed description of pre-selection and free-release measurement facility for different types of end-user, identified during the project taking into account specific peculiarities such as required throughput, types of wastes, radionuclides of interest, pre-selection and free release criteria, and legislative requirements.

Acknowledgement

References

Peyres, V., Marijuan, M.J., Šuran, J., Šolc, J., Kovar, P., Skala, L., Grisa, T., Gomez Caloca, C., Saez Vergara, J.C., 2021. Validation of a free release measurement facility on a decommissioning site. Appl. Radiat. Isot. 178, 109968.

Šolc, J., Kovar, P., Šuran, J., Peyres, V., Garcia-Toraño, E., 2014. Optimization of a measurement facility for radioactive waste free release by Monte Carlo simulation. Appl. Radiat. Isot. 87, 348-352.

Šolc, J., Kovar, P., Dryak, P., 2016. Validation of Monte Carlo model of HPGe detector for field-station measurement of airborne radioactivity. J. of Instr. 11, P03015.

Šolc, J., Kovar, P., Šuran, J., Grisa, T., 2017. Monte Carlo optimization of shielding for novel industrial free release measurement facility. Appl. Radiat. Isot. 126, 73-75.

Šuran, J., Kovar, P., Smoldasova, J., Šolc, J., Skala, L., Arnold, D., Jerome, S., de Felice, P., Pedersen, B., Bogucarska, T., Tzika, F., Van Ammel, R., 2017. New high-throughput measurement systems for radioactive wastes segregation and free release. Appl. Radiat. Isot. 130, 252-259.

Šuran, J., Kovar, P., Smoldasova, J., Šolc, J., Van Ammel, R., Garcia Miranda, M., Russell, B., Arnold, D., Zapata-Garcia, D., Boden, S., Rogiers, B., Sand, J., Perajarvi, K., Holm, P., Hay, B., Failleau, G., Plumeri, S., Beck, Y.L., Grisa, T., 2018. Metrology for decommissioning nuclear facilities: Partial outcomes of joint research project within the European Metrology Research Program. Appl. Radiat. Isot. 134, 351-357.

Proficiency Tests for Taiwanese Laboratories That Perform Low- and Intermediate-Activity Radio-Assays

Wan-Tzu Hung[*1,2], Wei-Han Chu[1,2], Yu-Tien Tsai[1], Pei-Lin Chung[1], Ming-Chen Yuan[1],

Rong-Jiun Sheu[2]

1 Department of Radiation Protection, National Atomic Research Institute, 1000 Wenhua Rd.

Jiaan Village, Longtan District, Taoyuan City 32546, Taiwan (ROC)

2 Institute of Nuclear Engineering and Science, National Tsing-Hua University, 101, Sec. 2, Kuang-Fu Road, Hsinchu, Taiwan

Abstract

This study reviewed the results of proficiency tests (PTs) conducted between 2013 and 2021 by the National Radiation Standard Laboratory of Taiwan for Taiwanese laboratories that perform low- and intermediate-activity radio-assays. The evaluated factors included the concentrations of gamma-emitting radionuclides, H-3, gross beta, and Sr-90 radioactivity, as well as the Sr-89/Sr-90 and Fe-55/Fe-59 radioactivity ratios. The results indicated that most of the assessed laboratories passed the PTs.

Keywords: Taiwan Accreditation Foundation; proficiency test; difficult-to-measure radionuclide; gamma radionuclide analysis; H-3 analysis; gross beta analysis; Sr-90 analysis; Sr-89/Sr-90 analysis

* Corresponding author, e-mail address: romanayaya@nari.org.tw

1. Introduction

Examining the performance of laboratories that perform low- and intermediateactivity radio-assays is crucial. Currently, seven laboratories in Taiwan have received accreditation from the Taiwan Accreditation Foundation (TAF) to perform radioactivity assays. The TAF provides accreditation on the basis of evaluations conducted by the National Radiation Standard Laboratory (NRSL) of the National Atomic Research Institute in Taiwan. An evaluation based on proficiency tests (PTs) is part of the accreditation procedure, which is performed for each laboratory tri-annually. In PTs, technical capability and quality control are assessed according to the criteria of the Ionizing Radiation Protection Act established by the Atomic Energy Council, Executive Yuan, Taiwan. Between 2013 and 2021, the NRSL conducted four proficiency testing programs for low- and intermediate-activity radio-assays according to the relevant technical criteria for radionuclides in the TAF-CNLA-T10(3) guidelines (TAF, 2018). The assessments in these programs adhered to the ANSI/HPS N42.22 (ANSI/HPS, 2002) and the ISO/IEC 17025 (ISO/IEC, 2017) standards.

The testing results obtained by the NRSL were used to determine the suitability of the analysis methods that are currently used in accredited radio-assay laboratories in Taiwan. These results and relevant feedback provided by the NRSL can be used by the assessed laboratories to improve their testing methods. Laboratories that pass the PTs are encouraged to apply for the ISO/IEC 17025 accreditation or for reaccreditation by the TAF.

2. Materials

The NRSL conducted PTs by sending suitable samples to the seven laboratories accredited by the TAF.

2.1 TAF-CNLA-T10(3) guidelines

2.1.1 Radionuclides analysis

The following analyses were conducted in the aforementioned seven laboratories:

(1) Analysis of gamma-ray emitters
(2) H-3 analysis
(3) Gross beta analysis
(4) Sr-90 analysis
(5) Sr-89/Sr-90 mixture analysis
(6) Fe-55/Fe-59 mixture analysis

2.1.2 Testing

Each laboratory performed two to five measurements for each sample according to its standard operation procedures. The minimum detectable activity (MDA) for each radionuclide needed to be lower than the predefined acceptable MDA (AMDA). The measurement results were evaluated on the basis of the resolution and zeta score (ζ-score). Moreover, the laboratories were requested to report the standard measurement uncertainty (see Section 2.1.3).

2.1.3 Standard measurement uncertainty

The standard measurement uncertainty for each analysis needed to be lower than 10%, and the uncertainty was evaluated according to the Joint Committee for Guides in Metrology (JCGM) 100:2008 standard of evaluation of measurement data—Guide to the expression of uncertainty in measurement.

2.1.4 Resolution

The resolution (R) is defined as follows:

$$R = \frac{A_s}{u_s} \qquad (1)$$

where A_s is the reference activity concentration of a specific radionuclide and where u_s is the standard measurement uncertainty ($k = 1$) for the reference activity derived by the NRSL.

The ratio of the activity value obtained by a laboratory (A_t) to the corresponding A_s value is called the measurement ratio (A_t/A_s). Table 1 presents the acceptable ranges of the measurement ratio for multiple resolutions.

Table 1: Acceptable ranges of the measurement ratio for multiple resolutions.

Resolution (R)	Range of acceptable measurement ratio
<4	0.4-2.5
4-7	0.5-2.0
8-15	0.6-1.66
16-50	0.75-1.33
51-200	0.8-1.25
>200	0.85-1.18

2.1.5 ζ-score

The absolute ζ-score is defined as follows:

$$\zeta = \frac{|A_t - A_s|}{\sqrt{u_t^2 + u_s^2}} \qquad (2)$$

where A_t is the activity value reported by a laboratory, A_s is the reference activity provided by the NRSL, u_t is the standard uncertainty of A_t, and u_s is the standard uncertainty of A_s when the coverage factor (k) is equal to 1.

According to the American National Standards Institute (ANSI) N42.22 (ANSI, 2002) guidelines, successful verification by the National Institute of Standards and Technology (NIST) in Taiwan is achieved when the difference between the NIST value and the test value is less than the propagated uncertainty of the difference under a k value of 3 and a 99% confidence level.

Consequently, absolute ζ-scores lower than 3 were considered acceptable in the tests of the NRSL.

2.1.6 Testing procedure

The PT programs were executed according to the procedure illustrated in Fig. 1. After all the samples were prepared and packed in NRSL, their surface dose rates were determined using the AT1121 detector. The dose rate was found to be lower than 1 μSv/h for all the samples.

The laboratories that were assessed by the NRSL provided the following data before the reporting deadline:

(1) Sample category
(2) Background or blank sample
(3) Counting time
(4) Activity correction for decay
(5) Standard measurement uncertainty (k = 1), including uncertainty of the radioactivity of the standard
(6) Reference date
(7) Brief description of analysis instrument or detector
(8) Analysis method

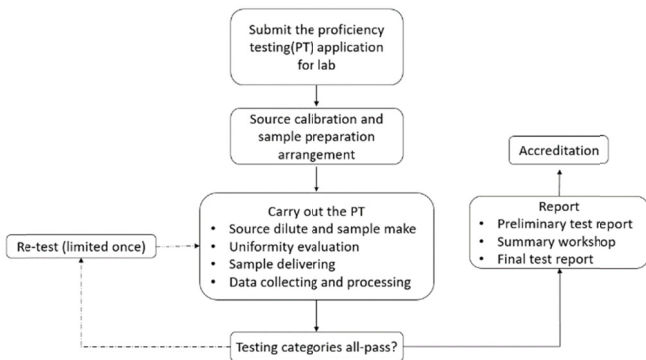**Figure 1:** Procedure for proficiency testing by the NRSL.

2.2 Determination of the radionuclides activity

The radioactivity of the test samples was 10 times higher than the AMDA. The reference activity values were determined using the following steps:

(1) Gamma radionuclides were calibrated using a 4πγ ion chamber at the NRSL.
(2) And the activities of the radionuclides should be traceable to the national measurement standard or the manufacturer of the original equipment.

2.3 Sample preparation

After source calibration was completed, NRSL diluted the prepared samples through the double-weighing method by using an electronic balance, and we ensured that the mass bias between every balance was included in the determination of the standard measurement uncertainty.

2.4 Sample measurements

Each laboratory assessed the received samples in accordance with its standard operating procedures. All the samples except for those containing difficult-to-measure (DTM) radionuclides had a mass of approximately 5 g.

2.4.1 Mixed gamma emitters

The gamma-ray spectrum of the sample was measured using an HPGe detector with a multichannel analyzer (MCA), and the sample was placed at a distance of 30 cm from the detector. The radioactivity for each radionuclide was calculated on the basis of the measured counting rate and the detection efficiency for the specified geometry.

2.4.2 H-3 samples

After the samples were mixed with scintillation cocktail, they were evaluated directly through liquid scintillation counting (LSC).

2.4.3 Fe-55/Fe-59 mixtures

Each sample was purified using anion exchange resins and preconcentrated through evaporation. The radioactivity of Fe-59 was evaluated using the HPGe detector with the MCA, and the radioactivity of Fe-55 was evaluated through LSC. In addition, the recovery rate was obtained through inductively coupled plasma optical emission spectrometry (ICP-OES).

2.4.4 Sr-89/Sr-90 mixtures

Strontium purification was performed using resin-packed columns, and the solution was analysed with LSC to evaluate the radioactivity of Sr-89 and Sr-90. The recovery rate was determined through ICP-OES analyses. Blind samples of Sr-89/Sr-90 mixtures are shown in Fig. 2.

Figure 2: Blind samples of Sr-89/Sr-90 mixtures.

2.4.5 Mixtures with DTM radionuclides

Arising from requirements related to the decommissioning of a nuclear power plant, the NRSL included the analysis of DTM radionuclides in its radioactivity analysis procedure in 2021. In the present study, we selected Ni-63, Tc-99, and Am-241 as DTM radionuclides. Because the laboratories were not accustomed to measuring these radionuclides, they were provided with three standard sources (20 g per bottle), as shown in Fig. 3. The massic activities of the reference DTM radionuclide s are listed in Table 2.
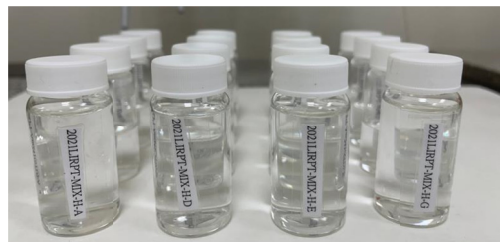

Figure 3: Standard and blind samples of the DTM radionuclides.

Table 2: Massic activities of reference DTM radionuclides

DTM	Massic activity (Bq/g, k=1)	Reference date
Ni-63	1,051±1.2%	
Tc-99	816±1.6%	2021/8/1 13:00
Am-241	801.1±0.56%	

A total of 1 g of each sample was preprocessed in multiple ways (as mentioned below) to prepare test samples. The processing of the Ni-63 samples is described as follows. A liquid mixture was prepared, and this mixture was then separated through precipitation. Subsequently, the sample was analysed with LSC and ICP-OES to obtain its activity and recovery rate, respectively.

The processing for the Tc-99 liquid samples is described as follows. The prepared sample was washed and separated using TEVA resin. Subsequently, the sample was analysed with LSC to determine its activity.

The processing for the Am-241 samples is described as follows. The relevant solution was electroplated on a stainless-steel sheet, and the radioactivity was then determined through alpha-particle spectrometry after the sample was purified using a highly selective Eichrom TRU resin.

3. Results and discussion

The PT procedure illustrated in Fig. 1 show the crucial steps in the accreditation procedure for radio-assay laboratories in Taiwan. The reference radioactivity values for the target radionuclides were determined by considering all the testing items and practical testing conditions of radionuclides.

We estimated that the source uniformity of the samples was within 3%. We used the TAF-CNLA-T10(3) criteria to analyze whether the results of each laboratory passed the PTs. The resolution values obtained by the laboratories were in the range 0.85–1.18 (Fig. 4). Moreover, for all the laboratories, approximately 99% of the ζ-scores were below 3 (Fig. 5), with the standard measurement uncertainty (k = 1) being less than 10% (Fig. 6). Because 99% of the aforementioned results met the relevant criteria, most of the laboratories passed the PTs. The radioactivity evaluation for the blind samples indicated an agreement between the laboratory-reported values and reference values.
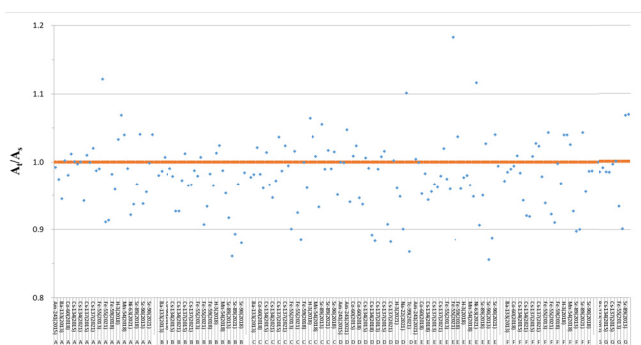
Figure 4: Ratio of the testing value (A_t) to the reference value (A_s).
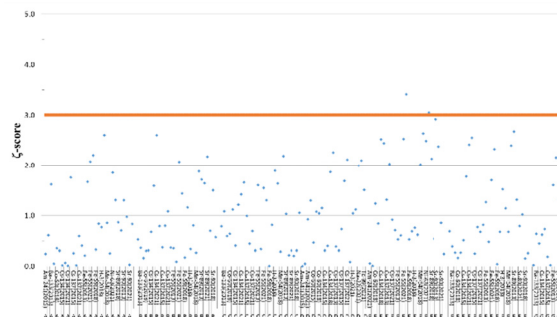
Figure 5: ζ-scores for all the laboratories.
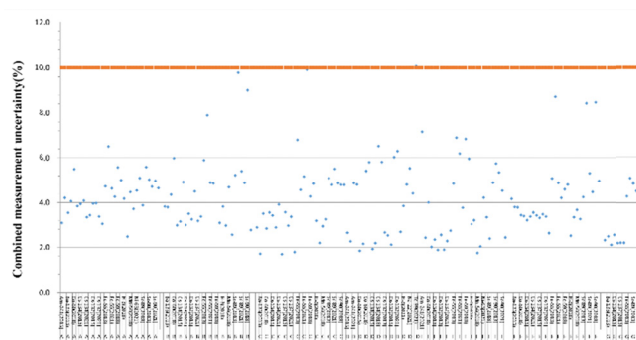
Figure 6: Measurement uncertainties for all the laboratories.

4. Conclusion

Over the preceding decade, the NRSL has been conducting PTs for laboratories accredited by the TAF that perform low- and intermediate-activity radio-assays. The PTs conducted by the NRSL in 2021 indicated radionuclide the technical capability of each of these laboratories. According to the results of these tests, 98.9% of the test criteria were satisfied; thus, most of the assessed laboratories passed the PTs. The next round of PTs is scheduled for 2024, with the focus being on radio-assay tests that are applicable in the decommissioning of nuclear power plants.

References

TAF-CNLA-T10(3): Technical criterion for accreditation of low and intermediate radio-assay level radionuclide analysis in the testing field, 2018.
ANSI/HPS N42.22, 2002. American National Standard - Traceability of Radioactive Sources to the National Institute of Standards and Technology (NIST) and Associated Instrument Quality Control
ISO/IEC 17025:2017. General requirements for the competence of testing and calibration laboratories
ISO/IEC 17043.2023. Conformity assessment-general requirements for proficiency testing.
(https://www.iso.org/standard/29366.html)
JCGM 100:2008, Evaluation of measurement data – Guide to the expression of uncertainty in measurement, BIPM.

Interlaboratory comparison of the results of food radiation testing in Taiwan

Wei-Han Chu[*1,2], Wan-Tzu Hung[1,2], Yu-Tien Tsai[1], Pei-Lin Chung[1], Ming-Chen Yuan[1],

Rong-Jiun Sheu[2]

1 Department of Radiation Protection, National Atomic Research Institute, 1000 Wenhua Rd.

Jiaan Village, Longtan District, Taoyuan City 32546, Taiwan (ROC)

2 Institute of Nuclear Engineering and Science, National Tsing-Hua University, 101, Sec. 2, Kuang-Fu Road, Hsinchu, Taiwan

Abstract

Since the Fukushima nuclear accident, food-safety has attracted increasing attention in Taiwan. Accurately detecting activity is crucial for ensuring food-safety. In this study, the food radiation testing results of eight laboratories accredited by the Taiwan Accreditation Foundation were compared according to the MOHWO0015.00 and ISO 17043 standards to examine the consistency. A total of 98% of ζ scores were found to be under 2, with the average measured activity being 1.02 ± 0.08 ($k = 1$) times the reference value.

Keywords: activity in food; Taiwan Accreditation Foundation; interlaboratory comparison; ISO 17043

* Corresponding author, e-mail address: weihan@nari.org.tw

1. Introduction

Food safety has become a major concern in Taiwan since the occurrence of the Fukushima nuclear accident in March 2011. Detecting radioactive substances in food is essential for ensuring food safety. Currently, eight food radiation testing laboratories in Taiwan are accredited according to the ISO/IEC 17025:2017 standard by the Taiwan Accreditation Foundation. These laboratories mainly analyze radionuclides such as I-131, Cs-134, and Cs-137 with activities ranging from 1 Bq/kg to 100 kBq/kg according to the MOHWO0015.00 standard of the food safety law (Method of Test of Radionuclides in Foods) established by the Ministry of Health and Welfare of Taiwan (2016).

In the present study, samples that were subjected to food radiation testing at the National Radiation Standard Laboratory (NRSL) of the National Atomic Research Institute of Taiwan were sent to the aforementioned eight laboratories to examine the consistency between their testing results.

The results from each laboratory were assessed, the food radiation testing capability of each laboratory was reviewed, and whether revisions were required in testing methods was determined. Food safety in Taiwan can be ensured if the aforementioned eight laboratories provide accurate and consistent results.

2. Materials

Food samples with different radionuclide massic (or specific) activity were prepared and sent to each of the laboratories participating in this study. Each laboratory was required to test the provided samples in accordance with the method specified in the MOHWO0015.00 standard (Table 1). This method is suitable for analyzing the massic activities of I-131, Cs-134, and Cs-137 in food (solid and liquid). Three matrices are introduced, they are milk (or milk products), soft drink (or bottled water), and infant foods, respectively. The method is divided into the following stages:

(1) Screening: An HPGe detector with a multichannel analyzer (MCA) is used to detect the target radionuclides, and the measurement time is determined by the relative efficiency of the HPGe detector. The minimum detectable activity (MDA) is less than 5 Bq/kg for soft drinks and less than 10 Bq/kg for milk and infant foods.

(2) Quantitative analysis: If the target radionuclides are detected, quantitative analysis is performed for the samples. Solid samples must be minced before they are subjected to quantitative analysis. In this analysis, the weights of solid and liquid samples were 100–600 g and 900–1000 g,

respectively. The MDA was less than 1 Bq/kg for all samples.

Each laboratory had to evaluate the massic activity of I-131, Cs-134, and Cs-137 and report these activities with their standard measurement uncertainties ($k = 1$). The factors to consider in the determination of the measurement uncertainty are presented in Table 5.

Table 1: Comparison of the MOHWO0015.00 method (2016) and FDA WEAC-RN-Method 3.0 (2022).

Item	MOHWO0015.00	FDA WEAC-RN-method 3.0
Detector	HPGe	HPGe
Radionuclides to be determined	I-131, Cs-134 and Cs–137	I-131, Cs-134, Cs-137, Ru-103 and Ru-106
Sample mass	1st stage: (100-600) g for each sample matrix; 2nd stage: (1) solid : (100-600) g (2) liquid : (900-1,000) g	≥400 mL
Container	Marinelli Beaker, other appropriate container, or wrapped fully sample	500 mL
Counting time	based on MDA	600 s or 6000 s

2.1 Radionuclide determination

On the basis of the Taiwanese Standards for the Tolerance of Atomic Dust and Radioactivity Contamination in Foods, we selected I-131, Cs-134, and Cs-137 as target radionuclides for food safety testing. The half-life of I-131 is approximately 8 days, and iodine exhibits volatility, leading to a possible underestimation of the actual activity in the sample material . Therefore, accurately determining the activity of I-131 is difficult. Moreover, comparing the I-131 activities of samples with stable properties is challenging. Consequently, we used Ba-133 as a target nuclide instead of I-131, a practice that is followed in many countries. Ba-133 has a main gamma-ray energy close to that of I-131; therefore, Ba-133 can be used as a simulated radiation source for I-131. Zimmerman et al.

(2013) and Healey et al. (2015) also used Ba-133 instead of I-131 as a target nuclide.

The radioactive sources selected for testing in the present study were calibrated by the NRSL using gravimetric methods, which involved sample weighing with an electronic balance. The samples were diluted and prepared by the bi-weighing method with an electronic balance.

2.2 Sample categorization and HPGe calibration

According to the Standards for the Tolerance of Atomic Dust and Radioactivity Contamination in Foods, foods can be subdivided into three categories for radiological testing: milk and milk products, infant foods, and soft drinks and bottled water.

The present study considered three types of foods: milk powder (M), rice powder (R), and tea (T). Each food type included I-131, Cs-134, and Cs-137 with low and medium massic activity (2–10 Bq/kg and 10–100 Bq/kg, respectively). We used an HPGe detector with a relative efficiency of 30% (ORTEC GEM30P4 in USA) to examine the effects of sample geometry on the MDA and detection efficiency. Cylindrical containers with inner diameters of 10 cm or 5.7 cm were used. These containers are described as follows:

(1) For the cylindrical container with an inner diameter of 10 cm (container A), the detection efficiency substantially decreased when the sample volume was increased. Moreover, the MDA was a function of the sample mass (Figure 1) and decreased with increasing sample mass.

(2) The cylindrical container with an inner diameter of 5.7 cm (container B) had a higher detection efficiency than container A. Moreover, because container B had a lower sample mass than container A, the MDA was larger for container B.
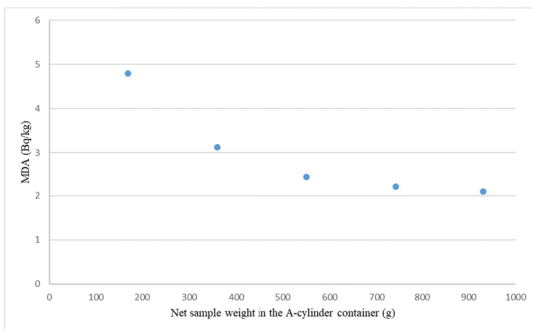

Figure 1: Variation in MDA with sample mass for container A.

2.2.1 Solid samples (M and R): A total of 600 g and 100 g of solid samples were filled in containers A and B, respectively; these containers were then sealed and sent to each laboratory. The laboratories conducted testing and analysis in accordance with the testing procedures of the MOHWO0015.00 standard. Milk powder and rice powder samples were packed into containers A and B, with the sample heights of these containers being 8 cm and 4 cm, respectively.

2.2.2 Tea samples (T): Tea samples weighing 1 kg each were directly distributed to each laboratory. The laboratories performed testing in Marinelli beakers for three sample weights: 100 g, 600 g, and 1000 g.

2.2.3 Standard water samples: The laboratories had to fill appropriate volumes or weights of water into their measurement containers following the standard operation procedures. For containers with a different shape or size to that of the container used for calibrations at the NRSL, a standard water sample was provided to the laboratories to enable them

to correct the system efficiency. The tea samples and standard water samples were filled in 1-L and 2-L cans, respectively.

2.3 Sample detection, data collection, and data analysis

A flowchart of the research procedure is displayed in Figure 2. The solid samples were shared by the laboratories, whereas separate liquid samples were provided to each laboratory. The samples were analyzed in accordance with the relevant laboratory's standard operating procedures. First, screening was conducted to detect the presence of the target radionuclides. Subsequently, if the target radionuclides were identified, quantitative analysis was performed. Each laboratory determined the massic activity (Bq/kg), relative uncertainty (%, k = 1), and MDA (Bq/kg) values for each target nuclide.

The data were analyzed in accordance with the ISO 17043(2023) standard. The absolute ζ-score [Equation (1)] was used to evaluate the results obtained by each laboratory, and results were considered acceptable only if $\zeta \leq 2$.

$$\zeta = \frac{|A_t - A_s|}{\sqrt{u_t^2 + u_s^2}} \qquad (1)$$

where A_t is the value reported value by a laboratory, A_s is the reference value provided by the NRSL, u_t is the uncertainty of the value reported by the laboratory, and u_s is the uncertainty of the reference value provided by the NRSL for a coverage factor (k) of 1.
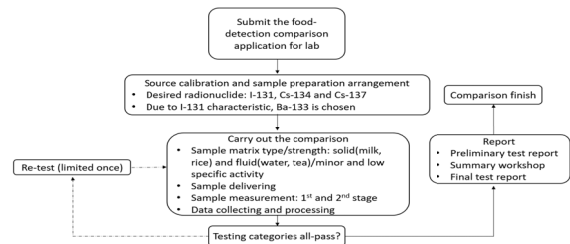
Figure 2: Research procedure.

3. Reference massic activity

Table 2 presents the reference massic activity of the three target radionuclides for the three types of samples. Figure 3 shows images of the tested samples, and Table 3 presents the activity of the standard water samples used for calibration. The NRSL distributed a bottle of water sample weighing approximately 1 kg to each laboratory.
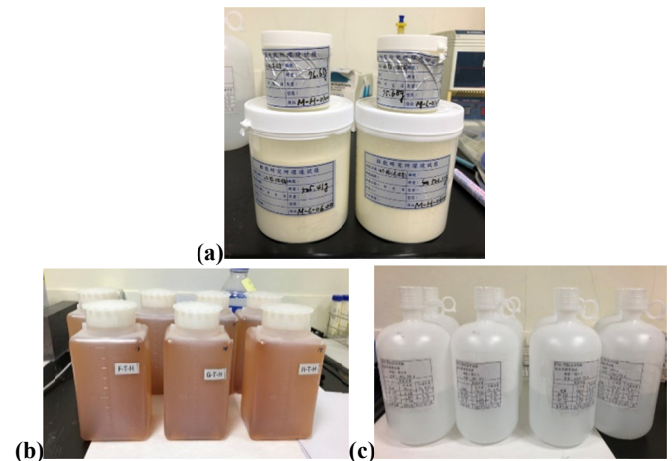
Figure 3: Samples used for testing. (a) Milk, (b) tea, and (c) water.

Table 2: Reference massic activity values of the target radionuclides for the different types of samples.

Matrix	Nuclide	Massic activity (Medium) (Bq/kg, k=1)	Massic activity (Low) (Bq/kg, k=1)
Rice	Ba-133	52.88 ± 1.5%	10.43 ± 2.2%
	Cs-134	25.24 ± 0.89%	10.06 ± 1.3%
	Cs-137	24.28 ± 1.1%	9.62 ± 1.4%
Milk	Ba-133	26.52 ± 1.5%	10.57 ± 3.2%
	Cs-134	12.17 ± 0.97%	5.09 ± 1.6%
	Cs-137	11.73 ± 1.2%	4.85 ± 1.4%
Tea	Ba-133	52.56 ± 2.2%	5.29 ± 2.2%
	Cs-134	5.01 ± 1.9%	2.54 ± 1.9%
	Cs-137	4.87 ± 1.9%	2.4 ± 1.9%

Table 3: Standard water samples used for calibration.

Matrix	Nuclide	Massic activity (Bq/kg, k=1)
Water	Ba-133	2,146 ± 0.72%
	Cs-134	2,053 ± 0.72%
	Cs-137	1,992 ± 0.77%

Because the regulations related to Cs-134 and Cs-137 activity limits applies to the sum of these, it is unclear whether the stipulated acceptable MDA (AMDA) value corresponds to the activity of an individual radionuclide only or to the total activity. Therefore, during sample preparation, both of Cs-134 and Cs-137 activities were maintained above the AMDA value in the screening stage. The tests for samples with medium levels of the target radionuclides were performed at half the regulatory limit. However, the tests for Cs-134 and Cs-137 in drinking water were performed close to the regulatory limit.

4. Results and discussion

4.1 First measurement stage

The measurement time of the first measurement stage was 1,000–18,000 s.

4.1.1 Rice powder and milk powder samples

Table 4 presents the MDA values obtained for the solid samples in the different laboratories. Some of the relevant results were as follows:

(1) For rice powder samples with a low massic activity, the massic activity was approximately equal to the MDA value.

(2) For milk powder samples with a low massic activity, the massic activity was approximately half the MDA value.

(3) When the MDA value was close to the target activity of the test sample, the radionuclide could not be quantified.

(4) The radionuclide could be identified for all samples with a medium massic activity.

Table 4: MDA values for the rice powder and milk powder samples.

	sample	Rice-powder sample	Milk-powder sample
MDA (Bq/kg)	Low	1-8.5	1.5-8.0
	Medium	1.5-7.0	1.5-7.0

Sufficient selectiveness was observed for the milk and rice samples in the first measurement stage.

4.1.2 Tea samples

The MDA values obtained for the tea samples in the different laboratories were between 0.3 Bq/kg and 4.5 Bq/kg. Some of the relevant results were as follows:

(1) For tea samples with a low massic activity, the massic activity was approximately half the MDA value, which was approximately half the regulatory limit.

(2) When the MDA value was close to the massic activity of the tea sample, the radionuclide could not be quantified.

(3) The target radionuclides could not be detected for three of the eighteen 100-g tea samples with low massic activity.

(4) The target radionuclides could not be detected for two of the eighteen 1000-g tea samples with low massic activity.

(5) The target radionuclides could be detected for all tea samples with medium massic activity.

When a certain radionuclide could not be detected in a sample in the first measurement stage, the sample was classified as having a low massic activity for that radionuclide, and the massic activity was below the MDA value stipulated in the announced method (MOHWO0015.00 standard). The first stage test method has a selective effect on soft drink (or bottled water).

To detect the radionuclides that were undetected in the first measurement stage, the following two actions were performed in the second measurement stage:

(1) The sample weight was increased to >300 g: According to the measurement results obtained for tea samples with weights of 100 g, 300 g, 600 g, and 1000 g, the sample weight was set to at least 300 g in the second measurement stage to enhance the detection rate.

(2) The MDA requirements were adjusted: Whether the specified AMDA value corresponds to the activity of Cs-134 only, Cs-137 only, or both Cs-134 and Cs-137 is unclear. Therefore, in this study, the MDA was maintained below 5 Bq/kg (half the regulatory limit) for the total activity.

The target nuclide was detected for all samples with a medium activity. The target nuclide could not be detected for some samples with a low activity; however, its presents is observable in the spectrum. For example, Cs-134 was not detected at a low activity level; however, it produced gamma energy peaks at 605 keV and 795 keV in the obtained spectrum (Figure 4). To overcome this problem in the future, the sensitivity of the adopted analysis software program can be adjusted, and related statements can be made in the analysis procedure.
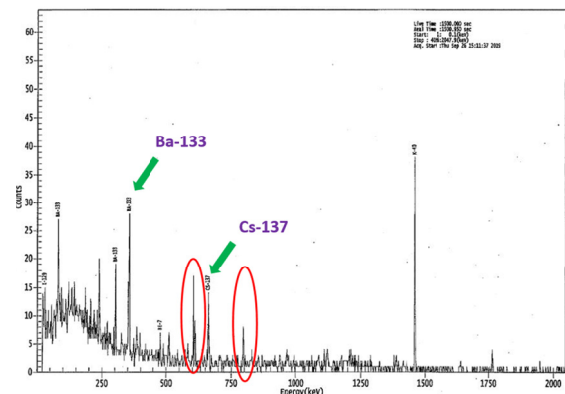

Figure 4: Gamma energy peaks produced by Cs-134 (indicated by red ovals) and the other target radionuclides.

4.2 Second measurement stage

The measurement time the second measurement stage was 1,830–180,000 s.

Figure 5 shows a total of 228 radioactivity measurements for the target radionuclides (the error bars denote the uncertainty of the ratio of the test value to the reference value). Some of the relevant results were as follows:

(1) A total of 97% of the ζ scores were less than 2. The red points marked in Figure 5 indicate ζ scores higher than 2, which did not meet the test requirements.

(2) The ratio of the test value to the reference value was closer to 1 for samples with a medium activity than it was for samples with a low activity.

(3) The distribution of the ratio of the test value to the reference value was approximately symmetrical around 1. This ratio changed marginally in the central part of the distribution and varied to a greater extent at the two ends, which is in line with the predicted statistical distribution. No significant deviation was observed between the reference and measurement values for each sample. The average ratio between the reference and test values was 1.02 ± 0.08 (k = 1).

(4) The bias (the difference between reported value and reference value) was in the range 0.83–1.11, 0.89–1.19, and 0.88–1.30 for Ba-133, Cs-134, and Cs-137, respectively. A total of 99% of the samples had a relative bias of less than 20%.

(5) For some laboratories, the MDA determined in the second measurement stage did not reach the limit of 1 Bq/kg; however, no abnormalities were observed in the overall performance.
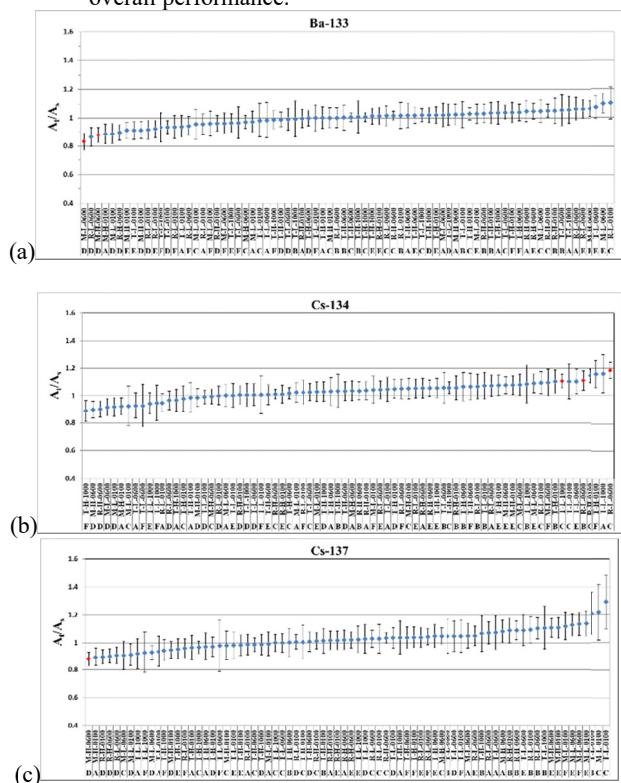

(a)

(b)

(c)

Figure 5: Ratio of test value (A_t) to reference values (A_s) for (a) Ba-133, (b) Cs-134, and (c) Cs-137.

5. Uncertainty

Uncertainty in the laboratory measurements was evaluated in accordance with the ISO GUM guidelines by considering the parameters listed in Table 5.

Table 5: Parameters considered for evaluating uncertainty in the laboratory measurements.

No.	Quantity
1	activity of standard
2	gamma branch ratio of activity standard
3	efficiency calibration curve
4	background
5	net area of full energy peak
6	gamma branch ratio of sample
7	geometry correction
8	density correction
9	decay correction
10	system long-term stability
11	weight
12	other statement

The measurement uncertainty ranges and average measurement uncertainty values for the target radionuclides are listed in Table 6. The large ζ score observed for certain laboratories were mainly caused by the measurement uncertainty being small. Lower uncertainty and higher accuracy were observed for samples with a medium activity than for samples with a low activity.

Table 6: Range of measurement uncertainty (k = 1) for the three radionuclides.

Item	Ba-133	Cs-134	Cs-137
Measurement uncertainty range	2.2%-13%	3.5%-17%	3.7%-20%
Measurement uncertainty range for 80% of the labs	1.9%-10%	3.0%-12%	3.8%-13%
Average value	6.9%	7.8%	8.5%

6. Conclusions

The Taiwanese Food and Drug Administration used the results of this interlaboratory comparison to review the suitability of currently applied methods in food radiation testing laboratories in Taiwan and the capabilities of these laboratories.

Among these 228 radioactivity measurements, about 98% of measurements meet the test requirements. It reveals that all the participating laboratories could detect the targeted radionuclides effectively and accurately considering the requested level of sensitivity. These test results were shared with the participating laboratories to enable them to improve their methods and processes. Through such improvements, food safety in Taiwan is enhanced.

References

ISO/IEC 17025:2017, General requirements for the competence of testing and calibration laboratories.

MOHWO0015.00, Ministry of Health and Welfare in Taiwan (ROC), 2016.

WEAC-RN.Method.3.0－Determination of Gamma-Ray Emitting Radioradionuclides in Foods by High-Purity Germanium Spectrometry, U.S. Food and Drug Administration, 2022.

Stephanie H., Kathryn E., Lindsey M., Zhichao L., Patrick R., 2015 FERN rapid detection and identification of gamma radioradionuclides in food, Center for Food Safety and Applied Nutrition, FDA.

Brian E. Z., Leticia P., Denis E. B., Jeffrey T. C., 2013 Calibration of Epoxy Based Ba-133 Standard Phantom Sources for Use in an International Comparison for Quantitative SPECT.

Standards for the Tolerance of Atomic Dust and Radioactivity Contamination in Foods, Ministry of Health and Welfare in Taiwan, 2015.

ISO/IEC 17043:2023. Conformity assessment-general requirements for proficiency testing.

Evaluation of measurement data — Guide to the expression of uncertainty in measurement (GUM 1995 with minor corrections) JCGM 100: 2008.

A Review of the Accuracy of Radionuclide Calibrators in UK Hospitals

Emma Bendall[a*], Natasha Ramirez[a], Andrew Fenwick[a]

[a] National Physical Laboratory, Hampton Road,

Teddington, Middlesex, TW11 0LW, UK

Abstract

During the routine calibration of hospital supplied sources by secondary standard ionisation chamber at the National Physical Laboratory (NPL), UK hospitals were asked to send their activity measurement of calibration sources for compilation and assessment. From June – December 2022 the data was collected, sorted by radionuclide, and analysed, and several areas of improvement were found, including the use of copper dippers and the way dial settings are derived.

Keywords: Radionuclide calibrator, accuracy, hospitals, calibration

* Corresponding author, e-mail address: emma.bendall@npl.co.uk

1. Introduction

Radionuclide calibrators are used in hospitals to measure the activity of radioactive sources used to treat and diagnose patients, allowing healthcare professionals to calculate the correct activity to be administered. They are therefore very important for patient care, as if they give the wrong activity value, then the patient is greatly affected. Radionuclide calibrators can give inaccurate activity readings for several reasons, including loss of gas (and therefore pressure), corrosion of electrodes (which affects their conductivity) and changes in vial geometry. To mitigate these, and other, effects national and international guidance (such as the NPL Good Practice Guide 93 and the IAEA Technical Report 454 (Gadd et al., 2006) (IAEA, 2006)) recommends annual calibration of a routinely used instrument against a reference instrument to ensure its continual traceability to the national standard. At the NPL, the Vinten 671 (SN: 3-5) secondary standard ionisation chamber fulfils the role of the reference chamber, allowing United Kingdom (UK) hospitals to use our customer supplied source calibration service to keep their calibrators accurate and traceable to primary standards.

The calibration service has been running for over thirty years and covers manufacturers, National Healthcare Service (NHS) hospitals and private hospitals within the UK as well as many international hospitals and manufacturers. For this service, the NPL receives active sources that were prepared by hospitals and measured on each of their calibrators. The calibration process (described in section 2) ensures that the calculated activity value is geometry independent. The activity value of the original source and any impurity data is reported back to the hospital, who then compare it to their activity measurement and may adjust the calibration factor or dial setting, as necessary.

The NPL recommends deriving a new dial setting if the hospital measurement is ± 5 % away from the NPL value or is inside the ± 5 % range but is consistently away from the NPL value across multiple calibrations. Ideally a statistical analysis is performed between the calibrated value and the hospital value to determine if the two results are statistically different, however in practice this may be tricky due to hospitals being unable to produce accurate uncertainty information (Fenwick et al., 2014; Ferreira and Fenwick, 2017)

Once calibrations are complete, customers of the service do not typically contact the NPL again until their next calibration is due, unless their measurement results are significantly (≥ ± 10 %) different to the calibrated value, but this happens infrequently. This means that the NPL does not have oversight of the overall measurement trends within the customer base. To rectify this, as part of the regular calibration service from June – December 2022, the measurement results from hospital calibrators were collected and analysed, and the hospital source was also measured on two in-house commercial calibrators.

2. Method

Once the hospital sources are received, they are measured on Vinten 671, and aliquots of this source are dispensed to ampoules of known geometries, with traceable calibration factors. The residue of the initial source is also measured on Vinten 671, and the true activity of the initial source is calculated. During this process, an impurity check is also performed, either using gamma spectrometry, or liquid scintillation for pure β emitters and corrections applied to the ionisation chamber measurements as appropriate. A simple breakdown of the uncertainties associated with this process can be seen in Table 1 below.

Table 1: *A table showing the approximate value of the major uncertainty components of the NPL certificate value. Typical certificate uncertainties at k = 2 are 1.5 % for ^{18}F, 1.7 % for ^{99m}Tc and ^{123}I and 1.4 % for ^{111}In.*

Uncertainty component	Maximum Value (k=1)
Capacitance	0.1 %
Measurement	0.05 %
Weighing	0.03 %
Calibration factor	Nuclide dependent (see below)
^{18}F	1 %
^{99m}Tc	0.9 %
^{123}I	0.9 %
^{111}In	0.75 %

To effectively analyse data collected from hospitals for trends and areas of improvement, it was decided that in addition to the activity measurement and reference time, the NPL would also collect the make and model of radionuclide calibrator and the dial setting used. Hospitals were informed of this study during the booking process, and that they would need to send the above data to the NPL before provisional certificates were released. They were also informed that the calibration source would be measured in the NPL CRC-12 and Atomlab 500 commercial radionuclide calibrators in addition to Vinten 671. These calibrators were chosen as they were thought to be representative of the brands of calibrators that hospitals use routinely. The measurements were made on the

manufacturer recommended dial settings, using the Perspex dipper provided. A background was taken before the calibration source was moved into the lab, and ten measurements of the source were taken. A background corrected average was then calculated. This was to provide a picture of how accurate the results are when the calibrator is used as specified by the manufacturer.

After the final certificate had been made, all results were compiled (i.e., the hospital activity measurement, the NPL commercial calibrator activity measurements, the certificate value, and the initial activity measurement on Vinten 671). The results were separated by radionuclide, decay corrected to the certificate reference time, if necessary, and the percentage difference between the certificate value and measurement was calculated. Some additional information was also gathered, including the type of vial (based on which Vinten 671 holder it fits into), if the dial setting used was the manufacturer recommended one or a derived one, and for ^{111}In and ^{123}I, if a copper dipper was used for the measurement. Each individual hospital was given a unique number to anonymise the data. This data was then filtered for the above information and plotted on bar charts of percentage difference to certificated value vs. type of calibrator.

3. Results and Discussion

3.1 Dial Settings

Dial settings are how radionuclide calibrators convert the current measurement into an activity. They are different for each radionuclide, as they are dependent on the energy of the emissions. They are also different for each brand and sometimes model of radionuclide calibrator, as they are affected by the geometry of the chamber, the type of gas it is filled with and the pressure that the gas is at. They can change over time as the calibrator ages, e.g. the chamber losing gas (and therefore pressure), or electrodes corroding. Therefore, new dial settings must be derived when measured activity is outside of accepted limits (± 5 %).

For this study, we received results on hospital reporting sheets rather than standardised forms, so it could be seen how new dial settings were derived for some locations. One common method was to measure the source on multiple dial settings above and below the existing dial setting, then plot a curve of the activity and derive a new dial setting based on that curve. Whilst this method works, it is quite time consuming and requires a reasonably complex spreadsheet to perform the necessary calculations.

Another method is to measure the calibration source on the existing dial setting, then when results are received calculate the percentage difference between the measurement and the NPL result, measure a long-lived check source (for example, ^{226}Ra) on the same dial setting and change it until the percentage difference in measured activity matches the calculated one. This is much less time consuming and requires fewer complicated calculations and as such was recommended to the hospitals that had used the former method.

3.1.1 Manufacturer dial settings compared to derived dial settings

All commercially available radionuclide calibrators come with manufacturer recommended dial settings, which are often determined from measurements made with ampoules. For Capintec calibrators, the geometry used is approximately 5 g of solution in borosilicate glass ampoules with a diameter of 17 mm, length of 40 mm and wall thickness of 0.6 mm (Capintec, inc., 2004) for most radionuclides. Therefore, it is important to derive new dial settings (particularly for low energy radionuclides) if they are routinely measured in a geometry that is significantly different.

During the study, the manufacturers dial setting was noted, along with the dial setting the hospital routinely used. The comparison of using the manufacturers dial setting to a derived dial setting is shown in figuresFigure 1 andFigure 2 for ^{99m}Tc, as it is

representative of the trends across all radionuclides. It was found that most hospitals (17 are using the manufacturers dial setting to measure radionuclides, but when using derived dial settings, the variance of the results decreases – the maximum percentage difference drops from 11.2 % to -2.2 %. This is because the derived dial settings are specific to each instrument and its specific condition i.e., gas pressure, position in the lab, etc.
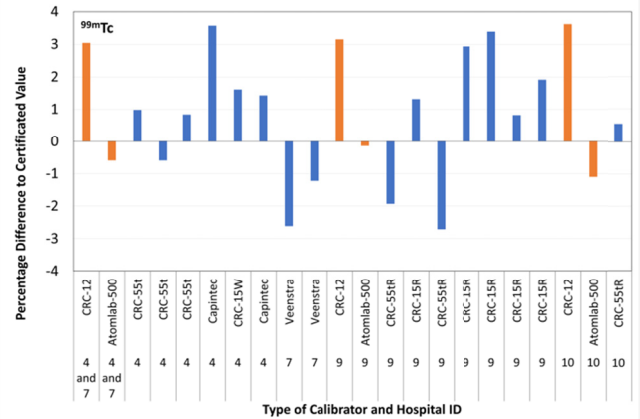

Figure 1: Percentage difference to certificated value vs. type of calibrator for ^{99m}Tc, where the source was measured with the original manufacturer dial setting. The orange values are from the NPL calibrators, and the numbers are the hospital ID for the associated source.

Figure 2: Percentage difference to certificated value vs. type of calibrator where the ^{99m}Tc source was measured with a derived dial setting. The CRC-15 Beta is a CRC-15R chamber combined with a NaI detector. Calibrator types were taken directly from the hospital reporting sheets.

3.2 Geometry effects

Radionuclides are typically received in a glass vial; however, the type of glass vial differs depending on the radionuclide and supplier of the radionuclide. In addition, many of these glass vials are not standardised, so there can be differences in the thickness of the walls, height of the vial, etc. For radionuclides that don't have intense low energy X ray emissions, these differences are often insignificant, however for radionuclides with high intensity low energy X-ray emissions (or pure beta emitters), the geometry of the vial makes a big difference to the activity measurement. This is because the X-ray emissions are easily attenuated, and therefore changes in the vial geometry will make a difference to the activity measured, described in more detail in the NPL Good Practice Guide

93 (Gadd et al., 2006), where the ratio of calibration factor for a given container is compared to that of a 10R Schott vial (also known as a VCDIN10R). For a P6 vial for ^{99m}Tc and ^{123}I, these are 1.00 and 0.98 respectively. For ^{111}In in a 5 ml syringe, this ratio is 1.25.

To quantify geometry effects in this study, the type of holder used to measure the starting vial in Vinten 671 was recorded, which gives an indication of the diameter of the base of the vial, which can be seen in Table 2 below:

Table 2: *A table comparing the approximate base diameters of the Vinten 671 holders, to give an idea of scale.*

Vinten 671 Holder	Approximate Diameter (mm)
P6	25
10R	27
Cs	33

The P6 and 10R holders were designed to fit P6 and 10R Schott vials respectively, and the Cs holder was designed to fit the ^{137}Cs check source that is used on Vinten 671, and the holder is used to measure any vial with a wider base diameter than a 10R Schott vial. A photograph of some representative vial types can be seen in Figure 3.
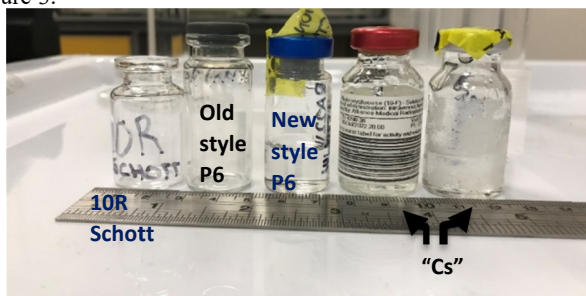
Figure 3: *A photograph comparing some common vial types used by hospitals. The new style P6 vial is now exclusively used instead of the old style P6, which is included here as the P6 calibration factors for Vinten 671 are based on the old style.*

Plots comparing the different vial types can be seen for each radionuclide in Figure 4. The percentage difference is an average of all results for that radionuclide. The initial source measurement in Vinten 671 is also included in these graphs, as only the certificated value is independent of geometry. From these graphs it can be seen that the vials measured in the Cs holder have the most divergence across all radionuclides. This is due to the variance in each vial, in height, width, and in the wall thickness.

Figure 4: *Plots of average percentage difference to certificated value of ^{18}F, ^{99m}Tc, ^{123}I and ^{111}In compared to different vial types.*

In the plot for ^{18}F (top left in Figure 4), the average of percentage difference to the certificated value for Cs vials is 1.4 %, which is the lowest of all comparable values for the radionuclides represented. This is because ^{18}F only has two X-ray emissions, both at 0.525 keV (Chisté et al, 2014), and the 511 keV gamma emissions dominate the spectrum. Cs vials are not commonly used for ^{99m}Tc, but one hospital used one for their calibration. The results from all measurements for this geometry were higher than the certificated value by 8.8 % on average. This is clearly anomalous, and as such was omitted.

3.2.1 Copper Dippers

To counteract the geometry effects mentioned in the previous section, copper dippers are frequently used with radionuclides that have high intensity low energy X-ray emissions alongside higher (100 keV+) gamma emissions, as this ensures that all low energy emissions are attenuated. These are frequently used with ^{111}In and ^{123}I.

In the bottom row of Figure 4, the average of percentage difference to certificated results can be seen for ^{123}I and ^{111}In. These radionuclides are both commonly measured with copper dippers, which reduce geometry effects and therefore also reduces the average percentage difference. When the results obtained using a copper dipper are removed for each radionuclide, the average for Cs vials for ^{123}I increases to -22.9 %, and the same value for ^{111}In increases to -5.5 %.

The most data for the use of copper dippers was acquired for ^{111}In, so a comparison of using copper dippers vs. no copper dippers when measuring the source are shown in figures Figure 5 and Figure 6. Figure 5 shows the percentage difference to certificated value vs. type of calibrator when a Perspex dipper was used, and Figure 6 shows the same variables for when a copper dipper was used. In Figure 6, one outlier was removed, as an incorrect dial setting was used (the manufacturer recommended one, which is intended for use without a copper dipper), and thus the result was -22.8 % different to the certificated value. This shows the importance of deriving a new dial setting if there is a major change to the way radionuclides are measured in a radionuclide calibrator. Comparing figures Figure 5 and Figure 6, the maximum percentage difference goes from -13.1 % to –2.8 %, which is an improvement of 10.3 %.

Figure 5: *A graph of percentage difference to certificated value vs. type of calibrator for ^{111}In when a Perspex dipper was used to take the measurement. The orange values are from the NPL calibrators, and the numbers are the hospital ID for the associated source. The first two NPL values cover hospitals 5, 6, 7 and 14.*
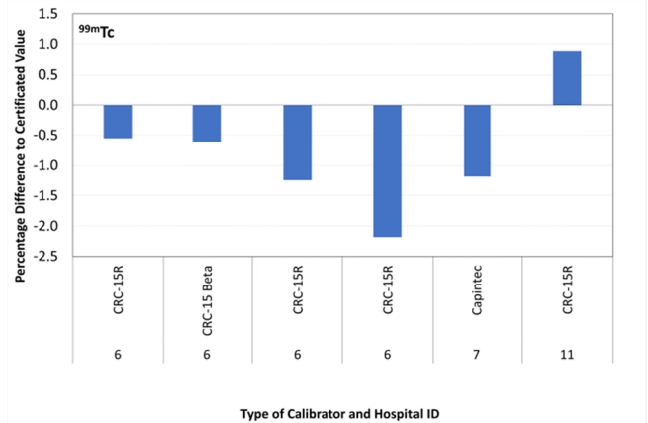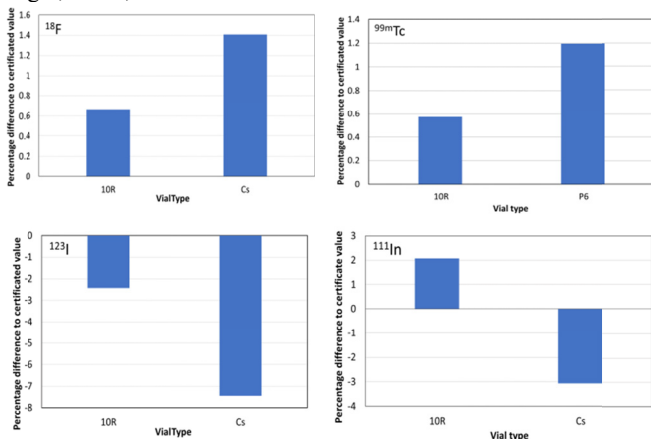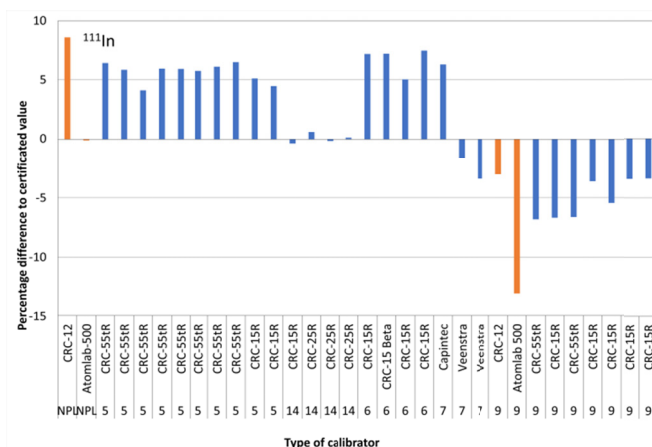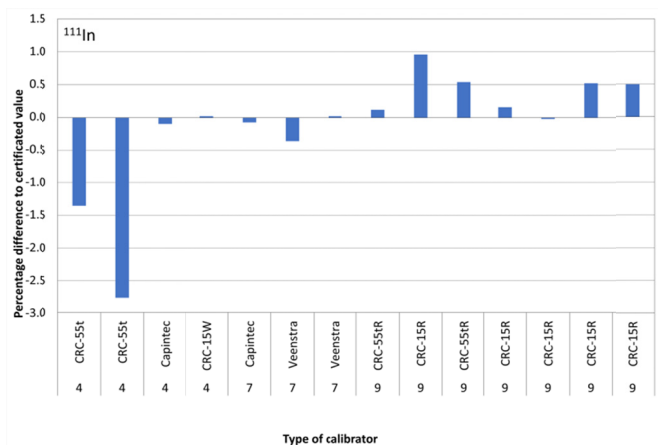
Figure 6: A graph of percentage difference to certificated value vs. type of calibrator for ^{111}In measurements where a copper dipper was used.

3.3 Spreadsheet errors

Another consequence of receiving hospital spreadsheets was that the data entered by hospitals could be observed, and any mistakes that could impact the results were recorded. Such mistakes were very rare, but one that reoccurred in a few calibrations was that the wrong half-life was used, for example, for ^{111}In a half-life of 2.9049 days was used in one instance, instead of 2.8049 (4) days (Bé et al, 2006) from DDEP. This resulted in the decay corrected values being an average of 0.9 % higher than the correct decay corrected value. The NPL use half-lives either from LNBH and the DDEP working group, the database of which can be found at http://www.lnhb.fr/nuclear-data/nuclear-data-table/ or ENSDF, which can be found at https://www.nndc.bnl.gov/ensdf/, with uncertainties at $k = 2$ when reporting results on certificates.

The NPL always reports time in UTC on certificates and reports, and it was noticed that when converting between UTC and British Summer Time (BST), some hospitals had decayed the NPL activity value incorrectly, or not decayed it at all. In one instance for a ^{99m}Tc calibration the NPL value was assumed to be in BST (i.e., the same time-zone as the hospital measurement), and the percentage difference was 11.6 %, but once this was corrected, the percentage difference was – 0.6 %. Shorter-lived radionuclides such as ^{18}F and ^{68}Ga would be more affected, and longer-lived radionuclides such as ^{111}In and ^{123}I would be less affected, and as such the mistake would be harder to spot.

It is therefore important to thoroughly check the data entered on reporting sheets to catch any errors made.

4. Conclusion

In conclusion, this study achieved what it set out to do, which was to identify both overall measurement trends in UK hospitals and any areas of improvement. It was identified that overall; hospitals can measure with adequate accuracy routine radionuclides (i.e. within ± 5 %). There were several areas of improvement, including the use of copper dippers when measuring geometry sensitive radionuclides, deriving dial settings for regularly used vial types, and rigorous spreadsheet checking. It was also recommended that the way new dial settings are derived could be changed to a less time-consuming method where practical.

This study will continue into 2023 to monitor any evolving trends and find any further areas of development.

References:
CRC®-15R Radioisotope Dose Calibrator Owner's Manual, Capintec, Inc., Florham Park, NJ, 2004, Revision W

Bé, M.M., Chisté, V., Dulieu, C., Browne, E., Baglin, C., Chechev, V., Helmer, R., Kondev, F., MacMahon, T.D. and Lee, K.B., 2006. Table of radionuclides (Vol. 3 – A = 3 to 244). BIPM Monographie-5.

Chisté V., Bé, M.-M., Kuzmenko, N.K., 2014 LNE-LNHB/CEA Table of radionuclides, Decay Data Evaluation Project working group, Update 1 September 2014, http://www.lnhb.fr/nuclides/F-18_tables.pdf [Accessed 31/05/2023]

Fenwick, A., Baker, M., Ferreira, K., Keightley, J., 2014. Comparison of ^{90}Y and ^{177}Lu measurement capability in UK and European hospitals. Applied Radiation and Isotopes 87. https://doi.org/10.1016/j.apradiso.2013.11.050

Ferreira, K.M., Fenwick, A.J., 2018. ^{123}I intercomparison exercises: Assessment of measurement capabilities in UK hospitals. Applied Radiation and Isotopes 134. https://doi.org/10.1016/j.apradiso.2017.11.015

Gadd, R., Baker, M., Nijran, K.S., Owens, S., Thomson, W., Woods, M.J., Zananiri, F., 2006. Measurment Good Practice Guide No. 93: Protocol for Establishing and Maintaining the Calibration of Medical Radionuclide Calibrators and their Quality Control. National Physical Laboratory.

IAEA, 2006. Quality assurance for radioactivity measurement in nuclear medicine. Technical Reports Series 454 (No. TRS 454), Technical Report Series. IAEA, Vienna.

Primary internal gas counting at NRC Canada

James Renaud[a*] and Raphael Galea[a]

[a] Metrology Research Centre, National Research Council Canada, Ottawa, Ontario, Canada

Abstract

The National Research Council (NRC) of Canada is developing a new primary method for radioactive noble gas counting using a length-compensated proportional counter system. As an initial trial, the activity concentration of a sample of Xe-133 was determined in the plateau region 1980(20) V for three pairs of proportional counters operating at a pressure of $1.724(3) \times 10^2$ kPa. The mean absolute value of the activity concentration was found to be in line with expectations based on Xe-133 supplier-provided information.

Keywords: length-compensated proportional counter; gas counting; Xe-133; activity concentration; primary activity standard

* Corresponding author, e-mail address: james.renaud@nrc-cnrc.gc.ca

1. Introduction

Radioactive noble gases and tritium are emitted from nuclear reactors when electricity is produced, accidents occur and as the result of nuclear weapons testing or use, and hence are of great interest to the nuclear forensics communities (Schulze et al., 2000). In addition, some radioactive noble gases serve critical medical functions, as is the case of Xe-133 in the diagnostic imaging for certain lung cancers (Mattsson et al., 2015). The accepted method by which radioactive noble gases have been standardized in terms of primary activity concentration is through the use of length-compensated proportional counters (LCPC) (Unterweger, 2007).

Internal gas counting involves the introduction of a beta-emitting radioactive gas sample within an LCPC system composed of two or more nominally identical cylindrical chambers of varying lengths. The so called length-compensation refers to the cancellation of complex end effects occurring due to the presence of non-uniform electric fields in the counter cap regions. The method requires that the volume, V, differences between any pair of counters (e.g., "short" and "long") be accurately known, as the activity concentration, A_V, is based on the net count rate, R, per net volume:

$$A_V = \frac{R_{long} - R_{short}}{V_{long} - V_{short}}$$

At present, several national metrology institutes (NMI) operate internal gas counting systems as primary radioactivity standards, including KRISS (Korea Research Institute of Standards and Science) (Seon et al., 2020), NMIJ AIST (National Metrology Institute of Japan) (Yunoki et al., 2010), LNE-LNHB (Commissariat à l'énergie atomique/Laboratoire National Henri Becquerel, France) (Unterweger, 2015), and NPL (National Physical Laboratory, UK) (Philips et al., 2010). The National Research Council (NRC), which serves as Canada's NMI, is developing a new primary method for radioactive noble gas counting using an LCPC. The aim of this work is to provide an overview of the NRC LCPC design as well as system performance through initial trials performed with samples of Xe-133.

2. System description

Internal gas counting at NRC consists of two separately operated systems, as shown in Figure 1; one for the gas handling, the other for data acquisition (DAQ).

At the heart of the gas handling system are three stainless steel cylinders, vertically mounted and serially connected, each with an inner diameter of 25 mm and respective lengths of (155.0(5), 256.5(5) and 384.0(5)) mm. The cylinders are capped at both ends with blank CF flanges machined to accommodate two ¼" (6.35 mm) feedthroughs for gas flow. A stainless steel wire with a diameter of 25.4 μm is strung along the central axis of each cylinder forming the anodes of the three proportional counters. Custom electrical feedthroughs are fashioned by off the shelf PEEK ferrule assemblies (Idex VacuTight™ fittings) that mate to 1.6 mm diameter stainless steel pins spot welded at each end of the anode wire. An SHV connection is made at the top pin and the opposite end is capped with an electrical insulator (glass-filled PEEK) to prevent electrical discharge. The volumes of the counters were gravimetrically calibrated through national measurement standards maintained at the NRC and were determined to be 88.43(55) cm^3, 143.66(54) cm^3, and 212.92(55) cm^3 ($k = 2$) (*uncertainties in parentheses throughout this work are for k = 1 unless otherwise stated*) (procedure described in Harris & Miller, 2019). Two counters are in principle sufficient to determine the activity concentration, and the third provides a measure of redundancy to permit the detection of potential malfunctions and increase the overall confidence in the system.

The other major components of the gas handling system include: (i) the radioactive gas sample, which can be introduced by means of a glass ampoule, compressed cylinder or quick connected sealed vessel, (ii) P10 (90 % argon + 10 % methane) proportional counting gas cylinder, (iii) digital pressure regulators (Clippard CPC-HFE-QA), (iv) bespoke circulating fan and mixing chamber to permit the counting measurements to be performed in either a dynamic gas flow or static state, (v) high-volume ballast tank to mitigate emergency evacuation occurrences, (vi) 1000 mL spherical quartz reference volume (Technical Glass Products, Inc.), (vii) pressure transducers (Setra barometric transmitter 0-50 Psia), (viii) vacuum transducers (Agilent FRG-700 Pirani/inverted magnetron), (ix) temperature sensors (USP12920 3892K) and, (x) a turbo vacuum pump (Edwards T-Station 85) that vents to the outside of the building. Despite the relatively small tubing (stainless steel ¼" (6.35 mm)) and number of bends, the vacuum pump can evacuate the gas handling system to a minimum pressure on the order of 1 Pa.

An instrumentation chassis (National Instruments PXIe-1088) is used to remotely monitor and precisely control process variables via LabVIEW code, including the pressure regulator settings, circulation fan operation as well as pressure and temperature logging. To verify the long term stability of the gas handling system volume, or a portion thereof, a volumetric expansion of the quartz reference volume is performed by first filling the system with pure nitrogen gas to a known pressure, closing the valve to the known reference volume, evacuating the system, and subsequently refilling the system with the contents of the reference volume, all while monitoring the internal gas temperature (i.e., Boyle-Charles gas laws). Accurate control of input pressures permit the quantitative

dilution of a gas mixture in much the same way. Once a contained sample of radioactive gas is standardized in terms of activity concentration, certified reference materials may be disseminated by means of flame sealing a glass ampoule or through a quick-connect manifold.

The DAQ system consists of a largely digital electronic readout chain designed to detect and count pulses in the proportional counters. The electrical connections between the anodes and the DAQ are made via the inputs of three charge sensitive preamplifiers (Ortec 142PC) that supply a common bias provided by a programmable high voltage power supply (Caen N1470 4-CH). The charge-integrated signals from the preamplifiers are fed to the analog inputs of a CAEN N6725S 8-CH 14-bit @ 250 MS/s 2 Vpp DPP-PHA (digital pulse processing for pulse height analysis) digitizer. The PDD-PHA (pulse height analysis) option provides a trapezoidal filter on the input pulses, which is the digital equivalent of having a shaping amplifier and peak sensing ADC. It has programmable input offset, trigger, and energy filter capabilities, and provides pulse timing information. The configuration of the DAQ parameters on parallel channels is managed using CAEN mc2 Analyzer (v.2.1.5.0).
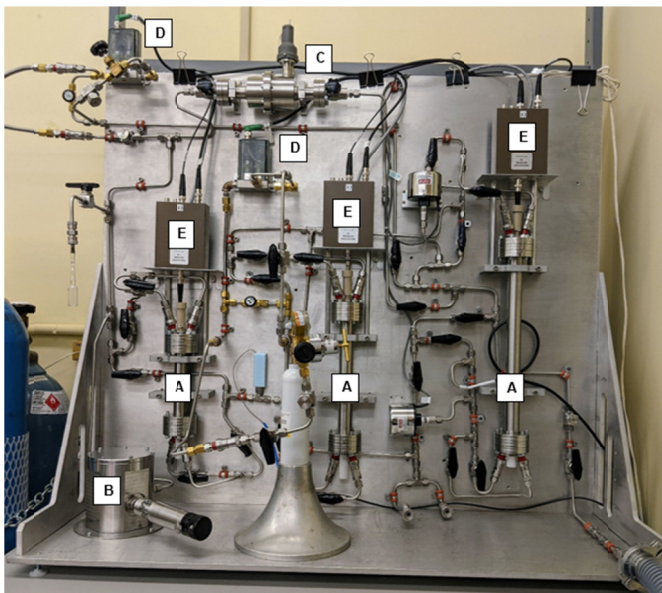

Fig. 1: The NRC internal gas counting setup consisting of both gas handling and DAQ systems. Major components labeled in the photo are: (A) Short, medium and long proportional counters, (B) casse-ampoule, (C) circulation fan and mixing chamber, (D) digital pressure regulators, (E) preamplifiers.

3. Activity concentration measurements

The radioactive gas under study is a Xe-133 gas standard (Eckert & Ziegler) pressurized to 9.6×10^3 kPa at STP in a 500 mL lecture bottle with a nitrogen carrier gas. The supplier-provided total activity of the sample at the reference date was 4.989×10^8 Bq (± 3.0 %, $k = 2$) with a quoted Xe-131m impurity content of 0.52 %. The activity of the master source of Xe-133 was determined with an ionization chamber with an NPL (Teddington, UK) calibration traceable to national standards.

While initially evacuated, the gas handling system was uniformly filled to a pressure of 328.2(2) Pa with the Xe-133 lecture bottle in an ambient temperature of 294.85 K. The system was then further pressurized to $1.724(3) \times 10^2$ kPa by the addition of P10. The combination of gases was mixed for 1 hour in an attempt to achieve homogeneity throughout the proportional counters. A variable bias in the range of (1200 – 2150) V was applied in steps as large as 50 V in regions of lesser interest and as small as 5 V in the

response plateau region. For each bias setting, the count rates for the three channels corrected for the dead time were sampled in parallel over a 200 s period. The background counting rate was subsequently measured at the operating pressure as a function of bias with only P10 present inside the system. The counting rates obtained with the Xe-133 were background-subtracted and then used to determine three activity concentrations; one for each pair of proportional counters. The parameters specific to the input signal, trigger and energy filter used in the acquisitions are summarized in Table 1.

The measured activity concentrations were compared to an expected value based on the supplier-provided decay-corrected activity and pressure of the compressed Xe-133 cylinder. This information was combined with an estimate of the volume of the gas handling system obtained from a volumetric expansion of the reference volume and the pressure of the system upon filling.

Table 1: The list of parameters set in the configuration of the three channels involved in this study. The associated digitizer is a CAEN N6725S 8-bit 14-bit @ 250 MS/s 2 Vpp DPP-PHA and the acquisition software used was CAEN mc2 Analyzer (v.2.1.5.0).

Setup category	Parameter	Value
Input signal	DC offset	80.00 %
	Input range	2.0 Vpp
	Fine gain	1.0000
	Pulse polarity	Positive
	Decimation	1
Trigger	Threshold	500 LSB
	Input rise time	0.50 μs
	Trigger holdoff	5.00 μs
	RC-CR2 smoothing	4
	Fast filter correction	Enabled
Energy filter	Baseline mean	16384
	Rise time	8.00 μs
	Decay time	130.00 μs
	Baseline clip	Enabled
	Flat top	1.50 μs
	Peak decay	30.00 %
	Peak mean	16
	Peak holdoff	5.00 μs
	Baseline holdoff	2.00 μs

4. Results and discussion

4.1 Volumetric stability of gas handling system

The mean temperature-corrected volume of the gas handling system was determined to be 1007.6(4) mL and was stable to within 0.04 % over the 6 month period of this investigation. The ratio of the combined active volume to the total system volume was calculated to be 0.442(1). The internal temperatures of the gas handling system was in the range of (294.6 – 295.4) K at the time of these volume measurements. The consistency of the overall system volume suggests that the individual proportional counter volumes, and their respective differences, are stable at a similar level.

4.2 Xe-133 activity concentration measurement

A plot depicting the HV plateaus for the three counters containing the Xe-133 sample at an operating pressure of $1.724(3) \times 10^2$ kPa is shown in Figure 2 for a bias range of (1200 – 2150) V. The optimal bias setting corresponding to the approximate middle of the three plateau regions was determined to be 1980(20) V (depicted as vertical shaded bar in Figure 2). In this optimized bias range for this operating pressure, the mean background (i.e. P10 only) count rates from the short, medium and long proportional counters were 2.202(44) s^{-1}, 3.667(75) s^{-1} and 8.439(114) s^{-1}, respectively. Once background-corrected, the three mean count rates measured in the presence of the Xe-133 were measured to be 166(1) s^{-1}, 248.2(7) s^{-1} and 343.4(2) s^{-1}. The net counting rates as a function of volume difference for each counter in shown in Figure 3. With the intercept fixed at zero, the slope, which corresponds to the net count rate per unit volume, is 1.42(1) s^{-1}•mL^{-1}.
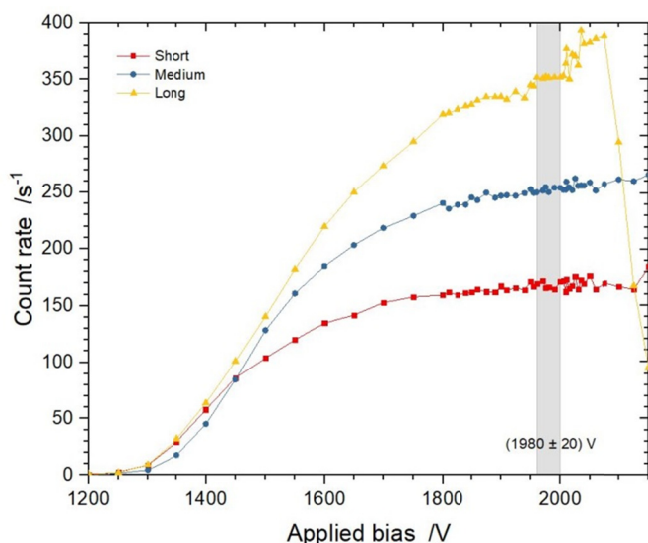

Fig. 2: The measured count rates for the three proportional counters containing the sample of Xe-133 at an operating pressure of $1.724(3) \times 10^2$ kPa in the bias range of (1200 – 2150) V. The relatively stable plateau region is depicted by the shaded vertical bar spanning (1980 ± 20) V.
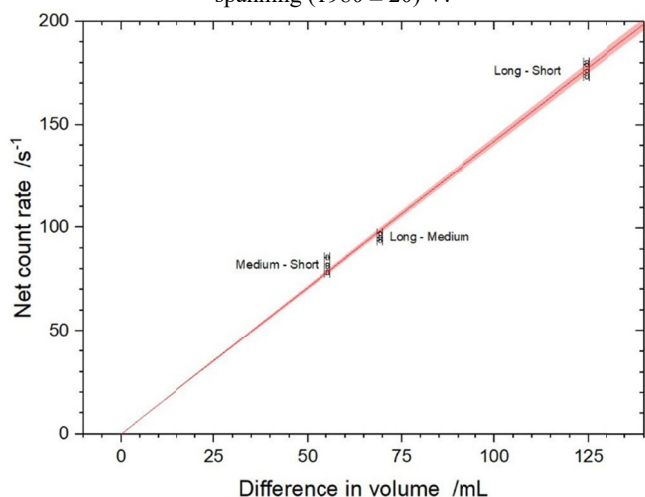

Fig. 3: The linear fit of the net count rate for the three differences in volume corresponding to the three pairs of proportional counters. The horizontal bars on the data points reflect the uncertainties in the calibrated cylinder volumes. The vertical scatter in the data is the variation observed as a function of bias in the range of (1960 – 2000) V. The red shaded area about the line of best fit is the 95 % confidence interval.

The mean absolute activity concentration determined from six different bias settings from (1960 – 2000) V was 1523(22) Bq•L^{-1} with an associated standard error on the mean of 1.4 % ($k = 2$). The 18 individual activity concentrations of this set of measurements (shown in Figure 4) ranged from (1469 – 1594) Bq•L^{-1}. In comparison, the expected activity concentration of the Xe-133 sample was estimated to be 1467(53) Bq•L^{-1} (horizontal dashed line and shaded area in Figure 4 plot). The relatively large uncertainty (3.6 %) being primarily due to the uncertainty in the manufacturer-provided activity. Other major contributions to the uncertainty include the absolute volume estimate of the gas handling system as well as the estimation of the Xe-133 compressed cylinder volume and pressure.
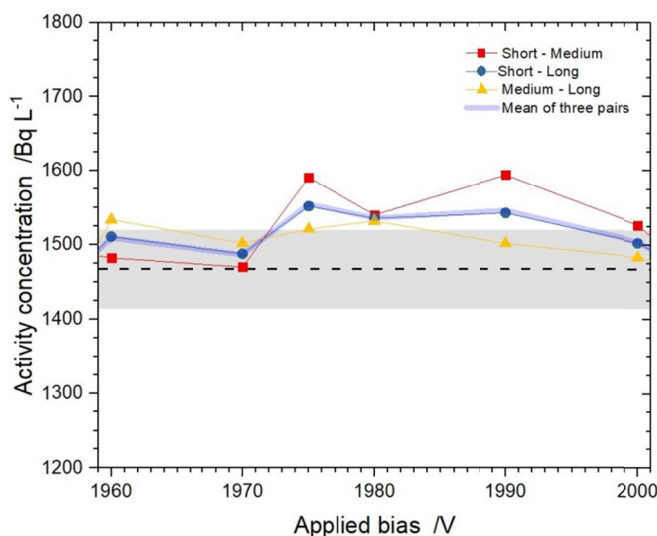

Fig. 4: Experimentally determined absolute activity concentration of the Xe-133 sample for the three pairs of proportional counters in the plateau region of (1960 – 2000) V. The mean of the three pairs is depicted by the shaded blue line. The horizontal dashed line and shaded area correspond to the expected activity concentration (1467(53) Bq•L^{-1}) based on supplier-provided information

Before an overall assessment of uncertainties may be made, the following outstanding effects must first be addressed:

(i) *The apparent drop in count rates observed at voltages past the plateau region* – As the bias applied to a gas-filled detector is progressively increased, the expected behavior is to pass the proportional region of the response (i.e., plateau) and enter a region of gas multiplication in which the count rate rapidly rises. To date, the opposite effect has been observed (see the long counter at >2100 V in Figure 2) in all three counters. The most likely reason is an increasing rate of saturation of the preamplifers, which then completely overwhelm the digitizer channels creating excessive dead times. The focus then becomes determining the cause for unexpectedly large proportional counter pulses. Possible reasons may including arcing in the region of the wire-pin interface, though the results of finite element modeling have suggested that this is unlikely following measures taken to insulate the spot weld. Incomplete mixing of the gases due to a possible lack of flow may be a contributing factor and will require verification. The composition of the gas mixture or some other contamination present in the system may also be to blame, in particular the relatively large amount of the nitrogen carrier in the Xe-133 cylinder, since the same drop in counts is not observed for the case of P10 only. The next steps are to repeat the study with another beta-emitting gas, ideally Kr-85 with its longer half-life, with little to no nitrogen carrier present. Another suggested avenue has been to try reverse-

P10 (90 % methane and 10 % argon) as other groups have done in the past6.

(ii) *Extrapolation to zero energy* - The effect of the counts lost below the threshold setting, an often dominant source of uncertainty in LCPC, is not accounted for in this study and will be the subject of ongoing work in which extrapolations to zero energy are compared against Monte Carlo-derived beta spectra (Unterweger 2015). This approach will require an energy calibration by means of a suitable source (*e.g.*, Fe-55).

(iii) Direct comparison against existing standards – As always, the ultimate measure of the accuracy will come from participating in a direct comparison against established primary standards which typically budget an overall relative standard uncertainty of (1.2 – 2.5) % (k = 2). Demonstrating agreement among, ideally independent, methods is needed not only to build confidence, but to validate any estimated uncertainty budgets.

5. Conclusions

A primary internal gas counting capability for beta-emitting noble gases based on LCPC is under development by NRC Canada. This initial trialing of the system with a sample of Xe-133 suggests that for a pressure of $1.724(3) \times 10^2$ kPa, a bias of 1980(20) V will place the operation of the system within the stable range of the HV plateau. The mean measured absolute activity concentration was found to be consistent with expectations based on the Xe-133 supplier provided information, though questions remain pertaining to the unexpected drop in the count rates at higher voltages past the plateau region.

References

Harris, G.L., & Miller V.R. (2019) SOP 14-1 Gravimetric Calibration of Volumetric Ware Using an Electronic Balance, in *Selected Procedures for Volumetric Calibrations* NISTIR 7383, (2019 Ed).

Mattsson, S., Johansson, L., Liniecki, J., Noßke, D., Riklund, K.Å., Stabin, M., Taylor, D., Bolch, W., Carlsson, S., Eckerman, K. and Giussani, A., 2015. Radiation Dose to Patients from Radiopharmaceuticals: a Compendium of Current Information Related to Frequently Used Substances. Annals of the ICRP, 44(2 Suppl), pp.7-321.

Phillips, H. C., Johansson, L. C., & Sephton, J. P. (2010). Standardisation of 85Kr. Applied Radiation and Isotopes, 68(7-8), 1335-1339.

Schulze, J., Auer, M., & Werzi, R. (2000). Low level radioactivity measurement in support of the CTBTO. Applied Radiation and Isotopes, 53(1-2), 23-30.

Seon, Y., Hwang, S. H., Lee, J. M., Lee, K. B., Heo, D. H., Han, M. J., & Kim, H. J. (2020). The primary system for measurement of beta emitting radioactive gases at KRISS. Applied Radiation and Isotopes, 164, 109238.

Unterweger, M.P. (2007) Primary radioactive gas standards (excluding radon). Metrologia, 44(4), S79.

Unterweger, M., et al. (2015). Uncertainties in internal gas counting. Metrologia, 52(3), S156.

Yunoki, A., Yamada, T., Kawada, Y., Unno, Y., Sato, Y., & Hino, Y. (2010). Activity measurement of 85Kr diluted by a large volume balloon technique. Applied Radiation and Isotopes, 68(7-8), 1340-1343.

Application of inductively coupled plasma tandem mass spectrometry for re-measuring the half-life of long-lived radionuclides

Emma C. Braysher[a*], Ben Russell[a], Arzu Arinc[a], Marc Abilama[a], Robert Shearman[a], Elsje van Es[a], Peter Ivanov[a], David Read[b]

[a] National Physical Laboratory, Hampton Road, Teddington, Middlesex, TW11 0LW, UK
[b] University of Surrey, Stag Hill, Guildford, Surrey, GU2 7XH, UK

Abstract

Mass spectrometry is increasingly used for contributing to half-life determination through atom counting. Tandem inductively coupled plasma mass spectrometry (ICP-MS/MS) has demonstrated improved online interference removal for multiple radionuclides, but has not been applied to half-life measurements. This paper details the first known investigation of ICP-MS/MS for half-life measurement, focusing on ^{238}U. The optimal setup, combined with Defined Solid Angle (DSA) measurement, calculated a half-life of 4.444 (55) $\times 10^9$ a, in agreement with the current value of 4.468 (5) $\times 10^9$ a. Further improvements in the instrument setup are recommended.

Keywords: Mass spectrometry, isotope dilution, half-life, atom counting, nuclear data

* Corresponding author, e-mail address: emma.braysher@npl.co.uk

1. Introduction

Mass spectrometry is a technique well-suited to the measurement of medium and long-lived radionuclides. It is increasingly being used in areas including decommissioning, environmental monitoring and nuclear forensics as a rapid alternative to radiometric measurement techniques. More recently, mass spectrometry has been used to contribute to re-measurement of the half-life of long-lived radionuclides using atom counting, in combination with absolute decay counting measurements. Advances in mass spectrometry means the accuracy and precision of radioisotopic dates are now sometimes limited by knowledge of the decay constants rather than the analytical uncertainty in atom counting and isotope ratio measurements (Parsons-Davis et al., 2018).

Short to medium half-lives can be determined by measuring the activity or the number of atoms and observing how they change over time (Pommé, 2015), through the relationship between the decay constant (λ) and the half-life ($t_{1/2}$):

$$t_{1/2} = \frac{\ln(2)}{\lambda} \qquad (1)$$

The half-life can also be measured using the mass concentration of the isotope of interest (m_x), the activity of the sample per mass unit (A) and the atomic mass of the isotope (M) as well as Avogadro's number (N_A) to give the number of atoms (N):

$$t_{1/2} = \ln(2)\frac{N}{A} = \ln(2)\frac{n \cdot N_A}{A} = \ln(2)\frac{N_A \cdot m_x}{A \cdot M} \qquad (2)$$

Previous half-life studies have used thermal ionisation mass spectrometry (TIMS) (Bé et al., 2015; Cheng et al., 2000; He et al., 2009), accelerator mass spectrometry (AMS) (Dou et al., 2014; MacDonald et al., 2016a), high-resolution ICP-MS (Kossert et al., 2013) and multi-collector inductively coupled plasma mass spectrometry (MC-ICP-MS) (Cassette et al., 2010; Cheng et al., 2013; Essex et al., 2018; Jerome et al., 2019; Nedjadi et al., 2012; Parsons-Davis et al., 2018; Varga et al., 2016; Yang et al., 2010) (Table 1). While TIMS and AMS were more traditionally used in half-life studies for their high sensitivity, ICP-MS application has

been increasing in recent years, with at least 15 half-life studies mentioning ICP-MS in the past two decades (figure 1).
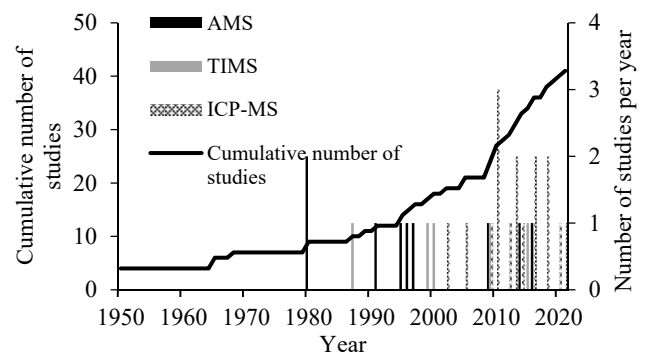

Fig. 1: Cumulative number of half-life studies over time using mass spectrometry.

Over the last decade, commercially available Inductively Coupled Plasma Tandem Mass Spectrometry (ICP-MS/MS) has been increasingly used for medium and long-lived radionuclide measurement, with the online interference removal capability reducing or removing the need for relatively time-consuming offline chemical separation (Croudace et al., 2017; P E Warwick et al., 2019). However, ICP-MS/MS has never been applied to half-life determination.

Uranium-238 was identified as a good candidate to test ICP-MS/MS for half-life measurements due to its long half-life of 4.468 (5) $\times 10^9$ a (Bé et al., 2006) and subsequently its low specific activity, resulting in good sensitivity for mass spectrometry measurement. Uranium-238 does not suffer from significant spectral interferences, therefore is unlikely to utilise the interference removal capabilities of ICP-MS/MS. A radionuclide such as ^{238}U, that does not need these capabilities provides an opportunity to optimise the setup and compare the precision achievable to alternative instrument designs.

Table 1: Examples of recent studies using mass spectrometry for measuring long half-lives (uncertainty k=1 unless stated otherwise).

Radionuclide	Starting sample	Sample preparation	Activity measurement	Mass spectrometry technique	Half-life	Reference
[238]U	''Q-metal'' uranium, containing (99.96 % [238]U)	HF digestion	Gamma spectrometry	MC-ICP-MS	4.456 (21) 10^9 a	Parsons-Davis et al. (2018)
[79]Se	Purified selenium (enriched in [78]Se to 57 %)	Stepwise dilution with high-pure selenium dioxide	Liquid scintillation counting	AMS	2.78 (18) $\times 10^5$ a	Dou et al. (2014)
[93]Zr	High level liquid waste	Silica gel adsorption and TBP extraction	Liquid scintillation counting	MC-ICP-MS	1.13 (11) $\times 10^6$ a	Yang et al. (2010)
[135]Cs	Stainless steel pipe used for collecting radio-Xe gas, decayed for several hours	HF digestion	Liquid scintillation counting	AMS / ICP-MS	1.6 (6) $\times 10^6$ a / 1.3 (2) $\times 10^6$ a	MacDonald et al. (2016)
[151]Sm	Sm_2O_3, enriched in [150]Sm to 87.27 %	Dissolution in HNO_3	Liquid scintillation counting	TIMS	96.6 (24) a	He et al. (2009)
	Samarium oxide, enriched in [149]Sm to 95.1 %	HPLC	Liquid scintillation counting	TIMS	94.6 (6) a	Bé et al. (2015)
[230]Th	Zircons, spar, latite and uraninite	Dissolution in HNO_3	None	TIMS	75690 (230) a ($k = 2$)	Cheng et al. (2000)
[234]U	Zircons, spar, latite and uraninite	Dissolution in HNO_3	None	TIMS	245250 (490) a ($k = 2$)	Cheng et al. (2000)

Uranium-238 is a key isotope in geological dating techniques, with the decay of [238]U and [235]U to [206]Pb and [207]Pb forming the basis for one of the oldest methods of geochronology (Begemann et al., 2001). Despite this, the current recommended half-life is based on a single published value in 1971 (Chisté and Bé, 2005; Jaffey et al., 1971; Schön et al., 2004). The low uncertainty of 0.12 % ($k = 2$) associated with this measurement has been unmatched in other studies (Schön et al., 2004; Villa et al., 2022). It is thought that this is due to the fact that systematic uncertainties, while considered, were not included in the uncertainty quoted (Schön et al., 2004; Villa et al., 2022). As a result, an uncertainty of double the magnitude has been applied to the recommended value as a conservative estimate to account for the systematic uncertainties (Chisté and Bé, 2005). Additionally, a call has been made for new measurements of the half-life with accuracies comparable to the work of Jaffey et al. (Schön et al., 2004). Previous measurements of the [238]U half-life, and the current recommended value, are shown in figure 2. A call for an improved set of decay constants for geochronological use was published in 2001 (Begemann et al., 2001), stating that the accuracy of radioisotopic ages is limited by the accuracy of radioactive decay constants. Radioisotopic dating is directly dependent on accurate measurement of decay constants and therefore a thorough understanding of associated uncertainty is necessary (Ludwig, 2003; Parsons-Davis et al., 2018; Schoene et al., 2006; Schön et al., 2004; Villa et al., 2016).
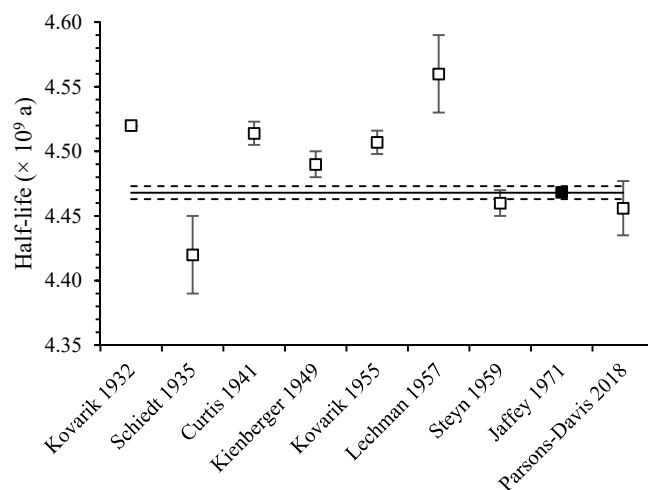
Fig. 2: Previously measured half-life values and associated uncertainties, with the black lines being the current recommended value and its associated uncertainties (Chisté and Bé, 2005; Schön et al., 2004).

The most recent published measurement of the [238]U half-life was from Parsons-Davis in 2018 (Parsons-Davis et al., 2018). In this study, the ingrowth method was used, in which ingrowth of the progeny radionuclide is measured as a ratio to the parent over several years, which is discussed in more detail in the Parsons-Davis study and elsewhere (Braysher et al., 2020; Varga et al., 2016). This is relevant for a long-lived radionuclide such as [238]U with a relatively short-lived progeny such as [234]Th as the activity of

the parent can be assumed as constant over the measurement time. In this study ^{238}U was quantified by MC-ICP-MS, ingrown thorium was extracted, purified and also measured. The thorium aliquots were then allowed to decay to ^{234}U for ≥ 10 half-lives of ^{234}Th and the number of ^{234}U atoms were counted, representative of the number of ^{238}U atoms decayed. The ^{238}U half-life was determined at $4.456\ (21) \times 10^9$ a and the ^{234}Th half-life at 24.157 (74) d, but there was internal inconsistency in measurements that increased the relative uncertainty on the ^{238}U half-life value to 0.462 % ($k = 2$).

Isotope dilution mass spectrometry is the most commonly used method when using mass spectrometry for half-life applications. Isotope dilution relies on a spike of known isotope ratio of the element of interest, preferably significantly different to that of the sample, being added to the sample of measured isotope ratio. The ratio of the isotopes in the mixed sample and spike will then be measured with no reliance on signal intensity (Braysher et al., 2020). A sample with a certified isotopic ratio should also be measured, most commonly using the sample:standard bracketing technique, to calculate and correct for instrument bias when measuring isotopic ratios.

This study investigates the advantages and limitations of ICP-MS/MS for half-life measurement for the first time. The instrument setup was optimised for uranium isotope measurements using isotope dilution mass spectrometry, with the performance assessed compared to results achieved in other studies using MC-ICP-MS. A further aim was to develop a consistent method for atom counting by ICP-MS/MS that can be applied to other radioisotopes with good understanding of uncertainty budget.

2. Materials & methods

Uncertainties are quoted as k=1 throughout unless stated otherwise.

2.1 Instrumentation

Two ICP-MS/MS instruments (Agilent 8800 and a newer generation Agilent 8900) were used. Each of these instruments is equipped with two quadrupole mass filters, separated by a collision-reaction cell. A detailed instrument setup and optimisation is discussed elsewhere (Braysher et al., 2020). Although online interference removal was not required for ^{238}U measurements, the instrument performance using both one (Single Quad) and both quadrupole mass filters (MS/MS) was evaluated. The reaction cell gas was not investigated, although this would be beneficial for other radionuclides where offline chemical separation cannot reliably remove interferences (P E Warwick et al., 2019). In addition to the standard sample introduction system (Scott double pass spray chamber, Microconcentric nebuliser, SP4 autosampler and peristaltic pump), an Apex Q desolvating sample introduction system (Elemental Scientific) was also tested. This system introduces the sample as a dry aerosol, resulting in reduced hydride and oxide-based interferences, as well as a 3-10-fold sensitivity improvement (Elemental Scientific, n.d.) compared to the standard sample introduction system.

2.2 Sample preparation

A solution of ^{238}U in HNO$_3$ in equilibrium with ^{234}Th and ^{234m}Pa was used (Braysher et al., 2021). The uranium was separated from actinides and progeny using the PUREX (Plutonium Uranium Reduction Extraction) process (Sawant et al., 1998). The separated uranium-containing solutions were combined and evaporated to incipient dryness, then redissolved in 4 mL of 2 M HNO$_3$.

2.3 Defined solid angle counting for primary standardisation

To remove residue and contamination prior to measurement, alpha discs were washed with acetone, acetic acid (0.01 M) and ethanol sequentially. Prior to sample deposition, the thickness of the disc was measured in five locations across the surface using a calibrated micrometre. Three discs were prepared by depositing, one, two and three drops of uranium-containing solution to each disc respectively. Photographs of the discs were taken to show the distribution of activity on the disc surface. The photographs were used to create Monte Carlo models for estimation of the geometrical efficiency of particles which pass through the diaphragm. These drop-deposited sources were measured using NPL's bespoke defined solid angle (DSA) counting facility at a controlled laboratory temperature of 20.0 (10) $^\circ$C in order to minimise changes to the solid angle (Arinc et al., 2016). A background measurement was run both before and after each sample measurement. An example spectrum is shown in figure 3. The source peak is identified and then the total counts, combined with the live time measured using a controlled pulser signal, are used to produce a background corrected count rate. Using the geometrical efficiency obtained from running Monte Carlo simulations, this count rate is then efficiency corrected and decay corrected to a chosen reference date. Having previously measured the mass of the deposits precisely, the activity per mass is then determined.

2.4 Isotope dilution

Two sequential controlled dilutions of the ^{238}U source were performed using a 6-figure balance (Mettler Toledo XP20) in order to minimise loss of alpha energy due to thickness of source. The gravimetric dilution factor was calculated from mass measurements and this was checked against the radiometric dilution factor measured by liquid scintillation counting (LSC). For the LSC measurements, two aliquots of the solution to be diluted were taken before and after dilution for each dilution stage. The aliquots were 0.1 g for the high level and 2.0 g for the lower level so that activity in all the vials were matched. These aliquots were dispensed into glass LSC vials containing 15 mL Ultima Gold AB scintillant with varying amounts of 2 M HNO$_3$ carrier to match cocktail to scintillant ratios. The vials were mixed gently to achieve homogeneity. The samples were measured with a Packard TriCarb 2910TR liquid scintillation counter for two measurement cycles with a count time of 360 minutes. Vials containing 2.0 g HNO$_3$, were measured before and after the active vials for background correction.

Due to its long half-life of $245.5\ (6) \times 10^3$ a and lack of spectral interferences ^{234}U was selected as a spike for isotope dilution. Solutions of ^{238}U spiked with ^{234}U were made up to 10 mL from the standardised and diluted ^{238}U sample spiked with a ^{234}U NPL standard (102.49 (59) Bq g^{-1}). These isotope dilution standards were prepared using a dedicated source preparation facility using a six-figure balance (Mettler Toledo XP20). This produced a range of samples containing ^{234}U/^{238}U mass ratios between 0 and 10.

2.5 Mass bias correction

A Certified Reference Material (CRM U970) (New Brunswick Laboratory, U.S. Department of Energy) of U$_3$O$_8$ powder with 1.7 % ^{234}U, 97.7 % ^{235}U, 0.1 % ^{236}U and 0.5 % ^{238}U (w/w) was used to assess and correct for mass bias. The uranium powder was dissolved in concentrated HNO$_3$ (trace analysis grade, Fisher Scientific) and diluted in 2 % (v/v) HNO$_3$. All masses were recorded using a 6-figure balance (Mettler Toledo XP20).

The linear mass bias law was used to correct for mass bias using sample bracketing, as exponential and power models are virtually linear at high mass minimal difference is seen between models as outlined previously (Braysher et al., 2020; Taylor et al., 1995).
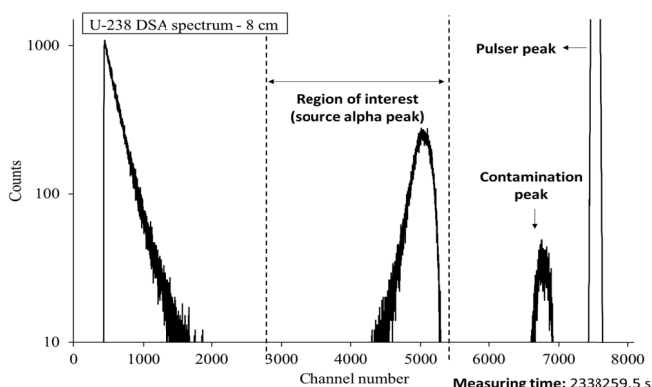
Fig. 3: DSA spectrum of sample 3 at 8 cm. ROI source peak relates to U-238 alpha emissions peak. Contamination peak is ignored and relates to non-uranium alpha emissions due to prior contamination present on DSA disc holder currently in use. Pulser peak relates to the controlled 10 Hz signal used to determine live time.

3. Results and discussion

3.1 Uranium-238 activity measurement

The weighted mean of three DSA measurements of different sources and geometries were used to determine the final value of activity per unit mass of the ^{238}U solution; this was taken as 44.85 (15) Bq g^{-1} (Table 2). Counting statistics were poor due to the necessary dilution of the activity per unit mass of the ^{238}U to minimise alpha energy loss. An example uncertainty budget is included in Table 3. The activity per mass unit value of the ^{238}U solution used in the final half-life measurement was calculated at 0.06505 (31) Bq g^{-1} using the LSC dilution check factors and an added uncertainty component for the dilution.

Table 2: Summary of DSA counting measurement results (reference date 04/12/2019 14:00 UTC).

Sample ID	Geometry (cm)	Peak counts	Activity per mass unit (Bq g^{-1})	Uncertainty (%)
Sample 1	8	12520	44.21 (43)	0.98
Sample 2	8	92130	44.93 (20)	0.44
Sample 3	15	28360	44.95 (30)	0.67
Weighted mean			44.85 (15)	0.34

Table 3: Uncertainty budget for a single DSA measurement.

Source of uncertainty	%
Source statistics	0.59
Background statistics	0.23
Efficiency	0.036
Weighing	0.18
Dead-time	0.028
Distribution activity	0.10
Combined standard uncertainty	0.67 %

3.2 Uranium-238 mass measurement

In order to calculate the ^{238}U concentration in the samples, the ^{238}U/^{234}U count ratio (R), corrected for mass bias, drift and background, was multiplied by the concentration of ^{234}U in each sample (m_y) and the dilution ratio (mass of ^{238}U solution added to the isotope dilution sample as a fraction of total sample mass, n):

$$m_x = m_y \times R \times n$$

An average was taken of nine samples. The instrument was optimised to maximise sensitivity and minimise uncertainty for the uranium isotopic ratio measurement, as discussed in the following sections.

3.2.1 Initial instrument optimization

The effect of the number of sweeps and replicates was investigated on the Agilent 8800 ICP-MS/MS. A replicate is a single analysis of the sample, while a sweep is the signal pulse through the quadrupole passing across the mass spectrum of selected mass-to-charge (m/z) values. The measurement uncertainty was generally lower with increased number of sweeps and replicates, until plateauing at around 300 sweeps and 10 replicates; these values were therefore used throughout this study.

The effect of increasing stabilisation time from 10 to 40 s was also investigated at 10 s intervals (figure 4). Improved sensitivity was seen for increased stabilisation time; however sample consumption is increased which should be considered if sample size is limited. A stabilisation time of 20 s was used in this study to maximise measurement sensitivity and minimise run time.

The lens settings were custom tuned using a ^{Nat}U standard. This standard was run for approximately eight hours prior to running the samples. This followed discussions with the instrument manufacturer that it was beneficial to leave the instrument time to stabilise prior to measuring uranium isotopic ratios. A previous study also showed the importance of assessing the measurement time on the stability of the measured uranium isotopic values (Lindahl et al., 2021).
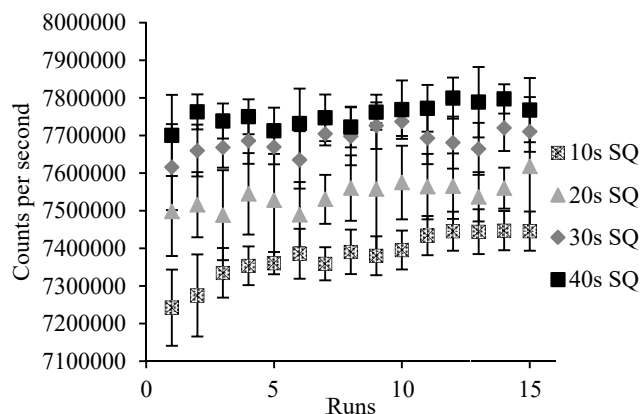

Fig. 4: Effect of stabilisation time on instrument sensitivity to ^{238}U in single quadrupole (SQ) mode.

3.2.2 Instrument mode

Initial measurements were run in MS/MS mode, which in this study sets both quadrupole mass filters to m/z = 238. Compared to Single Quad mode where only mass filter is operating, sensitivity is reduced, however there is reduced tailing interference, whilst filtering of the ion beam prior to entering the collision-reaction cell reduces in-cell polyatomic interference formation. However, as these interferences did not impact ^{238}U measurement in this study, MS/MS mode was not expected to be necessary. In MS/MS mode, a ^{238}U mass concentration of 5.30 (19) µg g^{-1} was determined corresponding to a relative uncertainty of 3.6 %. By comparison, in Single Quad mode, a ^{238}U concentration of 5.19 (12) µg g^{-1} and an uncertainty of 2.26 % was measured. CRM U970 was used to test for interferences, which were seen to be negligible. Single Quad mode was therefore used for all further testing.

3.2.3 Sample introduction

The impact of the sample introduction system was assessed by switching the standard sample introduction setup with the Apex Q. Self-aspiration was also recommended by the instrument manufacturer to provide a more stable signal; standard sample introduction uses the peri-pump which causes pulses in the sample flow. The carrier gas and make up gas flow rates for the Apex Q were the key instrument parameters that varied compared to the standard sample introduction system. The addition of the Apex Q

improved the sensitivity by an order of magnitude compared to the standard sample introduction system, as well as reducing the measurement uncertainty to 1.28 %, with a calculated [238]U concentration of 5.286 (67) µg g^{-1}.

3.2.4 Instrument version

The Agilent 8800 settings were replicated on the newer generation Agilent 8900. Using the standard sample introduction system, a [238]U concentration of 5.243 (50) µg g^{-1} was calculated with an improved uncertainty of 0.96 %. The sensitivity of the 8900 was over six times higher than the Agilent 8800 when using the same sample introduction system. Because of limited sample availability and the need to share equipment between laboratories, there was only an opportunity to do a single run using the Apex Q with the Agilent 8900. A sensitivity of 95,000 CPS per µg of [238]U was achieved, compared to the next highest value of 49,000 CPS per µg using the older Agilent 8800 with the Apex Q. However, the uncertainty increased slightly to 0.97 %, with a slightly less stable signal across the samples tested. Future work should include additional testing of this setup as is it likely that further uncertainty reductions and improvements in signal stability achieved with the Agilent 8800 could be made.

Table 4: Measured [238]U mass concentration using different instrument modes.

Instrument/mode/sample introduction system	[238]U concentration (µg g^{-1})	Relative uncertainty (%)	Average CPS per µg of [238]U
8800 / MS/MS / Standard	5.30 (19)	3.6	738
8800 / SQ / Standard	5.19 (12)	2.3	4816
8800 / SQ / Apex	5.286 (67)	1.3	48813
8900 / SQ / Standard	5.243 (50)	0.96	32512

Table 5: Summary of optimal instrument setup Instrument. *Microconcentric nebuliser, Peltier-cooled double pass spray chamber.

Instrument	Sweeps	Replicates	Stabilisation time (s)	Mode	Sample introduction system
8900	300	10	20	SQ	Standard*

3.2.5 Summary of optimal instrument setup

Uranium-238 concentrations measured in each instrument mode are shown in Table 4, and a summary of the optimum instrument setup is shown in Table 5. The newer generation ICP-MS/MS operating in Single Quad mode with the standard sample introduction system was considered the optimal setup. It is expected that this could be improved with further testing using the Apex Q sample introduction system with the same instrument.

For all instrument setups, the isotope ratio measurement of the CRM and the [234/238]U isotope dilution samples contributes the highest uncertainty; following background and isotope standard correction, the RSD associated with the isotope ratio measurement ranged from 0.71-1.2 % in SQ mode. The [234]U mass concentration contributes 0.016-0.20 %, while the dilution ratio contributes 0.0041-0.010 %. The uncertainty budget suggests that the single detector setup limits the isotope ratio precision achievable, as the detector must 'hop' between masses.

4. Uranium-238 half-life

The activity and mass measurements were combined with the atomic mass of [238]U (IUPAC, n.d.) and Avogadro's number (Güttler et al., 2019) as in previously shown in Equation 2. Table 6 and Figure 5 show calculated half-life values measured with each instrument setup. All of the measured half-life values agree with the current recommended half-life with uncertainties reflecting that of the concentration measurements. The mass measurement dominated the combined uncertainty budget at 0.96 % for the optimised setup. Uncertainty contributions from atomic mass and Avogadro's number are negligible, while the activity per mass unit contributes 0.47 %.

Table 6: Calculated half-life values using different mass measurement modes with associated uncertainties.

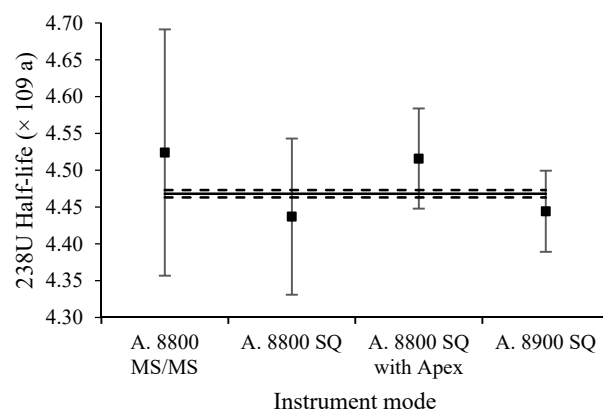| Mass measurement mode	Half-life (a)	Relative uncertainty (%)
8800 MS/MS	4.52 (17) × 10^9	3.7
8800 SQ	4.44 (11) × 10^9	2.4
8800 SQ with Apex	4.516 (68) × 10^9	1.5
8900 SQ	4.444 (55) × 10^9	1.2

Fig. 5: Half-life values calculated using different instrument modes compared to the current recommended half-life value and uncertainty (solid and dashed black lines, respectively).

Although the precision achieved by ICP-MS/MS for [238]U (1.2 %) was higher than the uncertainty in a recent using MC-ICP-MS (0.462 %) (Parsons-Davis et al., 2018) there are a number of radionuclides that have benefitted from the tandem setup where

offline chemical separation alone cannot completely remove interferences e.g. ^{93}Zr, ^{36}Cl, ^{90}Sr and ^{129}I (Croudace et al., 2017; Russell et al., 2017; Phillip E Warwick et al., 2019; Yang et al., 2010). For these radionuclides the ICP-MS/MS technique may be beneficial for contributing to updated half-life measurements. However, the long-term stability of cell product formation and isotope ratio precision must be carefully considered. Further investigations should include testing of the Agilent 8900 system together with the Apex Q sample introduction. Further testing of the optimal stabilisation period with lens settings custom tuned using a ^{Nat}U standard should be quantified.

Conclusions

This paper details the first application of ICP-MS/MS for half-life measurement. Isotope dilution was used and the instrument setup was optimised for measurement of ^{238}U. The measurement precision was significantly improved through optimisation of the instrument setup, including number of sweeps and replicates, stabilisation time, sample introduction system, as well as the instrument mode and instrument type. Half-lives measured with all instrument setups agreed with the current recommended half-life. The relative uncertainty of the measured half-life was 1.2 %, compared to the current recommended value of 0.12 % and 0.462 % using MC-ICP-MS in a recent study. A consistent approach has been developed for long half-life measurement using ICP-MS/MS, including a full uncertainty budget.

Acknowledgements

References

Arinc, A., Parfitt, M.J., Keightley, J.D., Wilson, A., 2016. Defined solid angle alpha counting at NPL. Appl. Radiat. Isot. 109, 198–204. https://doi.org/10.1016/j.apradiso.2015.11.073

Bé, M.-M., Chisté, V., Dulieu, C., Browne, E., Baglin, C., Chechev, V., Kuzmenco, N., Helmer, R., Kondev, F., Macmahon, D., Lee, K.B., 2006. Monographie BIPM-5 Table of Radionuclides (Vol. 3 - A = 3 to 244). http://www.nucleide.org/DDEP.htm, Sevres.

Bé, M.M., Isnard, H., Cassette, P., Mougeot, X., Lourenço, V., Altzitzoglou, T., Pommé, S., Rozkov, A., Auerbach, P., Sochorová, J., Dziel, T., Dersch, R., Kossert, K., Nähle, O., Krivošík, M., Ometáková, J., Stadelmann, G., Nonell, A., Chartier, F., 2015. Determination of the 151Sm half-life. Radiochim. Acta 103, 619–626. https://doi.org/10.1515/RACT-2015-2393/MACHINEREADABLECITATION/RIS

Begemann, F., Ludwig, K.R., Lugmair, G.W., Min, K., Nyquist, L.E., Patchett, P.J., Renne, P.R., Shih, C.Y., Villa, I.M., Walker, R.J., 2001. Call for an improved set of decay constants for geochronological use. Geochim. Cosmochim. Acta 65, 111–121. https://doi.org/10.1016/S0016-7037(00)00512-3

Braysher, E., Russell, B., Read, D., 2021. Development of Reference Materials and Evaluation of Decay Data in Support of Characterisation of Naturally Occurring Radioactive Material. https://doi.org/10.15126/THESIS.900238

Braysher, E., Russell, B., Read, D., 2020. Application of plasma mass spectrometry for half-life measurement of medium and long-lived radionuclides. J. Phys. Conf. Ser. 1643.

Cassette, P., Chartier, F., Isnard, H., Fréchou, C., Laszak, I., Degros, J.P., Bé, M.M., Lépy, M.C., Tartes, I., 2010. Determination of 93Zr decay scheme and half-life. Appl. Radiat. Isot. 68, 122–130. https://doi.org/10.1016/J.APRADISO.2009.08.011

Cheng, H., Edwards, R.L., Hoff, J., Gallup, C.D., Richards, D.A., Asmerom, Y., 2000. The half-lives of uranium-234 and thorium-230. Chem. Geol. 169, 17–33. https://doi.org/10.1016/S0009-2541(99)00157-6

Cheng, H., Lawrence Edwards, R., Shen, C.-C., Polyak, V.J., Asmerom, Y., Woodhead, J., Hellstrom, J., Wang, Y., Kong, X., Spötl, C., Wang, X., Calvin Alexander, E., 2013. Improvements in Th-230 dating, Th-230 and U-234 half-life values, and U–Th isotopic measurements by multi-collector inductively coupled plasma mass spectrometry. Earth Planet. Sci. Lett. 371–372, 82–91. https://doi.org/10.1016/J.EPSL.2013.04.006

Chisté, V., Bé, M.M., 2005. 238U - Comments on evaluation of decay data.

Croudace, I.W., Russell, B.C., Warwick, P.W., 2017. Plasma source mass spectrometry for radioactive waste characterisation in support of nuclear decommissioning: A review. J. Anal. At. Spectrom. 32, 494–526. https://doi.org/10.1039/C6JA00334F

Dou, L., Jiang, S., Wang, X.-B., Dong, K.-J., Wu, S.-Y., Yang, X.-R., Wang, X.-M., Lan, X.-X., Xia, Q.-L., He, M., 2014. Measurement of the half-life of 79 Se with accelerator mass spectrometry. Chinese Phys. C 38, 106204. https://doi.org/10.1088/1674-1137/38/10/106204

Elemental Scientific, n.d. Apex - Q (ES-4384-1000-21) [WWW Document]. URL https://www.icpms.com/files/flyers/Apex Q System F-16051.pdf (accessed 6.23.23).

Essex, R.M., Mann, J.L., Collé, R., Laureano-Perez, L., Bennett, M.E., Dion, H., Fitzgerald, R., Gaffney, A.M., Gourgiotis, A., Hubert, A., Inn, K.G.W., Kinman, W.S., Lamont, S.P., Steiner, R., Williams, R.W., 2018. New determination of the 229Th half-life. J. Radioanal. Nucl. Chem. 318, 515–525. https://doi.org/10.1007/s10967-018-6032-9

Güttler, B., Rienitz, O., Pramann, A., 2019. The Avogadro Constant for the Definition and Realization of the Mole. Ann. Phys. 531, 1800292. https://doi.org/10.1002/andp.201800292

He, M., Shen, H., Shi, G., Yin, X., Tian, W., Jiang, S., 2009. Half-life of 151 Sm remeasured. Phys. Rev. C 80, 64305. https://doi.org/10.1103/PhysRevC.80.064305

IUPAC, n.d. Atomic Weight of Uranium | Commission on Isotopic Abundances and Atomic Weights.

Jaffey, A.H., Flynn, K.F., Glendenin, L.E., Bentley, W.C., Essling, A.M., 1971. Precision measurement of half-lives and specific activities of U-235 and U-238. Phys. Rev. C 4, 1889–1906. https://doi.org/10.1103/PhysRevC.4.1889

Jerome, S., Bobin, C., Cassette, P., Dersch, R., Galea, R., Liu, H., Honig, A., Keightley, J., Kossert, K., Liang, J., Marouli, M., Michotte, C., Pommé, S., Röttger, S., Williams, R., Zhang, M., 2019. Half-life determination and comparison of activity standards of 231Pa. Appl. Radiat. Isot. 108837. https://doi.org/10.1016/J.APRADISO.2019.108837

Kossert, K., Jörg, G., Gostomski, C.L. v., 2013. Experimental half-life determination of 176Lu. Appl. Radiat. Isot. 81, 140–145. https://doi.org/10.1016/J.APRADISO.2013.03.033

Lindahl, P., Olszewski, G., Eriksson, M., 2021. Performance and optimisation of triple quadrupole ICP-MS for accurate measurement of uranium isotopic ratios. J. Anal. At. Spectrom. 36, 2164–2172. https://doi.org/10.1039/D1JA00177A

Ludwig, K.R., 2003. Mathematical-statistical treatment of data and errors for230Th/U geochronology. Rev. Mineral. Geochemistry 52, 631–656. https://doi.org/10.2113/0520631

MacDonald, C.M., Cornett, R.J., Charles, C.R.J., Zhao, X.L., Kieser, W.E., 2016a. Measurement of the Cs 135 half-life with accelerator mass spectrometry and inductively coupled plasma mass spectrometry. Phys. Rev. C 93, 14310. https://doi.org/10.1103/PhysRevC.93.014310

MacDonald, C.M., Cornett, R.J., Charles, C.R.J., Zhao, X.L., Kieser, W.E., 2016b. Measurement of the Cs 135 half-life with accelerator mass spectrometry and inductively coupled plasma mass spectrometry. Phys. Rev. C 93, 14310. https://doi.org/10.1103/PhysRevC.93.014310

Nedjadi, Y., Bailat, C., Caffari, Y., Froidevaux, P., Wastiel, C., Kivel, N., Guenther-Leopold, I., Triscone, G., Jaquenod, F., Bochud, F., 2012. A new measurement of the half-life of 166mHo. Appl. Radiat. Isot. 70, 1990–1996. https://doi.org/10.1016/J.APRADISO.2012.02.063

Parsons-Davis, T., Wimpenny, J., Keller, C.B., Thomas, K., Samperton, K.M., Renne, P.R., Mundil, R., Moody, K., Knight, K., Kristo, M.J., Williams, R., 2018. New measurement of the 238U decay constant with inductively coupled plasma mass spectrometry. J. Radioanal. Nucl. Chem. 318, 711–721. https://doi.org/10.1007/s10967-018-6148-y

Pommé, S., 2015. The uncertainty of the half-life. Metrologia 52, S51--S65. https://doi.org/10.1088/0026-1394/52/3/S51

Russell, B., García-Miranda, M., Ivanov, P., 2017. Development of an optimised method for analysis of 90Sr in decommissioning wastes by triple quadrupole inductively coupled plasma mass spectrometry. Appl. Radiat. Isot. 126, 35–39. https://doi.org/10.1016/J.APRADISO.2017.01.025

Sawant, R.M., Rastogi, R.K., Chaudhuri, N.K., 1998. Study on the extraction of U(IV) relevant to PUREX process. J. Radioanal. Nucl. Chem. 229, 203–206. https://doi.org/10.1007/BF02389477

Schoene, B., Crowley, J.L., Condon, D.J., Schmitz, M.D., Bowring, S.A., 2006. Reassessing the uranium decay constants for geochronology using ID-TIMS U-Pb data. Geochim. Cosmochim. Acta 70, 426–445. https://doi.org/10.1016/j.gca.2005.09.007

Schön, R., Winkler, G., Kutschera, W., 2004. A critical review of experimental data for the half-lives of the uranium isotopes U-238 and U-235. Appl. Radiat. Isot. 60, 263–273. https://doi.org/10.1016/J.APRADISO.2003.11.027

Taylor, P.D.P., de Bièvre, P., Walder, A.J., Entwistle, A., 1995. Validation of the analytical linearity and mass discrimination correction model exhibited by a multiple collector inductively coupled plasma mass spectrometer by means of a set of synthetic uranium isotope mixtures. J. Anal. At. Spectrom. 10, 395–398. https://doi.org/10.1039/JA9951000395

Varga, Z., Nicholl, A., Wallenius, M., Mayer, K., 2016. Remeasurement of 234 U Half-Life. Anal. Chem. 88, 2763–2769. https://doi.org/10.1021/acs.analchem.5b04370

Villa, I.M., Bonardi, M.L., De Bièvre, P., Holden, N.E., Renne, P.R., 2016. IUPAC-IUGS status report on the half-lives of U-238, U-235 and U-234. Geochim. Cosmochim. Acta 172, 387–392. https://doi.org/10.1016/J.GCA.2015.10.011

Villa, I.M., Holden, N.E., Possolo, A., Ickert, R. Ben, Hibbert, D.B., Renne, P.R., Bonardi, M.L., De Bièvre, P., 2022. IUGS-IUPAC recommendations and status reports on the half-lives of 87Rb, 146Sm, 147Sm, 234U, 235U, and 238U (IUPAC Technical Report). Pure Appl. Chem. 94, 1085–1092. https://doi.org/10.1515/PAC-2021-1202/MACHINEREADABLECITATION/RIS

Warwick, P E, Russell, B.C., Croudace, I.W., 2019. Evaluation of inductively coupled plasma tandem mass spectrometry for radionuclide assay in nuclear waste characterisation. https://doi.org/10.1039/c8ja00411k

Warwick, Phillip E, Russell, B.C., Croudace, I.W., Zacharauskas, Z., 2019. Evaluation of inductively coupled plasma tandem mass spectrometry for radionuclide assay in nuclear waste characterisation. J. Anal. At. Spectrom. https://doi.org/10.1039/C8JA00411K

Yang, J., Zhang, S., Ding, Y., Shu, F., Zhang, J., 2010. A new value of 93Zr half-life. Radiochim. Acta 98, 59–63. https://doi.org/10.1524/ract.2010.1678.

Measuring mass attenuation coefficients for materials with unknown composition by performing transmission measurements with a HPGe detector for X-rays and low-energy gamma rays.

Leen Verheyen[a*], Michel Bruggeman[a], Anaëlle Gassien[b]

[a] SCK CEN, Belgium
[b] Université de Bordeaux, France

Abstract

In gamma-ray spectrometry, analyzing low-energy gamma-emitting nuclides such as ^{210}Pb, ^{129}I, and ^{234}Th requires careful consideration due to the sample's self-attenuation, which is influenced by the specific elemental composition of the sample material. In this study, we present a novel non-collimated transmission measurement method utilizing a range of gamma- and X-rays, spanning 13.6 - 302 keV to acquire attenuation data. Subsequently, we apply sample self-attenuation corrections using efficiency transfer through EFFTRAN, incorporating the attenuation data derived from the transmission measurements.

* Corresponding author, e-mail address: leen.verheyen@sckcen.be

1. Introduction

Gamma-ray spectrometry is a technique that is widely used to quantify radionuclides in various applications. In order to quantify radionuclides using a gamma-ray spectrometry system, several calibrations of the spectrometer are necessary. The energy calibration sets up, this is the relation between the channel numbers of the gamma-ray spectrum and the corresponding energy of the full energy peaks of the gamma-rays that make up the spectrum. Peak shape calibrations define the parameters and equations necessary for a mathematical description of the peak shape, which is necessary for determining peak areas. The counting efficiency calibration sets the relation between the net peak areas of a certain radionuclide and its radioactivity or radioactivity concentration for a sample for which the spectrum was recorded. The counting efficiency calibration is dependent on many parameters, such as gamma-ray energy, the specific counting geometry in which the spectrum is acquired and the gamma-ray attenuation by the sample.

The counting efficiency calibration is commonly set up by an experiment in which a known radioactivity is measured in identical or similar conditions as the sample with the unknown radioactivity to be measured. Any difference between the calibration conditions and the conditions of the actual measurement of a sample may introduce a measurement bias. In general, samples and counting conditions may be complex in gamma-ray spectrometry, but in the application of laboratory analyses on small counting beakers the different sample parameters are generally well known.

Counting efficiency calibration is a crucial step in gamma-ray analysis, and both experimental and computer simulation approaches are widely used. While computer simulations can accurately calculate the counting efficiency by modeling gamma-ray interactions in the sample and detector, obtaining unbiased results requires precise information for all relevant parameters defining the sample and the detector. To obtain this information generally also experiments with well-known gamma sources are needed for benchmarking and fine-tuning the simulation model.

Efficiency transfer is commonly used to correct for known deviations in the counting geometry of the actual sample compared to the reference calibration. Correction factors (transfer factors) are obtained through analytical or computer simulation techniques.

Efficiency transfer is commonly used in laboratory analyses of small samples for which pre-defined efficiency calibrations were set up. Correction factors are typically needed to correct for differences in e.g. the sample filling height, sample composition and mass density of the sample material. These are all parameters related to the sample self-attenuation of the gamma rays.

At low energy (e.g. below 100 keV) the attenuation of gamma-rays in matter is a function of the chemical composition of the sample material. With no appropriate correction for sample self-attenuation, that can be different from the attenuation in the calibration sample, and with the assay of low-energy gamma emitters measurement results will be generally biased. The attenuation of low-energy gamma-rays strongly depends on the composition of the attenuating material, making it challenging to analyze radionuclides such as ^{210}Pb, ^{241}Am, ^{234}Th and ^{129}I. To deal with sample self-attenuation commonly, separate measurements of the attenuation properties of the material are conducted, or its chemical composition is identified (e.g. by energy dispersive X-ray analysis) from which the attenuation coefficients are then obtained from the XCOM database (Berger, 2010).

An effective solution to address the problem of unknown gamma attenuation at low energy in gamma-ray spectrometry was proposed by Cutshall in 1983 (Cutshall, 1983). The method involves computing an energy-specific correction factor obtained from the transmission through the sample at the same energy. This straightforward approach enables a more accurate analysis involving low-energy gamma-rays. Cutshall's correction factor computation method assumes that gamma-rays travel in parallel trajectories through the sample, as would be the case when the radiation source and detector are infinitely far apart. However, in practice the distance between the sample and detector is short (e.g. in applications for analysis of environmental radioactivity). Consequently gamma-rays travel in fan beams and the interpretation model is strictly not valid. Though since both, transmission and correction factor are used in a relative way in certain conditions still acceptable correction for sample self-attenuation are obtained depending on the counting geometry (Jodlowski, 2016) (Iurian, 2018).

Several attempts have been made to improve the Cutshall method by computing geometry-specific corrections to the basic correction of the method (Jodlowski, 2016). These corrections aim

to account for the non-parallel nature of gamma-rays in close proximity to the detector. The accuracy of the correction depends on the specifics of the counting geometry and can be validated through experiments with well-known gamma sources.

Gamma-ray spectrometry analyses of low-energy gamma-rays, requires the use of mass attenuation coefficients that are specific to the sample material. Experimental determination of these coefficients using a parallel beam of gamma-rays typically involves collimators and a relatively active transmission source to achieve acceptable counting statistics. Spectra obtained with the collimated transmission source may show artifact peaks resulting from low-incidence-angle scattering in the collimator, complicating peak analysis. As a result, these experiments need to be carefully designed and may require more resources compared to the Cutshall approach.

The determination of attenuation coefficients with non-parallel trajectories of gamma-rays from a transmission source can also be realized by computation. Using the computer program GESPECOR (Sima O., 2001) one can compute the linear attenuation coefficients for a predefined sample geometry and experimental value for the ratio of detector response relative to that of a non-attenuating sample for a transmission point source.

We propose a method based on transmission without collimation that involves establishing a calibration curve representing the linear attenuation coefficient of the material relative to that of water as a function of the relative count rate obtained from a transmission experiment for this material relative to water. Water is often used as a reference sample matrix due to its ease of preparation and common use in experimental reference efficiency calibrations. This approach can also be used to determine attenuation coefficients for other transmission source configurations than a points source e.g. using a surface source.

Figure 1 *Figures*shows the setup used to measure the transmission spectra using a point source. The sample used for obtaining the transmission data is not necessary the same as the one used for assay of the radioactivity content.
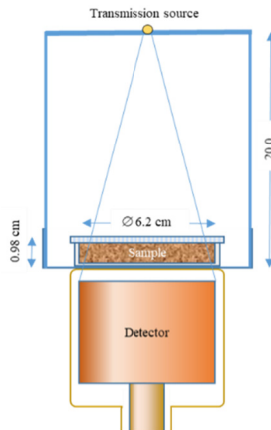

Figure 1: Setup used to measure the transmission spectra. A sample specific for the transmission analysis is considered.

Similar methods for the determination of attenuation coefficients for the correction of sample self-attenuation were already presented in the past by Byun (Byun J., 2015) and later also by Lee (Lee J.B., 2020). However, all determined the attenuation coefficients for selected materials directly from the photon transmission ratio relative to a non-attenuating sample. Moreover, the energies below 100 keV were limited to 46.5 keV and 59.5 keV respectively and only total attenuation coefficients were determined. We show that the method can be extended to energies as low as 13 keV, and suggest using more transmission data at low energy to obtain a more dense energy grid to well

represent the variation of the attenuation coefficients at low energies. A dense energy grid for attenuation data allows a direct use for efficiency transfer without prior need for interpolation. We demonstrate that the method can be used to determine the total attenuation as well as total attenuation minus coherent scattering.

2. Materials and methods

2.1 *Materials used for transmission*

The choice of water as a reference sample material in the determination of relative linear attenuation coefficients is driven by the fact that the reference counting efficiency calibration is commonly set up for a water matrix. Hence efficiency transfer factors are then also relative to the water matrix, next to differences in other sample parameters for which efficiency transfer is required. The experimental set-up to determine attenuation coefficients involves the measurement of the relative count rate $\frac{r_A}{r_w}$ obtained by transmitting gamma-rays of energy E from an external source through the material of interest (material A), normalized to the count rate obtained by transmitting gamma-rays through water (material W), both measured in a fixed predefined geometry. The relative linear attenuation coefficients can then be calculated from the relative count rates using a mathematical relation

$$\frac{\mu_A(E)\rho_A^{-1}\rho_A'}{\mu_w(E)\rho_w^{-1}\rho_w'} = F_{cal}\left(\frac{r_A}{r_w}\right) \tag{1}$$

In which $(\mu_A(E)\rho_A^{-1})$ is the mass attenuation coefficients at a specified energy E and ρ_A' is the apparent density of the material A. r_A is the count rate (in counts per second) measured with the transmission source through the material A at the energy E. F_{cal} is a calibration function correlating the relative attenuation data to the relative count rates. The calibration function is energy and detector specific, but may be more generally applicable for similar detectors. In the conditions where the sample diameter is larger than the detector crystal diameter, a good approximation for the calibration function is given by:

$$\frac{\mu_A(E)\rho_A^{-1}\rho_A'}{\mu_w(E)\rho_w^{-1}\rho_w'} \cong C \ln\left(\frac{r_A}{r_w}\right) + 1 \tag{2}$$

Equation (2) is exact for a parallel beam of photons that runs perpendicular through the testing materials and for a detector with a constant detection efficiency over its surface. In this special condition, the ratio of count rates can be expressed as:

$$\frac{r_A}{r_w} = \frac{\exp(-\mu_A(E)\rho_A^{-1}\rho_A'L)}{\exp(-\mu_w(E)\rho_w^{-1}\rho_w'L)} \tag{3}$$

Where the right-hand side of the equation (3) gives the ratio of attenuation of the beam with L the thickness of the sample material. This yields

$$-\ln\left(\frac{r_A}{r_w}\right) = \left(\frac{\mu_A(E)\rho_A^{-1}\rho_A'}{\mu_w(E)\rho_w^{-1}\rho_w'} - 1\right)\mu_w(E)\rho_w^{-1}\rho_w'L \tag{4}$$

From which it follows that the constant in equation (2) equals $C = -(\mu_w(E)\rho_w^{-1}\rho_w'L)^{-1}$ for a parallel beam of photons.

In the more general situation where the photons travel not in a parallel beam perpendicular to the sample surface but in a fan beam and where the detection efficiency is a function of the angle by which the gamma-rays enter the detector, the ratio of count rates can be expressed as:

$$\left(\frac{r_A}{r_w}\right) = \frac{\int_0^{\theta_{max}} I(\theta)\varepsilon(\theta)\exp\left(-\mu_A(E)\rho_A^{-1}\rho_A'l(\theta)\right)sin(\theta)\,d\theta\,d\varphi}{\int_0^{\theta_{max}} I(\theta)\varepsilon(\theta)\exp(-\mu_w(E)\rho_w^{-1}\rho_w'l(\theta))sin(\theta)\,d\theta\,d\varphi} \tag{5}$$

In which $I(\theta)$ is the photon intensity in the direction given by the angle θ, $\varepsilon(\theta)$ is the detection efficiency for photons entering the detector under an angle θ and $l(\theta)$ is the path length the photons travel through the sample material and the integral is over the solid angle Ω subtended by the detector crystal. According to Fig. 1, the most inclined photon trajectories through the sample correspond to an angle of less than 9°. Thus, the longest trajectories differ from the thickness of the sample by about 1.2%. Therefore, equation (4) should describe with a good approximation the present measurements.

In the approximation that $I(\theta)\varepsilon(\theta)$ is independent of the angle θ, equation (5) has a solution of the form

$$\left(\frac{r_A}{r_w}\right) = \frac{\exp(-\mu_A(E)\rho_A{}^{-1}\rho_A'L)}{\exp(-\mu_W(E)\rho_W{}^{-1}\rho_W'L)} \cdot \frac{\dfrac{\left(1 - \exp(-\mu_A(E)\rho_A{}^{-1}\rho_A'\Delta)\right)}{\mu_A}}{\dfrac{\left(1 - \exp(-\mu_W(E)\rho_W{}^{-1}\rho_W'\Delta)\right)}{\mu_W}}$$

$$(6)$$

In which $\Delta = L(\theta\_max) - L$ is the difference between the maximum path length and the minimum path length of the photons of the transmission source in the sample. The equation (6) generally does not give a solution such that:

$$\ln\left(\frac{r_A}{r_w}\right) = \left(\frac{\mu_A(E)\rho_A{}^{-1}\rho_A'}{\mu_w(E)\rho_w{}^{-1}\rho_w'} - 1\right)C$$

With C a constant.

The experimental determination of the mass attenuation coefficients for a set of materials relies on the photon cross section data for the elements and compounds in those materials, which can be readily obtained from the XCOM database available on the NIST website (Berger M.J., 2010).

When selecting materials for the experimental determination of the attenuation properties, it is important to ensure that the materials are of known composition and free of impurities. For instance, materials like Polyvinyl Chloride (PVC) may contain a complex mixture of additives. Hence the base chemical formula $(C_2H_3Cl)_n$ is inappropriate for this experiment as the precise composition of such plastics is often unknown.

The Table 1 specifies the different materials we used to set up the calibration function F_{cal}. The table specifies the chemical formula used in XCOM, the apparent density ρ_A' and the mass attenuation coefficients $\mu_A(E)\rho_A{}^{-1}$ at the different energies E emitted by the transmission sources.

The transmission through materials specified in Table 1 were measured in a sample container made of polystyrene with an inner diameter of 6.2 cm and a sample height of 0.98 cm (see Figure 1). Massive solid materials were machined to fit in the container with a height of 0.98 cm. Fine powders and liquids were poured in the sample container at the reference thickness of 0.98 cm. The apparent density of the materials has been determined by weighing the material and using the computed volume filled by the material. For powders the apparent density may depend on the way the powder is compacted, several measurements, involving refilling of the sample container and weighing were used to determine an average density and uncertainty of this value. For the machined materials, the dimensions of the machined cylinder and its weight were used to compute the density.

Table 1: Mass attenuation coefficients for the different energies and materials with coherent scattering.

| Material | Formula | ρ g/cm³ | E(keV) | | | | | | | | | |
			13.6	20.8	26.3	31.0	33.0	35.1	53.2	59.5	81.0	302.9
Water	H_2O	1	2.19	0.7	0.47	0.36	0.3	0.31	0.22	0.21	0.2	0.12
Sodium carbonate	Na_2CO_3	1.2	3.93	1.2	0.69	0.48	0.4	0.38	0.23	0.21	0.2	0.1
Di-ammonium hydrogen citrate	$C_6H_{14}N_2O_7$	0.83	1.75	0.6	0.4	0.32	0.3	0.28	0.2	0.19	0.2	0.11
Sodium Chloride	$NaCl$	1.36	16.8	4.9	2.58	1.61	1.4	1.17	0.45	0.36	0.2	0.10
Oxalic Acid Dihydrate	$C_2H_6O_6$	1.14	2.06	0.7	0.44	0.34	0.3	0.29	0.21	0.2	0.2	0.11
PMMA	$C_5O_2H_8$	1.2	1.42	0.5	0.36	0.29	0.3	0.26	0.2	0.19	0.2	0.11
Aluminium	Al	2.74	13.9	0.1	2.17	1.37	1.2	1.01	0.41	0.34	0.2	0.11
Teflon - PTFE	C_2F_4	2.21	2.76	0.9	0.53	0.38	0.3	0.31	0.2	0.19	0.2	0.10
PVDF	$C2H2F2$	1.8	2.36	0.8	0.48	0.35	0.3	0.3	0.2	0.19	0.2	0.11
PE HD 1000	$C2H4$	0.96	0.93	0.4	0.31	0.26	0.3	0.24	0.2	0.2	0.2	0.12
Polyoxoxy methylene	$CH2O$	1.43	1.73	0.61	0.40	0.31	0.29	0.27	0.20	0.19	0.17	0.11
Air			2.01	0.68	0.43	0.33	0.30	0.28	0.20	0.19	0.17	0.11
PP	$C3H6$	0.95	0.93	0.41	0.31	0.26	0.25	0.24	0.20	0.20	0.18	0.12
Carbon	C	1.1	1.03	0.41	0.30	0.25	0.24	0.23	0.18	0.18	0.16	0.10
PETP	$C10H8O4$	1.39	1.46	0.5	0.36	0.29	0.3	0.26	0.20	0.19	0.20	0.11

2.2 Transmission sources

Two sources, ^{241}Am (40 kBq) and ^{133}Ba (10 kBq) were sequentially used to measure the transmission at several energies through the selected materials in the set-up outlined in Figure 1. Since for most of the X-rays of these sources rather a range of energies is reported in literature instead of single energies, we specified their energies by the centroid of the peaks observed in the gamma-ray spectrum. For ^{241}Am the energies considered are: 13 keV, 20.8 keV, 26.1 keV, 33.0 keV and 59.5 keV. For ^{133}Ba the energies considered are 31.0 keV, 35.0 keV, 53.0 keV, 81.0 keV and 302.6 keV.

The transmission measurements were made with a REGe detector having a carbon composite window and a relative efficiency of 28 %. The energy resolution, full width at half maximum (FWHM) at 59 keV is 0.88 keV.

The measurements were made with the sample container put on a sample holder made of polystyrene (1 mm thick) and with the source at a distance of 20.1 cm from the detector end cap using a cylindrical spacer closed at one end and with a hole in the center of the end piece in which the transmission source is position, one measurement per sample. Measurement time was variable, taking care of enough counting statistics in the full energy peaks.

Determination of the net peak areas from the spectra of the different energies and materials considered in Table 1, were done by Genie 2000 (version 3.4.1) with a valid peak shape calibration. Due to the fact that multiplets of X-rays compose certain parts of the spectrum, peak area fitting was made by using a variable FWHM to obtain the net area of unresolved multiplets. The uncertainty on the computed count rate was taken directly from Genie. This uncertainty only accounts for the statistical uncertainty as it is modeled in the software, but does not account for possible bias in the peak area because the actual peak shape and continuum under the peaks do not exactly correspond to the model used in the spectrum analysis software.

The uncertainty on the experimentally determined attenuation coefficients cannot directly be used for an uncertainty estimation of the efficiency transfer factors by EFFTRAN. Hence to evaluate uncertainty on the efficiency transfer factors when using experimentally determined attenuation parameters instead of data generated by XCOM a separate uncertainty evaluation needs to be performed. This can be done by evaluating transfer factors computed by EFFTRAN while varying the attenuation data.

2.3 Efficiency transfer

The aim of the determination of the attenuation coefficients is for their use in efficiency transfer to correct for sample self-attenuation. This requires setting up a material file for the sample material with a data structure equal to the one of the data files directly obtained from XCOM. For efficiency transfer such files are prepared by using the standard energy grid of XCOM. This defines the energy values for which attenuation data are provided. EFFTRAN then uses log-log interpolation to compute efficiency transfer factors at other energies than those provided by the standard grid. In case of materials where K-edges appear in the considered energy range, these are also included in these material files. In the 10 keV to 100 keV energy range, the standard grid of XCOM includes the energies: 10, 15, 20, 30, 40, 50, 60, 80 and 100 keV. To set up a material file representing the attenuation data obtained from the calibration curves, an existing XCOM file can be edited to replace the standard grid energies by the photon energies used in the transmission and by replacing the attenuation data with the experimentally obtained attenuation data. The set of energies to replace those of XCOM are then 13.0, 20.8, 26.1, 31.0, 33.0, 53.0, 59.5, 81.0 and 302.6 keV. The values above 300 keV can then be kept equal to those of the standard materials used in efficiency transfer e.g. the generic materials.
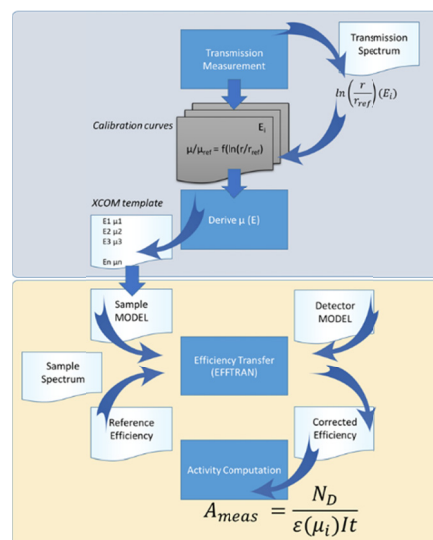

Figure 2: Principle of using experimentally determined attenuation data in an XCOM material file to be used for efficiency transfer with EFFTRAN.

Figure 2 demonstrates the principle of utilizing transmission data acquired at multiple low energies along with efficiency transfer through EFFTRAN. By computing the efficiency transfer factors utilizing a material file with a template identical to an XCOM data file, but with the attenuation coefficients replaced by the experimentally derived attenuation data, the activity of a sample with an unknown matrix composition can be determined from the sample spectrum. In sample compositions where elements of high atomic number dominate, the method may fail when X-ray fluorescence peaks are produced at the position of the transmission energies where they will interfere with the transmission spectrum.

In efficiency transfer the total attenuation coefficient minus coherent scattering is generally used to calculate corrections for sample self-attenuation of gamma rays. The total attenuation coefficient includes all possible interactions between the gamma rays and the matter. In coherent scattering, the gamma rays interact with the entire atom and change their direction without losing energy. If in such a coherent scattering event the scattered gamma-ray still enters the detector it is not contributing to the overall attenuation by the sample. Since coherent scattering does not result in any energy loss, it is typically not considered in the calculation of gamma-ray attenuation in the sample.

At low energies (< 100 keV) however, coherent scattering becomes more prominent as the energy of the photon decreases. In coherent scattering, the photon interacts with the entire atom and changes direction without losing energy. This is in contrast to incoherent scattering, where the photon interacts with individual electrons and loses energy in the process. The effect of coherent scattering increases with; decreasing photon energy, increasing distance of penetration in the medium and increasing atomic number of the atoms on which the scattering occurs (Cramer et all, 1989).

At the lowest energies, the small-angle coherent scattering deflection is the greatest, and the photons tend to be scattered radially outward more quickly than in the case where there would be no coherent scattering as it has been demonstrated by Cramer (Cramer S.N., 1989). Therefore, it is important to consider the effects of coherent scattering when modeling the transport of gamma rays at low energies. Figure 3 shows the relative difference between total attenuation coefficients with and without coherent scattering as a function of gamma-ray energy for different materials.

In the energy range 20 to 50 keV the relative difference is of the order of 10 % and is a peaked function of energy.
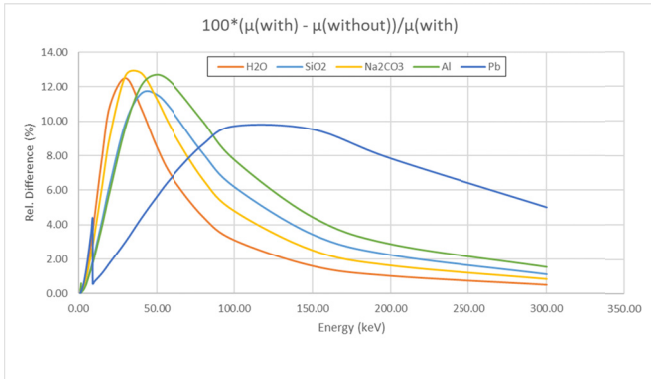

Figure 3: Relative difference between total and total – coherent scattering coefficients as a function of photon energy for different materials.

When applying efficiency transfer to correct for deviations between the actual counting efficiency and the reference efficiency calibration conditions, there is also the need to estimate the uncertainty that goes with the efficiency transfer. However a clear source of uncertainty is related to the accuracy with which the attenuation coefficients of the sample material can be defined. Since our method relies on the data available in the XCOM database it is a first source of uncertainty to consider. The material-independent energy-independent uncertainty on the photon mass attenuation coefficients given by XCOM is estimated 0.5 % (68 % confidence) for photon energies above 100 keV (ESM Ali, 2015). Below 100 keV the uncertainty is estimated to be larger (ESM Ali, 2015). It is generally difficult to compare the theoretically predicted values for photon attenuation with experimental data because often scattering of photons complicates the interpretation of data. An inter comparison between the theoretical methods to compute mass attenuation coefficients, XCOM and FFAST (X-Ray Form Factor, Attenuation, and Scattering Tables) shows that the agreement between both methods for photon energies between 10 and 100 keV is of the order of a few percent depending on the atomic mass of the attenuation material (Saloman E.B., 1986).

Calibration functions $F_{cal}(E)$ at the different transmission energies E where set up for both, total attenuation and total attenuation minus coherent scattering. However in efficiency transfer with EFFTRAN total minus coherent scattering coefficients are used as these are read by the software directly from the data files produced by XCOM. Accounting for the findings made by Cramer (Cramer S.N., 1989) however, it is clear that at the low energies (below 100 keV) the effects of coherent scattering of photons may not be fully excluded. Since we aim only at measuring attenuation coefficients relative to water, one may expect that the impact of coherent scattering will level out since it will occur in both materials, in the material under study and in water.

The Figure 4 shows the difference of efficiency transfer with EFFTRAN using respectively total attenuation coefficients and total attenuation minus coherent scattering for 3 different configurations of pillbox samples with a diameter of 60 cm and different heights of respectively 20, 40 end 60 mm. The efficiency transfer with total attenuation coefficients with EFFTRAN was realized by editing the XCOM files used by EFFTRAN by putting the total attenuation data in the column read by EFFTRAN.

As can be seen in Figure 4 different results are obtained using the one or the other data set. The deviations are largest below 100 keV and are larger for the thickest sample. In this example, the efficiency transfer factors were computed for a material defined as

dirt 1, that was given a density of 1 g/cm³ with a composition with mass fractions: H:0.022   O:0.575   Al:0.085   Si:0.262   Fe:0.056 relative to water. The deviations between the two computations was of the order of 2 %.
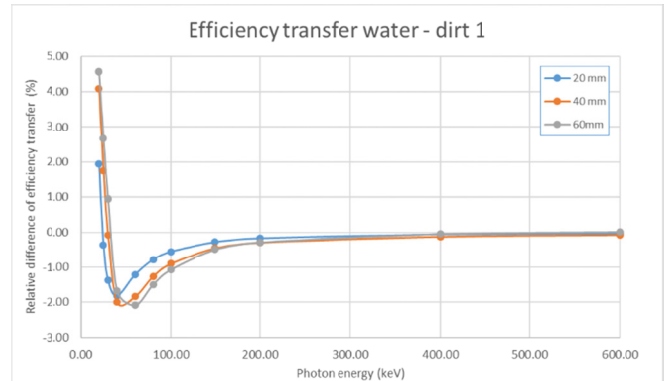

Figure 4: Relative difference of efficiency transfer made by EFFTRAN using total attenuation coefficients and total minus coherent scattering for 3 different geometries (sample heights) from water to dirt 1 material.

Figure 5 shows the relative difference between the ratios of total attenuation coefficients and total attenuation minus coherent scattering for the material used for the efficiency transfer:

$$Rel\ difference = \ 100\left(\frac{\frac{\mu_{Dirt}^{t-coh}}{\mu_{w}^{t-coh}} - \frac{\mu_{Dirt}^{t}}{\mu_{w}^{t}}}{\frac{\mu_{Dirt}^{t}}{\mu_{w}^{t}}}\right).$$

The maximum deviations observed for the attenuation data correspond to those observed in the efficiency transfer factors.
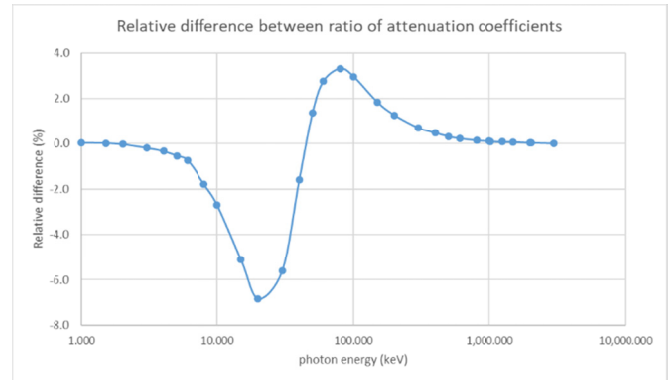

Figure 5: Relative difference between ratios of attenuation coefficients of total μ and total μ - coherent scattering for the material dirt 1 relative to water.

As is also considered in the work of Lee (Lee J.B., 2020) and (Sima, 2002) it is important to design the transmission set up without collimation in such a way that true coincidence summing (TCS) is excluded. A source detector configuration as was used by Cutshall, where the transmission source is close to the detector will not exclude TCS effects when using sources with radionuclides which are subject to TCS. Hence this configuration is not appropriate for the method described here. Theoretically, transmission measurements could be corrected for TCS effects however the TCS correction itself also depends on the self-attenuation properties of the material interacting with the gamma-rays. An iterative approach in which the corrections for TCS are

gradually refined using improved values for the attenuation coefficients from a previous iteration step could be used to make TCS corrections. Such an approach would surely complicate the determination of attenuation parameters and would increase its uncertainty. Hence it is advised to exclude TCS effects by measuring with the transmission source at a distance of at least 20 cm. The TCS effects for ^{241}Am are rather small but the gamma-rays from ^{133}Ba will surely be subject to TCS effects when the source to detector distance is below 20 cm. This also holds for the determination of attenuation coefficients using the special option of GESPECOR discussed earlier.

3. Results

3.1 *The calibration curves.*

With the selected materials and sources, count rates measured ranged from 46 counts/s to 0.005 counts/s for the least, respectively most attenuating material.

For each of the photon energies 13 keV, 20.8 keV, 26.1 keV, 31.0 keV, 33.0 keV, 35.0 keV, 53.0 keV, 59.5 keV, 81.0 keV and 302.6 keV and with the XCOM data computed for the different calibration materials given in Table 1, the different calibration curves giving the relative attenuation as a function of the logarithm of the relative count rate obtained from the transmission measurements were determined. A calibration curve was set up respectively for the total mass attenuation coefficients and one for the total mass attenuation minus the coherent scattering (only those for total attenuation are shown here).

The results and fittings of the calibration function at the different energies are shown in the figures 6 to 15 for the total attenuation coefficients, with d the density of the material. For each point in the calibration curve uncertainty is given on the relative count rate and on the relative linear attenuation coefficients. The latter are computed from the uncertainty on the ratio of apparent densities of respectively the reference material (water) and that of the calibration material. Uncertainty on the mass attenuation coefficients obtained from XCOM was not considered since no specific uncertainty is available as discussed in the materials and method section.
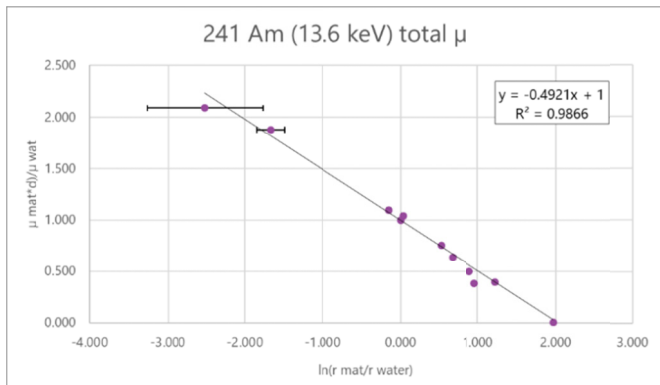

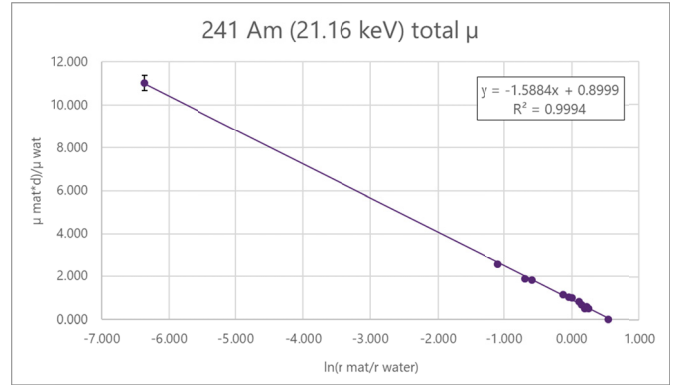Figure 6: Calibration curve for the total attenuation coefficient at 13.6 keV.

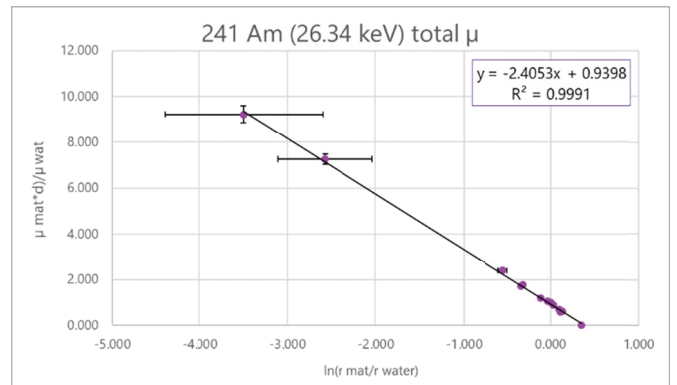Figure 7: Calibration curve for the total attenuation coefficient at 21.16 keV.

Figure 8: Calibration curve for the total attenuation coefficient at 26.34 keV.
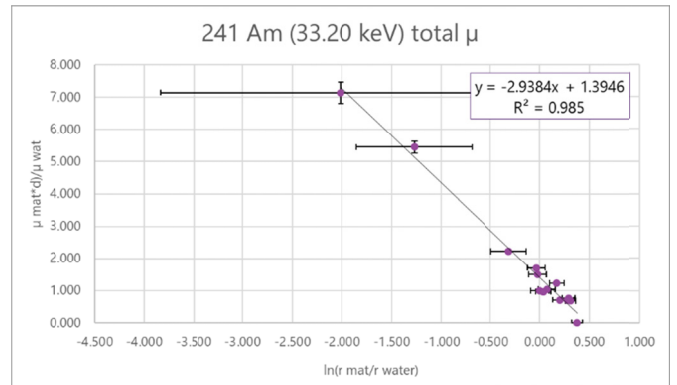

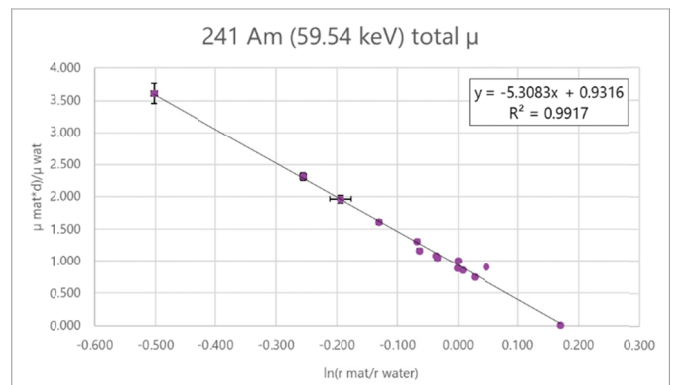Figure 9: Calibration curve for the total attenuation coefficient at 33.20 keV.

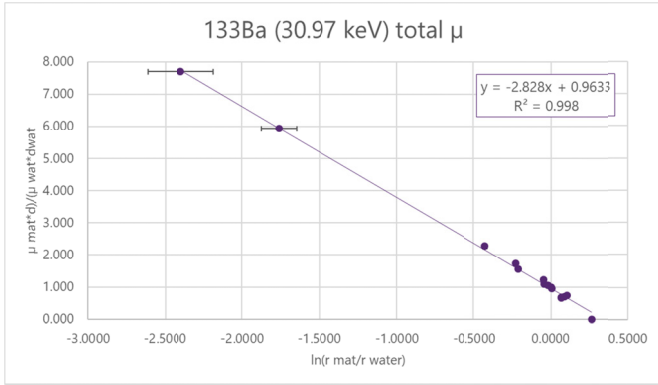Figure 10: Calibration curve for the total attenuation coefficient at 59.54 keV.

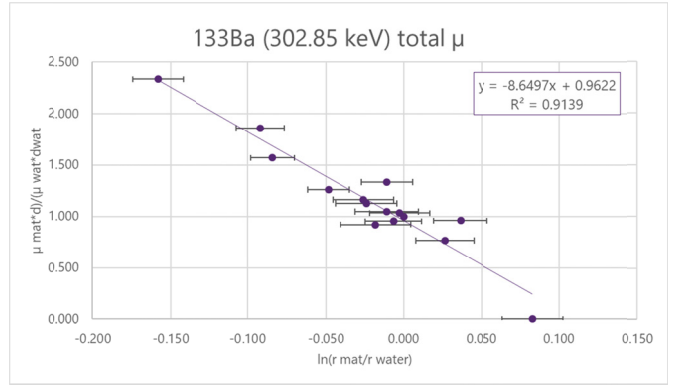*Figure 11: Calibration curve for the total attenuation coefficient at 30.97 keV.*
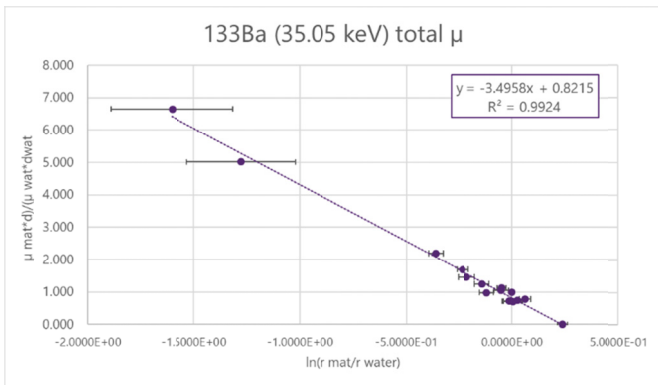

Figure 12: Calibration curve for the total attenuation coefficient at 35.05 keV.
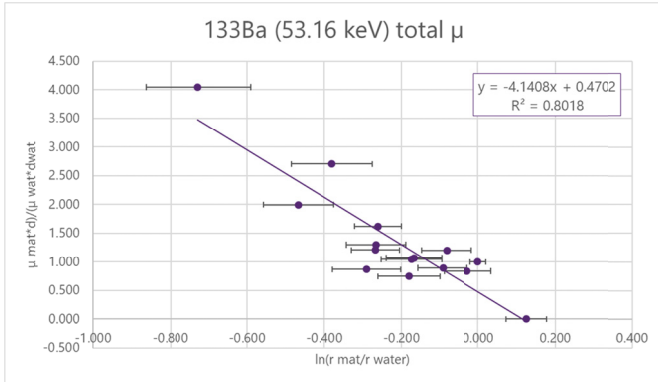

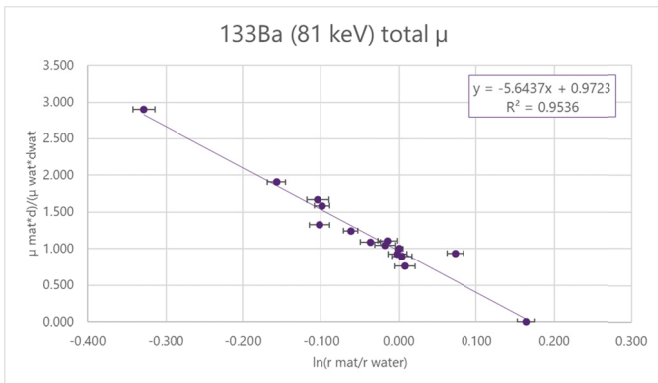*Figure 13: Calibration curve for the total attenuation coefficient at 53.16 keV.*

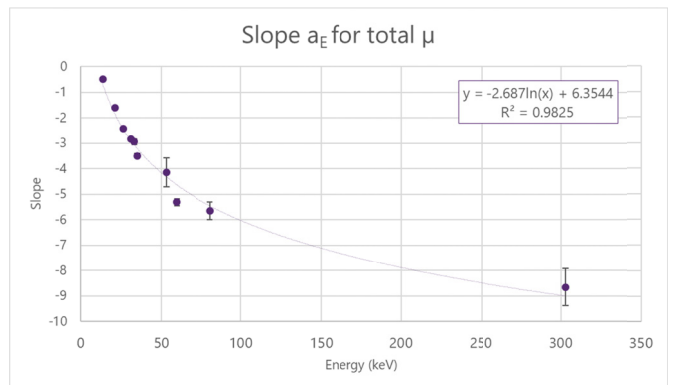*Figure 14: Calibration curve for the total attenuation coefficient at 81 keV.*

Figure 15: Attenuation curve for the total attenuation coefficient at 302.85 keV.

Each of the calibration curves was fitted with a straight line and the slope and the offset were determined using MS Excel's LINEST function and its associated statistics data from which a confidence interval can be computed (Morrison, 2014). The Figure 16 shows the evolution of the slope of the calibration function as a function of energy. The logarithmic fit is a guide to the eye only. The Figure 17 shows the offset of the calibration curve as a function of the photon energy and shows that it is scattered around 1 as is predicted by the ideal case of a parallel beam. We did not found a particular reason why the point at 59 keV has a relative large deviation on offset and slope compared to the other points. It is believed that it results from bias in the peak area determination.

Figure 16: Evolution of the slope of the linear calibration curve for total attenuation coefficient as a function of photon energy.

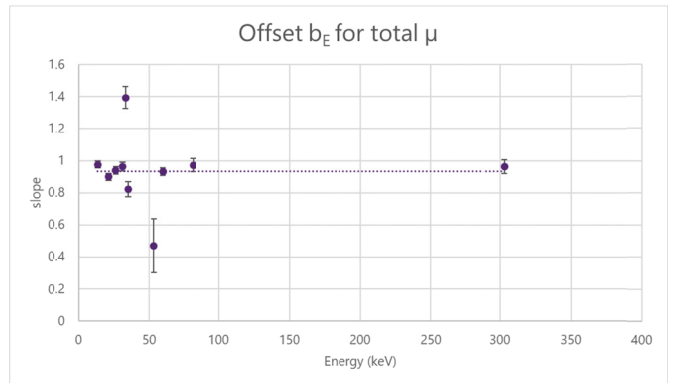*Figure 17: Offset of the linear calibration curve as a function of photon energy.*

The Figure 18 shows the confidence intervals for the calibration curve for ^{133}Ba at 30.97 keV to estimate uncertainty on the attenuation data obtained from the calibration curves.
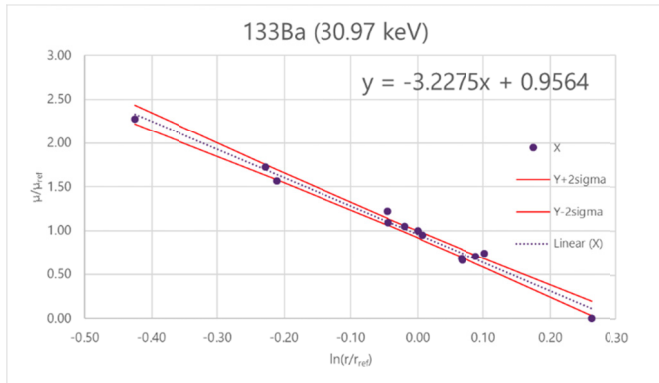

Figure 18: Example case showing confidence interval computed from the statistical information given by the LINEST function of Excel.

As explained before, the linear fit is only an approximation and the quality of fit has to be investigated for its validity and other functions may be needed for best results.

Using all the calibration curves obtained at the different transmission energies, the attenuation coefficients, both, total attenuation and total attenuation minus coherent scattering, are then obtained from:

$$\frac{\mu_A(E)}{\rho_A} = F_{cal}(E) \frac{\mu_w(E)}{\rho_w} \frac{\rho'_w}{\rho'_A} \qquad (7)$$

Where the $F_{cal}(E)$ are different for total attenuation and total minus coherent data. Uncertainty on the attenuation coefficients is estimated by considering the uncertainty obtained from the calibration curve on the attenuation data relative to water and the apparent density of the sample material for which the attenuation data are requested. It follows from:

$$\frac{\sigma^2\left(\frac{\mu_A}{\rho_A}\right)}{\left(\frac{\mu_A}{\rho_A}\right)^2} = \frac{\sigma^2(F_{cal})}{(F_{cal})^2} + \frac{\sigma^2(\rho'_w)}{(\rho'_w)^2} + \frac{\sigma^2(\rho'_A)}{(\rho'_A)^2} \qquad (8)$$

In which uncertainty on the XCOM data $\frac{\mu_w(E)}{\rho_w}$ is neglected here. The uncertainty on F_{cal} is obtained from the confidence interval computed for the count rate ratio measured. The uncertainty on the density is obtained from mass and volume evaluations of the sample materials used in the transmission experiments.

3.2 *Test on known material*

To evaluate the method, a test was conducted using a known material that was independent of the materials used for the calibration setup. Calcium Ammonium Nitrate powder ($CaH_8N_2O_{10}$) was chosen as the test material and prepared in the sample box with an apparent density of 1.1361 g/cm³. The attenuation data were obtained using equation *(7)* and the calibration functions $F_{cal}(E)$ at the different transmission energies E. The experimental data can then be compared with the XCOM data for Calcium Ammonium Nitrate. This material has a K-edge at 4 keV which outside the energy range of the method.

Figure 19 illustrates the relative difference between the measured total attenuation coefficients for $CaH_8N_2O_{10}$ and the corresponding values obtained directly from XCOM at the different transmission energies. The error bars displayed represent 68.3% confidence levels. It is worth noting that no result was obtained for the transmission at 13 keV in this particular case.

The comparison reveals that the relative difference between the experimentally determined attenuation coefficients and the reference values obtained from XCOM is generally within 6%. In most cases, this difference aligns with the reported uncertainty. However, at a few specific points e.g. at 21 keV and 81 keV, the observed deviation surpasses the uncertainty at a 95% confidence level. Based on this test case, the generalized estimated uncertainty for mass attenuation coefficients determined using this method is estimated at 5%.
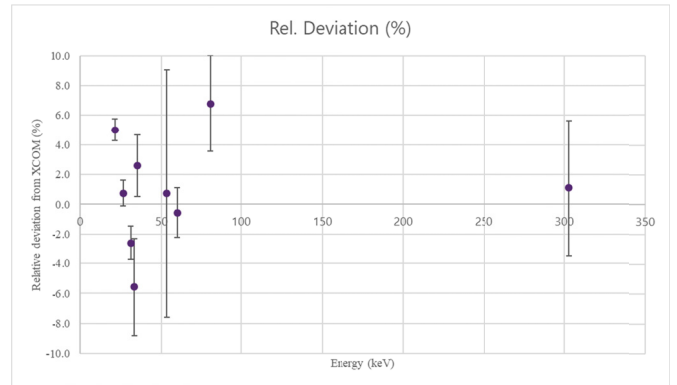

Figure 19: Comparison of total attenuation data obtained from the experiment with XCOM data for calcium ammonium nitrate.

It is important to note that the way uncertainty in the attenuation data affects efficiency transfer depends on the specific circumstances, including the sample characteristics and counting configuration. The relationship between uncertainty and efficiency transfer is influenced by these factors and may vary accordingly.

The Figure 20 illustrates the relative difference in efficiency transfer computations when the attenuation parameter of the sample material is increased or decreased by 5 % at all energies. Data are given for three different sample thicknesses (20 mm, 60 mm and 80 mm). The sample and detector models utilized in these computations are as described in paragraph 2.1.

As depicted in the figure, the relative difference tends to increase with sample thickness and decrease with increasing energy. Above 100 keV, the relative difference remains below 2 %. However, at energies below 100 keV, the highest relative difference is observed at 20 keV, reaching approximately 5 %. This value is comparable to the variation applied to the attenuation coefficients.

Furthermore, it is noteworthy that at the lowest energies, the variation of the relative difference as a function of sample thickness is less pronounced compared to intermediate and high energies. Based on these observations, we conclude that efficiency transfer for typical laboratory samples is primarily influenced by the uncertainty in the attenuation data at low photon energies, resulting in a relative deviation comparable to the deviation observed in the attenuation data.
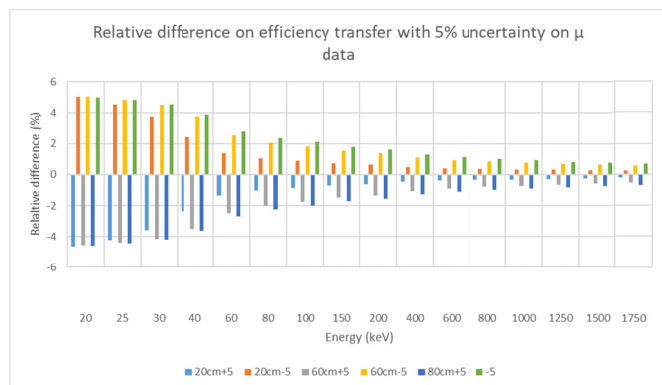
Figure 20: Relative difference of efficiency transfer when attenuation data is varied with 5%.

4. Conclusion

A method was outlined to experimentally determine attenuation coefficients at photon energies in the range 13.0 keV – 302 keV using an uncollimated beam of gamma- and X-rays emitted from transmission sources. The method relies on calibrations performed by measuring count rates of photon transmission through specific materials in a well-defined geometry measured at various transmission energies and their correlation with the attenuation coefficients. The attenuation data for all these materials were obtained from the XCOM database.

In the proposed method, the attenuation data are acquired relative to the data of water, which acts as the reference sample material (calibration) for efficiency transfer. Efficiency transfer is employed to correct for sample self-attenuation in the analysis of low-energy gamma-rays or X-rays using the measured attenuation parameters.

Efficiency transfer factors are computed to determine the actual counting efficiency of the sample being analyzed, referencing a calibration of efficiency obtained with a water matrix. To accomplish this, the attenuation data obtained at different transmission energies from a separate measurement are employed to replace the attenuation data in the material file used by EFFTRAN. By incorporating the experimentally determined attenuation data, the efficiency transfer accounts for the specific characteristics of the sample material in the analysis.

The method achieves an accuracy on the order of 5% for the low-energy (< 100 keV) attenuation data and efficiency transfer factors for assay of typical laboratory samples. The level of accuracy depends on the quality of the calibration curves, the difference in attenuation properties compared to water. The method may fail when the transmission spectra strongly interfere with fluorescence X-rays produced by the sample material when irradiated by transmission photons.

We also discussed that at low energy the correction of sample self-attenuation may be influenced by coherent scattering. Attenuation data that are measured and later on used in sample self-attenuation correction should be used in a consistent way. Attenuation data in XCOM also have an uncertainty and at low-energy these are of the order of a few percent.

References

Berger M.J., H. J. (2010). *XCOM: Photon Cross Sections Database NIST Standard Reference Database (XGAM)*. Retrieved from https://physics.nist.gov/PhysRefData/Xcom/html/xcom1.html

Berger, M. H. (2010). XCOM: Photon Cross Section Database. *NIST STandard Reference Database*, na. Retrieved from http://www.nist.gov/pml/data/xcom/

Byun J., Y.-Y. J. (2015). A calibration transmission method to determina the gamma-ray linear attenuation coefficient without a collimator. *Applied Radiation and Isotopes, 102*, 70-73.

Cramer S.N., K. B. (1989). *The effect of coherent scattering in photon radiation transport calculations.* ORNL/RSIC-51.

Cutshall, N. (1983). Direct analysis of 210Pb in sediment samples: Self-absorption corrections. *Nucl.Instrum.Methods, 206*, 309-312.

Degrelle D., M. C.-E. (2016). Determination of mass attenuation coeficient by numerical absorption calibration with Monte-Carlo simulations at 59.54 keV. *Nuclear instruments and Methods in Physics Research Section A: Accelerators, SPectrometers, Detectors and Associated Equipment, 816*, 47-52.

ESM Ali, S. B. (2015). Towards a quantitative measurement based estimate of the uncertainty in photon mass attenuation coefficients at radiation therapy energies. *The journal Phys. Med. Biol.*, 1641-1654.

Iurian, e. a. (2018). Self-attenuation corrections for Pb-210 in gamma-ray spectrometry using well and coaxial HPGe detectors. *Applied Radiation and Isotopes, 134*, 151-156.

Jodlowski, P. (2016). A revision factor to the Cutshall self-attenuation correction in Pb-210 gamma-spectrometry measurements. *Applied Radiation and Isotopes, 109*, 566-569.

Lee J.B., B. J. (2020). Mass attenuation coefficients of environmental samples for gamma-ray energies from 46.5 keV to 1408 keV. *International Journal of Radiation Research, 18*(2), 201-207.

Morrison, F. A. (2014). *Obtaining Uncertainty Measures on Slope and Intercept of a Least Squares Fit with Excel's LINEST.* Houghton: Michigan Technological University.

Saloman E.B., H. J. (1986). X-ray Attenuation Coefficients (Total Cross Sections): Comparison of the Experimental Data Base With the Recommended Values of Henke and the Theoretical Values of Scofield for Energies Between 0.1-100 keV. *NBSIR*, 86-3431.

Sima O., A. D. (2001). GESPECOR: A versatile tool in gamma-ray spectrometry. *Journal of Radioanalytical and Nuclear Chemistry, 248*(2), 359-364.

Sima, O. ,. (2002). Transfer of the efficiency calibration of Germanium gamma-ray detectors using the GESPECOR software. *Applied Radiation and Isotopes, 56*, 71-75.

Vidmar, T. (2005). EFFTRAN A Monte Carlo efficiency tranfer code for gamma-ray spectrometry. *Nucl. instrum. Methods, 550*, 603-608.

Initial Gamma Spectroscopy of ITER Material Irradiated in the JET D-T Neutron Environment

C.L. Grove[a*], C.R. Shand[a], L.W. Packer[a], N. Fonnesu[b], E. Łaszyńska[c], S. Loreti[b], J.W. Mietelski[d], M. Pillon[b], M.I. Savva[e], I.E. Stamatelatos[e], A.Turner[a], T. Vasilopoulou[e], R. Villari[b], A. Zohar[f] and JET contributors[†]

[a] United Kingdom Atomic Energy Authority, UK
[b] ENEA – Department of Fusion and Technology for Nuclear Safety and Security via E. Fermi 45, 00044 Frascati, Italy
[c] Institute of Plasma Physics and Laser Microfusion, Poland
[d] Institute of Nuclear Physics, Polish Academy of Sciences, Poland
[e] Institute of Nuclear and Radiological Sciences, Technology, Energy and Safety, NCSR Demokritos, Greece
[f] Reactor physics division, Jožef Stefan Institute, Slovenia

Abstract

During operations with deuterium and tritium in the Joint European Torus (JET), 11 materials used in the construction of the International Thermonuclear Experimental Reactor (ITER) were irradiated. This work presents gamma spectrometry results of 17 ITER material activation foils measured by UKAEA and compares identified radionuclides with those predicted by nuclear inventory code calculations. The radionuclides detected broadly agree but indicate two additional impurities of iron, and silver or cadmium in the CuCrZr through the identification of Mn–54 and Ag-110m.

Keywords: Activation foils, JET, ITER, nuclear fusion, gamma spectroscopy

1. Introduction

As part of the EUROfusion Preparations for ITER Operations (PrIO) programme, within the 'ACT' sub-project, 27 functional materials used in the main components of the International Thermonuclear Experimental Reactor (ITER) tokamak and 4 different dosimetry foil materials were irradiated within the Joint European Torus (JET) tokamak neutron environment during operations with deuterium and tritium undertaken in 2021 (DTE2 and C40a&b campaigns). A total of 68 ITER material foils and 21 dosimetry foils were placed in a long-term irradiation station (LTIS) assembly close to the JET vacuum vessel. These irradiated foils were extracted and distributed to several European labs for gamma spectrometry measurements. This analysis aimed to identify and accurately assess the activity of radionuclides present. This work presents the latest gamma spectrometry results of the 17 ITER material foils measured by the Radiological Assay and Detection Laboratory (RADLab), UKAEA. The data obtained from these irradiated ITER materials provide insight into the neutron-induced radionuclides that ITER will generate in the nuclear phase. The activity measurement results from UKAEA are presented and compared with initial simulated predictions from nuclear inventory calculations to help indicate impurities present in the ITER materials.

2. Retrieval of ACT Holder

The activation foil holder shown in Fig. 1, known as the ACT holder, consisted of 26 channels each 2 mm thick. Each channel was filled with 0.5 mm thick activation foils, thinner foils, or VERDI detectors. A VERDI (Novel Neutron Detector for Fusion) detector is a stack of multiple activation foils housed in a graphite case used to determine the neutron fluence and energy spectrum at the irradiation position. The VERDI project is outside the scope of this paper but is discussed further in (Savva, et al., 2023). The 4 dosimetry foil materials (Titanium, Iron, Cobalt, and Yttrium) were selected based on known nuclear reactions that would occur in them, which could be used to characterise the irradiation received at the LTIS through techniques such as neutron spectrum unfolding. The results from measurements of these dosimetry foils

will be studied in future work and are not considered in this paper. The 17 ITER materials focussed on in this report were all approximately 0.5 mm thick with diameters varying between 10 mm and 18 mm. The materials and physical properties of the 17 ITER materials measured by UKAEA are shown in Table 1 and their elemental compositions of the ITER materials can be found in (Packer, et al., 2021).

(a) Holder pre-irradiation   **(b)** Holder post-irradiation
Fig. 1: Photo of the ACT holder pre- and post-irradiation

The foils and holder were irradiated during JET's D-T campaign between August and December 2021, the prior and following T-T campaigns, and the clean-up D campaign. During the D-T campaign, the LTIS was irradiated with 14.1 MeV neutrons at a fluence ranging $4.7 - 5.3 \times 10^{15}$ cm^{-2} and the highest instantaneous neutron flux was approximately 2×10^{-13} cm^{-2} s^{-1}. After the D-T irradiation, the LTIS was allowed to decay until the dose rate had sufficiently reduced, in accordance with health physics requirements, to retrieve the holder from the irradiation positions on 25th September 2022. The ACT holder was packaged into a shielded drum, in order to reduce the external dose rate to a level lower than 3 μSv h^{-1}, and was transferred to the Materials Research Facility (MRF) at UKAEA to a dedicated controlled area where the foil samples were extracted. The contact dose rate external to the ACT holder was measured using a Ludlum Model 26-1 handheld detector and was 660 μSv h^{-1}. This value was in agreement with the value of 673±75 μSv h^{-1} predicted by FISPACT-II inventory code (Fleming, Stainer, & Gilbert, 2018)

and used to guide in health and safety of the extraction operation. Once extracted the activated foils were placed into labelled bags and packaged into separate parcels for distribution to the labs involved in the project, including ENEA, IPPLM, IFJ, and NCSRD. The radiation dose on the outside of each package meant that each parcel could be shipped as exempt.

Table 1: List of ITER materials foils irradiated in DTE2 and their physical properties that were measured by UKAEA.

ITER Material	Material	Mass (g)	Thickness (mm)	Diameter (mm)	Density (g cm^{-3})
ITER 1	SS316L (N) -vv plate (Industeel)	0.923	0.52	18.00	6.98
ITER 2	SS316L (N) - vv plate (R. Kind)	0.924	0.52	18.00	6.98
ITER 3	SS316L (N) - vv plate (Thyssen)	0.922	0.52	18.00	6.97
ITER 4	SS316L (N) - TF radial plate 2500/64	0.880	0.50	18.00	6.92
ITER 5	SS316L (N) - TF radial plate 2500/68	0.890	0.51	18.00	6.86
ITER 10	Alloy 660 - divertor	0.926	0.47	18.00	7.74
ITER 12	CuCrZr divertor pipe 212601	0.961	0.51	18.00	7.41
ITER 13	CuCrZr divertor pipe 212606	0.890	0.47	18.00	7.44
ITER 14	Tungsten	0.705	0.49	10.00	18.32
ITER 16	Divertor XM-19	0.910	0.52	18.00	6.88
ITER 17	Divertor XM-19	0.915	0.52	18.00	6.92
ITER 18	Inconel 718	0.963	0.49	18.00	7.72
ITER 19	Eurofer 97-3	0.357	0.51	11.00	7.37
ITER 20	Eurofer 97-3	0.501	0.51	13.00	7.40
ITER 21	Divertor Al-Bronze	0.855	0.50	18.00	6.72
ITER 23	SS304 - In-wall shield	0.881	0.51	18.00	6.79
ITER 26	Alloy 660 - In-wall shield A286	0.924	0.52	18.00	6.98

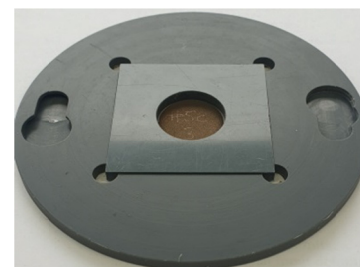## 3. Gamma Spectroscopy Measurements

Gamma Spectroscopy measurements were carried out using foils in a sample holder put on the endcap of a broad energy high-purity Germanium (BEGe) detector with Compton suppression system (CSS) as shown in Fig. 2a. The BEGe (S/N: b13135) detector was cooled by liquid nitrogen within a Canberra Cryo-Cycle cooling system, and it is equipped for data acquisition with a Lynx digital MCA device connected to a PC with Genie2000 software for analysis. The CSS consists of 6 NaI detectors with data also recorded by a Lynx digital MCA and set up to veto coincidence events in both the BEGe and a NaI, so reducing the Compton continuum in the spectrum. The measurements were carried out between 20/10/2022 and 04/11/2022 using various measurement times. The standard measurement time was 24 h. Tungsten (ITER#14), Inconel 718 (ITER#18), and Eurofer 97-3 (ITER#19) were considered important materials to investigate so they were prioritised for weekend-long measurements of 65 h or 66 h. Whereas several stainless-steel foils (ITER#1, ITER#2, ITER#4, and ITER#5) and a duplicate Alloy 660 sample (ITER#10) were measured for shorter periods of 4 h to 6 h.

The analysis software, Genie2000, is an advanced gamma spectrometry software where energy and efficiency calibrations are applied, allowing for quantitative analysis of gamma spectra. An energy calibration was performed before the measurements using a traceable mixed radionuclide source, certificated by Deutschen

Kalibrierdienst (DKD), containing gamma-emitting radionuclides with emission energies ranging across the spectrum from 59 keV to 1836 keV. The mixed radionuclide source contains Co-57, Co-60, Sr-85, Y-88, Cd-109, Sn-113, Cs-137, Ce-139, Hg-203, and Am-241 with activities referenced to 12:00 UTC on 1st January 2016 with relative expanded (k=2) uncertainty of 3% (but 5% for Cd-109).
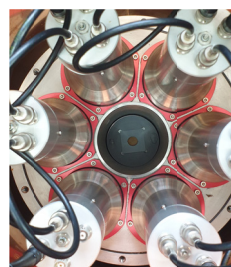
(a) Sample on detector endcap   **(b)** Measurement sample holder

Fig. 2: Photos of a sample in position for a measurement on the endcap of the detector in the sample holder.

Efficiency calibrations of the ITER materials were performed using a source-less approach using In Situ Object Counting System (ISOCS) geometry models with the sample on the detector endcap. Note that efficiency calibrations are only in reference to the quantitative results from the BEGe and not the qualitative measurements from the CSS. To confirm the accuracy of the efficiency correction an ISOCS geometry of the mixed radionuclide source was made and activity analysis was performed on an energy calibration measurement with results compared to the source reference activity at the date 01/01/2016 12:00T. Since the measurement was performed on the detector's endcap, a coincidence summing correction was applied when calculating the activities. Of the five radionuclides (Co-57, Co-60, Cd-109, Cs-137, Am-241) identified in the mixed radionuclide source, they all had measured activities within the uncertainty of the source reference activity. These results show that the ISOCS geometry model produces an accurate efficiency correction across the spectrum. An ISOCS geometry for efficiency correction was generated for each of the 17 ITER materials, which were measured in a sample holder for ease of retrieval from the BEGe as shown in Fig. 2b. The ISOCS models accounted for the foil dimensions, masses, materials, and sample holder.

The material definitions used for the ISOCS models were based on the ITER material certificates that were obtained when the bulk materials were purchased from Goodfellow (Goodfellow, 2023). These generally included a breakdown of elements present in the material along with any measurable impurities. A breakdown of the material composition can be found in (Packer, et al., 2021). The smallest impurity by percentage weight varies across the ITER materials ranging from 0.0001% and 0.01%. The certificates also gave a range of values that each element in the compositions could take, and for this paper, the compositions used were based on the upper bounds. The composition ranges and weaker impurities than measured might contribute to the activation and result in radionuclides present in the gamma spectrum that would not be predicted by inventory codes such as FISPACT-II. Therefore, it would be advantageous to conduct composition measurements on the ITER materials that would both confirm the certificates and identify any other impurities in the materials. This work was not performed for this paper but it is planned in future through techniques such as Wavelength-Dispersive X-ray Spectroscopy (WDS) and Atom Probe Tomography (APT). The ISOCS geometry composer used was not capable of making material definitions that encompass all elements in ITER material certificates. Specifically,

ITER materials with more than 14 elements; including Eurofer 97-3 (ITER#19 and ITER#20), SS304 [In-wall shield] (ITER#23) and Al-Bronze Divertor (ITER#26). For these materials, approximation materials were created using the 14 most dominant elements. This meant that elements totalling a weight percentage of 0.132%, 0.0506%, and 0.0211% for Eurofer 97-3, SS304 [In-wall shield], and Al-Bronze Divertor were not included in the ISOCS geometries for efficiency corrections. It is not thought that these missing minor elements would cause a significant difference to the efficiency correction.

4. Results and Discussion

An example gamma spectrum from one of the ITER materials, ITER#18 Inconel 718, is shown in Fig. 3 where peaks corresponding to identified radionuclides were marked. The figure shows the effect of the CSS on a measured spectrum, where a reduced Compton continuum has revealed additional peaks and more clearly distinguished others. For example, the peaks originating from Cr-51, Fe-59, and Nb-95 were identified in the raw BEGe spectrum but are clearer in the CSS spectrum, which gives additional confidence that the peak is present and can be correctly used for activity determination. Many of the peaks that are not labelled in Fig. 3 can be attributed to pile-up summing events caused by the intense 122 keV Co-57 peak. For example, the 4 unlabelled peaks between 900 keV and 1000 keV originate from a sum of the peaks from 122 keV Co-57 and the 4 labelled peaks between 800 keV and 900 keV, and the unlabelled peak at 1320 keV which corresponds to a summation of Co-58 peaks (810 keV and 511 keV annihilation peak). In some materials such as CuCrZr peaks in the CSS allowed for the identification of additional radionuclides, such as Zr-95 for ITER#12 and Mn-54 for ITER#13, which could not be observed from a BEGe spectrum alone. However, the CSS also removed one radionuclide from the spectrum. Ag-110m was identified in the BEGe but its peaks were not present above the Compton continuum in the CSS spectrum. The reason for this is that the cascade of gamma-ray emission from Ag-110m, with transitions of the order of picoseconds, is too fast for the CSS to deal with it appropriately and so Ag-110m gamma-rays were vetoed incorrectly as Compton scattering events. This highlights the importance of ensuring that the coincidence timing window is long enough to remove Compton events, but not too long to avoid removing radionuclides with a fast emission cascade and this was not possible for Ag-110m. The CSS editing of the spectrum is one reason activity analysis was performed using BEGe-only data.

The activity results from radionuclides identified in the BEGe spectra calculated using Genie2000 with efficiency correction using the ITER material ISOCS models are shown in Table 2. The activity results have been decay corrected to the end of the JET DTE2 campaign at 21:53 on 21/12/2021 where the majority of irradiation had been received by the activation foils. Since the measurements were undertaken on the detector endcap, a coincidence summing correction was also performed as part of Genie's inbuilt cascade correction algorithm, which uses total efficiencies calculated from the ISOCS models. The correction factors varied across the radionuclides and their emission lines but ranged from 0.153 to 1.037. The activities are given as specific activities in Bq g^{-1} using the masses given in Table 1, with the associated standard uncertainties (k=1). Where radionuclides were not identified but were included in the nuclide library used for analysis their minimum detectable activity (MDA) is given alongside a less-than sign. The nuclide libraries used in the analysis were made based on radionuclides predicted from the FISPACT-II nuclear inventory code calculations used to aid the health and safety of extraction along with other radionuclides identified by studying the unknown peaks in the spectra.
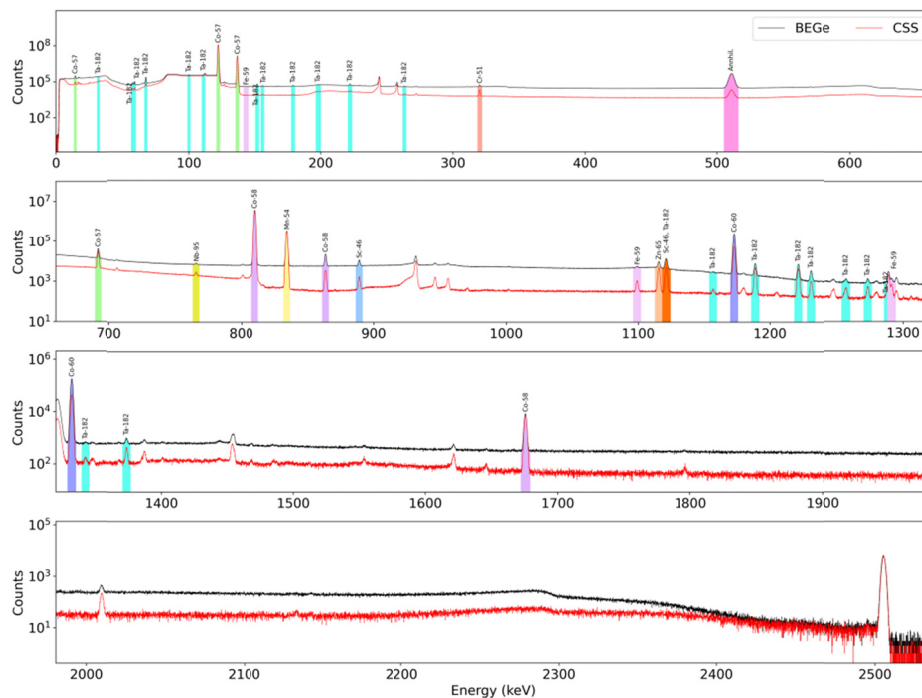

Fig. 3: Spectrum of Inconel 718 (ITER#18) measured by the BEGe and CSS with identified nuclides peaks labelled.

Table 2: Activities results calculated from the measurements performed on the BEGe detector, decay corrected to the end of the JET DTE2 campaign (21/12/2021 21:53), and cascade corrected by Genie2K's inbuilt analysis routine using ISOCS total efficiencies.

ITER Material	Total Activity (Bq g^{-1})	Radionuclide Activity (Bq g^{-1})						
		Sc-46	Cr-51	Mn-54	Fe-59	Co-57	Co-58	Co-60
ITER#1	2.38x10^5	n/a	(195±16)x10^3	(5.4±0.3)x10^3	514±22	(9.0±0.5)x10^3	(26.6±0.9)x10^3	198±6
ITER#2	2.32x10^5	n/a	(190±15)x10^3	(5.3±0.3)x10^3	436±21	(9.1±0.5)x10^3	(26.9±0.9)x10^3	171±5
ITER#3	2.22x10^5	n/a	(180±15)x10^3	(5.5±0.3)x10^3	490±19	(8.8±0.5)x10^3	(26.3±0.8)x10^3	217±6
ITER#4	2.34x10^5	n/a	(193±16)x10^3	(5.1±0.3)x10^3	438±24	(8.6±0.5)x10^3	(26.6±0.9)x10^3	167±5
ITER#5	2.41x10^5	n/a	(197±16)x10^3	(5.5±0.3)x10^3	484±24	(9.3±0.5)x10^3	(27.3±0.9)x10^3	181±5
ITER#10	2.47x10^5	328±12	(170±14)x10^3	(4.5±0.3)x10^3	512±30	(18±1)x10^3	(53±2)x10^3	468±13
ITER#12	1.02x10^4	n/a	(8.8±0.8)x10^3	1.2±0.1	n/a	3.1±0.2	26±2	783±22
ITER#13	8.72x10^3	n/a	(7.2±0.7)x10^3	<0.516	n/a	0.37±0.04	<5.08	765±22
ITER#14	2.99x10^5	n/a	n/a	0.29±0.02	n/a	2.1±0.2	1.5±0.2	0.94±0.03
ITER#16	2.80x10^5	<2.73	(235±19)x10^3	(9.7±0.6)x10^3	427±16	(8.8±0.5)x10^3	(25.6±0.8)x10^3	181±5
ITER#17	2.70x10^5	<2.78	(226±18)x10^3	(9.4±0.6)x10^3	456±17	(8.5±0.5)x10^3	(25.3±0.8)x10^3	178±5
ITER#18	3.40x10^5	138±8	(181±15)x10^3	958±58	529±19	(41±2)x10^3	(114±4)x10^3	665±19
ITER#19	1.14x10^5	n/a	(107±9)x10^3	(4.9±0.3)x10^3	702±26	14±1	41±3	7.5±0.3
ITER#20	1.20x10^5	n/a	(109±9)x10^3	(5.0±0.3)x10^3	774±30	11.5±0.9	30±3	7.3±0.3
ITER#21	1.61x10^4	<4.36	<2.53x10^3	455±27	<47.0	(4.0±0.2)x10^3	(10.9±0.4)x10^3	707±20
ITER#23	2.38x10^5	n/a	(196±16)x10^3	(4.2±0.3)x10^3	496±19	(9.5±0.5)x10^3	(27.4±0.9)x10^3	186±5
ITER#26	2.42x10^5	343±12	(161±13)x10^3	(4.6±0.3)x10^3	509±19	(19±1)x10^3	(56±2)x10^3	312±9

Table 2 continued: Activities results calculated from the measurements performed on the BEGe detector, decay corrected to the end of the JET DTE2 campaign (21/12/2021 21:53), and cascade corrected by Genie2K's inbuilt analysis routine using ISOCS total efficiencies.

ITER Material	Radionuclide Activity (Bq g^{-1})							
	Zn-65	Zr-95	Nb-95	Ag-110m	Ta-182	Hf-181	W-181	W-185
ITER#1	50±2	<22.6	491±50	n/a	<3.46	n/a	n/a	n/a
ITER#2	52±2	<24.4	637±64	n/a	<3.67	n/a	n/a	n/a
ITER#3	47±2	<14.7	597±47	n/a	<2.11	n/a	n/a	n/a
ITER#4	47±3	<30.6	566±74	n/a	<4.39	n/a	n/a	n/a
ITER#5	52±2	<29.3	616±67	n/a	<4.39	n/a	n/a	n/a
ITER#10	39±2	<37.8	<349	n/a	<5.53	n/a	<5.24	n/a
ITER#12	25±1	<10.8	514±37	3.4±0.2	22.3±0.6	n/a	n/a	n/a
ITER#13	20±1	22±2	680±47	1.9±0.1	<6.58	n/a	n/a	n/a
ITER#14	13.5±0.6	n/a	n/a	n/a	140±2	56±3	(91±5)x10^3	(208±21)x10^3
ITER#16	44±2	<13.5	556±42	n/a	73±1	n/a	<2.43	n/a
ITER#17	42±2	<14.0	528±42	n/a	71±1	n/a	<2.05	n/a
ITER#18	58±3	<11.3	848±57	n/a	532±8	n/a	<2.38	n/a
ITER#19	55±2	n/a	n/a	n/a	(1.09±0.02)x10^3	n/a	303±43	n/a
ITER#20	47±2	n/a	n/a	n/a	(5.26±0.07)x10^3	n/a	<10.5	n/a
ITER#21	44±2	<12.1	<106	n/a	<1.12	n/a	<1.08	n/a
ITER#23	53±2	<14.4	<129	n/a	<2.12	n/a	n/a	n/a
ITER#26	38±2	<14.5	345±36	n/a	<2.23	n/a	<2.07	n/a

A detailed study quantitatively comparing the activity of the measured radionuclides from the ITER materials with those expected from FISPACT-II calculations will be conducted in the future. This will focus on supplying ITER with knowledge that can be used to understand how activate their construction materials will become during ITER's deuterium and tritium operations and highlight any impurities that might be of concern to them. An initial assessment will be discussed here that compares the radionuclides measurements with those expected from the FISPACT-II calculations. The FISPACT-II calculations were performed using TENDL2019 (Koning, et al., 2019). A breakdown of this is given in Table 3, which shows the radionuclides that were both measured and predicted by FISPACT-II, predicted by not measured, and measured but not initially expected based on the FISPACT-II calculations. The radionuclides measured in Table 3 take into account radionuclides that were identified from either the BEGe or CSS spectra. Note that the FISPACT-II calculations used in this report were initial scoping calculations with the primary purpose of predicting the total activity of the ACT irradiation holder so that a

date for extraction from the JET LTIS could be safely selected. Therefore, these FISPACT-II calculations are not as rigorous as they will be for the quantitative investigation as they do not use the full irradiation schedule experienced by the LTIS but only the D-T campaign, and may not have used the most accurate material definitions with all known impurities for the ITER materials.

There were a few radionuclides, namely Sc-46, Fe-59, Hf-181, W-181 and W-185, where there was an agreement between measurements and predictions across all of the ITER materials. Most of these align with the fact that these radionuclides were not included in the analysis libraries where they were not expected. For example, Hf-181 and W-185 were only included in the tungsten library, but there was no evidence of their peaks in the other material spectra. Cr-51, Co-56, Y-91, Zr-95, and Nb-95 were radionuclides that were expected in more foils than they were measured but not measured in any material where they were not predicted. This does necessarily mean that these nuclides were not present in the foils but that the activity was less than the MDA so could not be measured. The reason that the activity might be below

the MDA is jointly caused by the short half-life of these nuclides compared with the time that had passed post-irradiation and a potentially low number of reactions producing these nuclides. For example, 302 days had passed since the end of D-T irradiation and the start of the CuCrZr ITER#12 measurement where Y-91 ($t_{1/2}$ = 58.51 days) would have passed through 5 half-lives. Additionally, the dominant production reaction pathway is Zr-91(n,p)Y-91, and since the percentage weight of Zr in CuCrZr is 0.15% and the abundance of Zr-91 in zirconium is 11.22% means that the initial number of Y-91 nuclide there were produced was likely low as well.

Table 3: List of ITER materials foils irradiated in DTE2 and analysed by UKAEA, along with the nuclides measured that were also predicted by FISPACT-II (green), not predicted (blue), and predicted but not measured (orange).

(Legend for table cells: G = green (measured & predicted); B = blue (measured, not predicted); O = orange (predicted, not measured); blank = no colour)

ITER Material	Material	Sc-46	Cr-51	Mn-54	Fe-59	Co-56	Co-57	Co-58	Co-60	Zn-65	Y-91	Zr-95	Nb-95	Ag-110m	Ta-182	Hf-181	W-181	W-185
ITER#1	SS316L(N) – vv plate (Industeel)		G	G	G		G	G	G	B					O			
ITER#2	SS316L(N) – vv plate (R. Kind)		G	G	G		G	G	G	B					O			
ITER#3	SS316L(N) – vv plate (Thyssen)		G	G	G		G	G	G	B					O			
ITER#4	SS316L(N) – TF radial plate		G	G	G		G	G	G	B								
ITER#5	SS316L(N) – TF radial plate		G	G	G		G	G	G	B					O			
ITER#10	Alloy 660 – divertor	G	G	G	G		G	G	G	B			G					
ITER#12	CuCrZr divertor pipe 212601		G	B			B	B	G	B	O	G	G		B			
ITER#13	CuCrZr divertor pipe 212606		G	B			B	B	G	B	O	G	G		B			
ITER#14	Tungsten Monoblock			B			B	B	B	B					G	G	G	G
ITER#16	Divertor XM-19		G	G	G		G	G	G	B					O			
ITER#17	Divertor XM-19		G	G	G		G	G	G	B					O			
ITER#18	Inconel 718		G				G	G	G	B			G		G			
ITER#19	Eurofer 97-3			G	G					B					G			G
ITER#20	Eurofer 97-3			G	G					B					G			G
ITER#21	Divertor Al-Bronze		O	G	O		G	G	G	G								
ITER#23	SS304- In-wall shield		G	G	O		G	G	G	B			G					
ITER#26	Alloy 660 – In-wall shield A286	G	G	G	G		G	G	G	B			G					

For the other radionuclides, Mn-54, Co-57, Co-58, Co-60, Zn-65, Ag-110m and Ta-182, there was at least one ITER material where the radionuclide was identified despite not being expected from FISPACT-II calculations. The most notable nuclide identified was Zn-65, which was only expected in the Al-Bronze foil (ITER#21) due to its small 0.016% zinc content, however, Zn-65 was measured in every ITER material. One explanation for this comes from a surface contaminant deposited during the cutting process rather than a material impurity. The foils were cut from bulk materials using electrical discharge machining, thus the brass wire used likely deposited zinc and copper onto the surface of each foil. The foils were not polished to remove surface contaminates before loading into the irradiation sample holder. Therefore, any deposited zinc on the surface was also irradiated in JET leading to the production of nuclides such as Zn-65. Further experimental testing using techniques such as WDS on cut foils will be performed to confirm this hypothesis, but it is suggested that future irradiations should be conducted on activation foils that have been polished after being cut.

The Co-60 was measured but not expected in the tungsten foil (ITER#14), which might also be explained through brass surface contamination, having a possible production reaction of Cu-63(n,α)Co-60. However, given that Mn-54, Co-57 and Co-58 were also identified in the tungsten foil, which cannot be explained by production routes from brass, it is likely that at least part of the Co-60 also had another origin. In materials that do not contain cobalt, these manganese and cobalt activation product radionuclides are typically a result of neutron-induced reactions with iron and nickel, such as Fe-54(n,p)Mn-54, Ni-58(n,np)Co-57, Ni-58(n,p)Co-58, and Ni-60(n,p)Co-60. Despite the tungsten foil being predominantly (99.97%) made of tungsten, both iron and nickel are stated impurities within the material with maximum weight percentages of 0.0002% and ≤0.005% respectively according to the material certificates. The FISPACT-II calculation used a material definition of 100% tungsten for this foil so any activation from impurities would not be accounted for. When quantitative analysis between the measurements and FISPACT-II calculations is carried out this foil calculation will be performed again to capture all information possible for an accurate comparison.

Mn-54, Co-57 and Co-58 were also measured in the CuCrZr (ITER#12 and ITER#13) despite not being expected by FISPACT-II calculations, for a similar reason. FISPACT-II calculations were performed using a material definition that only included copper chromium and zirconium. The material certificates include impurities of cobalt, niobium, and tantalum. A cobalt impurity can explain the presence of Co-57 and Co-58, which would have been produced via the reactions Co-59(n,3n) and Co-59(n,2n). Performing FISPACT-II calculations again with an accurate CuCrZr material definition will be conducted to access whether the cobalt impurity leads to a comparable activity of Co-57 and Co-58. However, the Mn-54 activation product cannot be explained by these impurities since the exotic reactions, such as Co-59(n,2n+α)Mn-54, required have thresholds of >14 MeV generated by D-T fusion reactions. Therefore, there might be a previously unknown iron impurity in the CuCrZr that is not accounted for by the material certificate. WDS or APT measurements on CuCrZr will be conducted to confirm this.

In the case of Ta-182, in addition to being detected in the tungsten (ITER#14) and Eurofer 97-3 (ITER#19, ITER#20) foils where it was expected, it was also identified in CuCrZr (ITER#12), XM-19 (ITER#16, ITER#17) and Inconel 718 (ITER#18) where it was not expected, whilst not being measured in the SS316L (N) – vv plate (ITER#1, ITER#2, ITER#3) foils where Ta-182 was expected. Ta-182 has two production routes in the tungsten and Eurofer 97-3 samples, from tantalum via the reaction Ta-181(n,γ)Ta-182 and from tungsten via the reactions W-182(n,p)Ta-182 and W-183(n,np)Ta-182. However, since the other ITER materials with measured Ta-182 do not have a tungsten component the only production route available is Ta-181(n,γ)Ta-182. The three SS316L (N) – vv plate foils have tantalum components with stated maximums of 0.01%, 0.008%, and 0.0031% respectively. With such small tantalum components, any activity present from Ta-182 is likely at a level where it is not detectable, i.e. <MDA. ITER#12, ITER#16, ITER#17, and ITER#18 have comparable maximum tantalum components by percentage weight of 0.01%, 0.01%, 0.01%, and 0.05% respectively, but Ta-182 was identified in the spectra of these materials. One main reason for this is the longer measurement time used for these samples resulting in lower MDAs. ITER#1, ITER#2 and ITER#3 were measured for 6 h, 6 h, and 18 h, whereas ITER#12, ITER#16 and ITER#17 were measured for 24 h, and ITER#18 were measured for 66 h. As stated above the FISPACT-II calculations were performed using a material definition of CuCrZr that did not contain the tantalum impurity, which might explain why Ta-182 was not predicted. This is also the case for XM-19 and Inconel 718 where some of the minor impurities including tantalum

were not in the material definitions used for the FISPACT-II calculations.

The final radionuclide, Ag-110m, was only identified in the CuCrZr spectra but was not expected and cannot be explained by impurities listed in the material certificates that were not included in the FISPACT-II calculations. Therefore, the presence of Ag-110m suggests that there is another impurity in CuCrZr. Since the foils underwent neutron-induced activation, the two most likely elemental impurities are silver and cadmium through reactions such as Ag-109(n,γ)Ag-110m or Cd-110(n,p)Ag-110m. If cadmium was the impurity, the only other long-lived gamma-emitting nuclide that might also have been produced is Cd-109. However, Cd-109 only has a weak gamma emission at 88 keV with 3.6% intensity and the abundance of seed nuclide Cd-108 is only 0.888% so the number of Cd-109 nuclides that will have been produced might be <MDA. If silver was the impurity, one might expect Ag-108m to also be produced. Ag-108m does have gamma lines with high intensity but with a half-life of 438 years, it is not easily detectable within the period of the 24 h measurement. Therefore, at the current stage, there is not enough information to say whether the impurity is cadmium or silver. There are a few techniques planned to yield further information on this impurity from WDS and APT to further measurements. The additional measurement will specifically focus on the better determination of the Ag-110m activity and potentially revealing the presence of Ag-108m by dissolving part of the foil in nitric acid before precipitating out AgCl and conducting a measurement for a long time on a low background spectrometer.

5. Conclusion

In conclusion, 67 ITER materials and 21 dosimetry activation foils were irradiated in JET during the recent D-T, T-T and clean-up D campaigns. The activation foils were extracted from the LTIS and distributed to several European labs for gamma spectrometry measurements. 17 ITER material foils were retained by UKAEA for measurements and their activities were determined. A qualitative comparison between the radionuclides identified by the gamma spectroscopy and those expected through FISPACT-II nuclide inventory code calculations was carried out. In general, most of the expected radionuclides were present in the ITER materials although there were a few exceptions. Some of the weaker activity radionuclides expected such as Co-56 and Y-91 were not detected in any sample, while others such as Cr-51, Zr-95, Nb-95 and Ta-182 were not identified in every spectrum they were expected. These radionuclides were not measurable above the MDA due to a combination of their short half-lives in comparison to the time after irradiation that the measurements were conducted, and a low number of the nuclides being produced given the small reaction rate and low content of the seed nuclide in the material.

There were also some nuclides detected that were not predicted by FISPACT-II calculations. Most of these, such as Mn-54, Co-57, Co-58, Co-60 and Ta-182, appear to be a result of the FISPACT-II calculations not accounting for minor impurities in the samples. Quantitative analysis will perform the FISPACT-II calculations again with material definitions that include these impurities. However, Mn-54 cannot be explained through the missed impurities in the CuCrZr foils suggesting there is another unknown impurity of iron in the material. Ag-110m was also identified in the CuCrZr spectra, which was not expected and indicated that there is either a silver or cadmium impurity in the material. Further experiments are planned to determine if the material does contain silver. Zn-65 was predicted in one of the 17 ITER materials measured but was detected in all of them. This was attributed to a brass surface contaminant on the foils resulting from the electrical discharge machining used to cut the foils. Future irradiations in JET will test this hypothesis but grinding some of the samples after they have been cut to remove any surface contaminants.

References

Fleming, M., Stainer, T., & Gilbert, M. (2018). *The FISPACT-II User Manual.* Culham Science Centre: UKAEA-R(18)001.

Goodfellow. (2023). Retrieved from https://www.goodfellow.com/

Koning, A., Rochman, D., Sublet, J.-C., Dzysiuk, N., Fleming, M., & van der Marck, S. (2019, January). TENDL: Complete Nuclear Data Library for Innovative Nuclear Science and Technology. *Nuclear Data Sheets, 155*, 1-55. doi:https://doi.org/10.1016/j.nds.2019.01.002

Packer, L. W., Batistoni, P., Bekris, N., Bradnam, S. C., Fabbri, M., Ghani, Z., . . . JET Contributors. (2021, October). Technological exploitation of the JET neutron environment: progress in ITER materials irradiation and nuclear analysis. *Nuclear Fusion, 61*(11), 116057. doi:10.1088/1741-4326/ac2a6b

Savva, M. I., Bradnam, S. C., Vasilopoulou, T., Nobs, C. R., Mergia, K., Packer, L. W., . . . JET Contributors. (2023, June). Application of VERDI detectors for ITER materials activation product inventory characterization. *Fusion Engineering and Design, 191*, 113559. doi:https://doi.org/10.1016/j.fusengdes.2023.113559

Preparation of Cs-137 Sources from Nuclear Fuel Element Plate U$_3$Si$_2$/Al Post Irradiation for Calibrating Nuclear Instruments

Gatot Wurdiyanto[a], Aslina Br. Ginting[b], Yanlinastuti[b], Hermawan Candra[a], Boybul[b], and Erlina Noerpitasari[b].

[a] Research Center for Safety, Metrology, and Nuclear Quality Technology – Indonesian National Research and Innovation Agency (BRIN)
[b] Research Center for Nuclear Fuel Cycle and Radioactive Waste Technology – Indonesian National Research and Innovation Agency (BRIN)

Abstract

The spent fuel elements contain some radioisotopes with a very high level of radioactivity, and half-lives greater than 10 years that may have a high enough economic value for recovery, especially ^{137}Cs. The separation method of ^{137}Cs was carried out by the cation exchange using Lampung zeolite. The preparation of the ^{137}Cs-zeolite was carried out gravimetrically using a calibrated semi-micro balance. There were 15 point sources and 4 extended volume sources in vials containing zeolite with ^{137}Cs incorporated in the zeolite matrix. Activity and impurity measurements were carried out using gamma spectrometry. The measured specific activity value of ^{137}Cs was 84.3 Bq/g with an expanded uncertainty of 3.4%, at k=2. Validation was carried out by comparison with ^{137}Cs standard solutions. There were not siqnificant difference between standard solutions of ^{137}Cs and ^{137}Cs-zeolite.

Keywords: Spent fuel, ^{137}Cs, cation exchange, Lampung zeolite.

* Corresponding author, e-mail address: gatot.wurdiyanto@brin.go.id

5. Introduction

From 2002, the Multi-Purpose Reactor G.A. Siwabessy (RSG-GAS) in Serpong, Indonesia uses U$_3$Si$_2$/Al type fuel with a density of 2.96 gU/cm^3 for the Material Testing Reactor (MTR) type. U$_3$Si$_2$/Al fuel with an enrichment of 19.75% was irradiated at RSG-GAS with a burn up by 56% and produced several fission and activation products together with heavy elements such as ^{137}Cs, ^{134}Cs, ^{90}Sr, ^{235}U, ^{238}U, ^{234}U, ^{236}U, ^{239}Pu, and ^{148}Nd (Kim J.S.. et. al, 2015). After allowing for short-lived radionuclides to decay for $\geq$101 days, the U$_3$Si$_2$/Al fuel is sent to the Radiometallurgical Installation (IRM) hot cell for post irradiation examination. The post-irradiation tests aim to determine the performance of nuclear fuel during irradiation at RSG-GAS. These tests include determination of the strength of the AlMg$_2$ cladding, the stability of the fuel cladding and the compatibility of the fuel and the fuel cladding. The post-nuclear fuel irradiation tests consist of non-destructive tests (defects, dimensions, swelling) and damage tests (metallographic analysis to observe microstructure, and physico-chemical analysis to determine burn-up). The post-irradiation test data is then used as feedback to the RSG-GAS to determine the performance of the fuel and to the fabricator to evaluate the optimisation of fabrication parameters in developing the fuel. In addition to knowing the performance of the fuel, the burn-up data obtained from destructive testing is used to prove the suitability of the burn-up data calculated using the Origen software program by RSG-GAS. The amount of burn up may not exceed the limits set by the Regulatory Agency (BAPETEN and IAEA) for the safe operation of the RSG-GAS, currently 56% (Report of Safety Analysis (Indonesian), 2021).

The determination of post-irradiation U$_3$Si$_2$/Al fuel burn-up was carried out through physicochemical analysis by cutting the fuel plates, dissolving it with 6M HNO$_3$ and 6M HCl. Meanwhile, the separation caesium from uranium is carried out by cation-anion exchange method. Physicochemical analysis aims to determine the content of the isotopes ^{137}Cs and ^{235}U in the fuel formed through nuclear fission during reactor operation. The type of isotope that can be used as an indicator of burn-up, the most widely used of which is the ratio of ^{235}U burned (U_i) to the initial ^{235}U (U_o) or the ratio (U_i/U_o). The original ^{235}U isotope (U_o) is the ^{235}U content present in nuclear fuel at the time of manufacture. In addition to the ratio (U_i/U_o), the ratio ^{134}Cs/^{137}Cs is also often used as an indicator to burn up (Peng Hong Lim, et al, 2013). The basis for selecting the ^{134}Cs/^{137}Cs ratio as an indicator of burn up is because ^{134}Cs and ^{137}Cs are isotopes that are in the region of the majority of the gamma (Iγ) intensities, have a small (σ) neutron absorption profile and have a long half-life (T$_{1/2}$) of 30.018 years (Aslina and Liem, 2015, Be, et al, 2006).

Lampung zeolite is one of the natural products in Indonesia originating from the Lampung province of Indonesia. The Lampung province, especially the area of Campang Tiga, and Talang Baru have total zeolite resources of 127 million tons consisting of a measured resource of 27 million tons and an inferred resource of 100 million tons. Natural zeolite is a hydrated aluminum silicate compound, with the main elements consisting of alkaline and alkaline earth cations. This compound has a three-dimensional structure and has pores that can be filled with water molecules. The use of zeolite is widespread, and it is found in diverse products such as industrial raw materials, in water treatment, liquid waste cleaners, the agricultural, livestock, fisheries, cosmetic, pharmaceuticals and others. In this study Lampung Zeolite was used to separate the radioactive material caesium from various other materials.

The development of nuclear medicine techniques in Indonesia is very rapid. More than 100 dose calibrators are owned by around 20 hospitals in Indonesia. Dose calibrators need a standard source for routine quality checks to ensure consistency and relative accuracy. Due to price and other procurement issues, mos hospitals do not have standard sources for quality checks. Their dose Calibrators are only calibrated once a year to the national reference laboratory, PTKMR-BATAN.

The Secondary Standard ionization chamber of the PTKMR-BATAN is a Capintec CRC-7BT radionuclide calibrator that is used as a working chamber for the routine dissemination of the activity standards for photon emitting radionuclides. The calibrator is subject to regular quality checks to ensure consistency and relative accuracy, using standard sources from National Metrology Institutes (NMIs), namely the National Measurement Institute of Japan (NMIJ), the Physikalisch-Technische Bundesanstalt (PTB), and the National Institute of Standards and Technology, NIST).

This paper describes the procedures used to separate the caesium in spent fuel U_3Si_2/Al post irradiation, measure the activity of ^{137}Cs-zeolite, and the results of the measurements used to calibrate the radionuclide calibrator. The volume of ^{137}Cs-zeolite used was 5 ml, 10 ml, 15 ml, and 20 ml because this is the volume most often used in hospitals. The vials used are made by Wheaton, USA and are made of borosilicate glass, with a volume of 20 ml, height of 55 mm, outer diameter of 30 mm, and thickness of 1 mm.

6. Experiment and methodology

2.1. Separation of ^{137}Cs in post-irradiation PEB U_3Si_2/Al solution

Post irradiation U_3Si_2/Al density 2.96 gU/cm^3 fuel element plate (PEB) was cut in the middle with dimensions of 3×3×1.37 mm or the equivalent weight of 0.056 g PEB, then dissolved using 5 ml of 6 M HCl and 5 ml of 6M HNO₃. This dissolution technique produces 10 ml of U_3Si_2/Al fuel solution containing fission isotopes such as ^{137}Cs, ^{235}U and ^{239}Pu isotopes. The U_3Si_2/Al fuel solution was prepared in a hot cell, and 1 ml aliquot of this solution is taken from the bulk solution and removed from the hot cell, diluted to 20 ml with 0.1M HCl. After homogenising the solution, 50 µl aliquots of the solution were placed in a vial of 1 g of Lampung zeolite. Cation exchange between the solution and the zeolite was carried out by stirring for 1 hour using a shaker with a speed of 1000 rpm, and left for 24 hours so that the solid phase was separated from the liquid phase. The results of the cation exchange process were that caesium isotopes were bound to zeolite in the form of Cs-zeolite as the solid phase while ^{235}U and other isotopes remained in the aqueous phase as is shown in Fig 1.
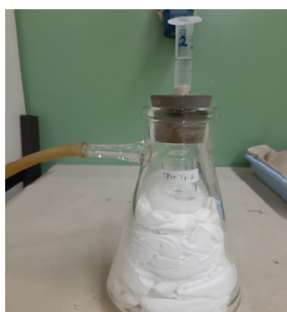
Fig. 1: The process of separating ^{137}Cs with a cation exchange column using Lampung zeolite.

2.2. Preparation of ^{137}Cs-zeolite sources

All the relevant equipment was cleaned with diluted alcohol, then ^{137}Cs-zeolite sources were prepared gravimetrically using semi-micro balance. The balance was calibrated by the Indonesian NMI for weighing, and the level of readability of the balance is 0.1 mg. Two types of samples were made: (a) 15 point sources, and (b) 5 ml, 10 ml, 15 ml, and 20 ml sources in vials. All sources are derived from the same master sample. The point sources had a sample diameter of about 4 mm, with an approximate weight of ~1 g. After drying under a heat lamp for about 30 minutes, they were then covered with a film of Mylar with a ± 25 µg/cm^2 thickness. The samples had measured activities between 1–400 kBq. The density of the ^{137}Cs-zeolite was measured at 2.3 g/ml.

2.3. Measurement by gamma spectrometer

The gamma spectrometry was used to measure the activities of point sources. The detector is an HPGe model GEM20-70-LB-C (Ortec, USA), which has a relative efficiency of 20% with an energy resolution of ≤ 1.8 keV FWHM at 1332.5 keV . The detector is equipped with a model DSPEC-LF Digital Spectrometer with MAESTRO Software and DIM-POSGE Detector Interface Module, and operates at a bias voltage of + 4200 V. The source-to-

detector distance was 25 cm. As described above, the gamma-ray spectrometry system was first calibrated using standard sources of ^{152}Eu, ^{60}Co and ^{137}Cs that have traceability to the SI. Three sets of measurement were made with a counting time of 120 minutes in each case. Impurities and homogeneity of samples were also checked using gamma spectrometry.

Fig. 2: ^{137}Cs-zeolite in various volume

2.4. Measurement by ionization chamber radionuclide calibrator.

Vial samples were measured using the Capintec radionuclide calibrator in two ways: firstly with the predefined calibration factor corresponding to the ^{137}Cs button on the activity calibrator and secondly using the dial setting determination method. Pre-set push buttons are provided for the quick selection of the calibration number of commonly used radioisotopes. There are eight pre-set push buttons on this model that were used in this study. One of the remaining buttons was calibrated for ^{137}Cs in zeolite material as part of this work. It is important to note that the calibration settings for the Capintec chambers are defined only for measurements of solutions in a standard NIST ampoule. Thus, the calibration settings for each radionuclide and geometry need to be determined individually. The determination of the appropriate dial settings of this work was achieved using the technique described by Zimmerman and Cessna (2000). The ratio, R, of the activity measured with the special button on the standard activity, is determined after the gamma spectrometry activity results are known. The ratio R is given by $R = A_{std}/A_{cap}$ where A_{std} is the

activity of standard source and A_{cap} is the activity measured by the Capintec radionuclide calibrator. This R value can be used directly as a calibration factor for the ^{137}Cs when the special button or a calibration setting number is used.

3. Results and discussion

The result of the efficiency calibration of the HPGe detector using ^{152} Eu, ^{60}Co and ^{137}Cs standard sources is shown in Fig. 3. The energies used to produce the efficiency calibration curve were 244.7, 344.3, 661.657, 778.9, 964.1, 1112.1, 1173.228, 1332.492 and 1408.0 keV (Be, et al, 2004), resulting in a curve described by the equation efficiency at energy, $\varepsilon = 0.2851\ (E)^{-0.959}$, with E given in keV, correlation coefficient 0.9998. The uncertainty of the interpolated efficiency at any point is 1.5% at k=1. This value was determined from the residuals between the true efficiencies and the efficiencies obtained from the efficiency curve

There was no significant impurity detected above 0.05% of the ^{137}Cs activity. The counting time for each sample was 120 minutes. The results of the activity determinations of the ^{137}Cs-zeolite are shown in Table 1. These values are from the specific activity values of ^{137}Cs obtained from gamma spectrometry and the masses of the 5 ml, 10 ml, 15 ml, and 20 ml samples in the vials. These results have expanded uncertainties of 3.4 % at k=2.
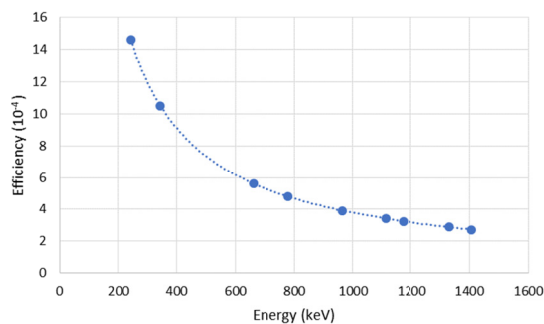
Fig. 3: Efficiency calibration curve using ^{152}Eu, ^{60}Co, and ^{137}Cs standard sources.

Previously, we had measured the activity of ^{137}Cs in brown rice for participating in international comparison of activity. Fig. 4 is the result of our laboratory measurement (PTKMR-BATAN) when participating in an international comparison of activity measurement of ^{137}Cs and ^{134}Cs in brown rice. In this comparison, we prepared the calibration source of rice spiked with ^{134}Cs and ^{137}Cs using the same containers and filling them with the same amount of rice as that of the samples. From the success in this comparison, we tried to source standard ^{137}Cs in various matrices, in this case ^{137}Cs in a zeolite matrix.
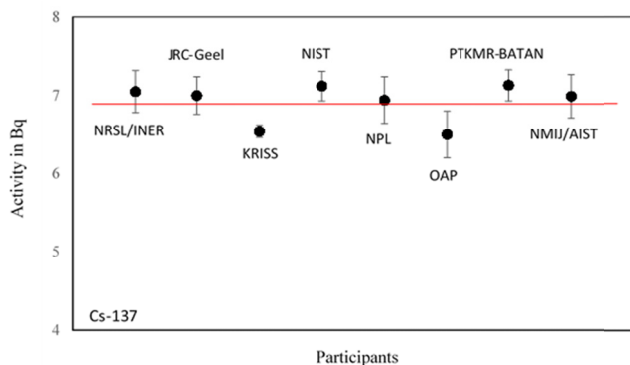
Fig. 4: Laboratory results of the international comparison of activity measurement of ^{137}Cs in brown rice (A. Yunoki, et al.,2023).

Table 1: Activity of ^{137}Cs-zeolite samples base on gamma spectrometry measurements.

Volume (ml)	Activity (Bq)	Uncertainty (%) (k=2)
5	970,000	3.4
10	1,939,000	3.4
15	2,909,000	3.4
20	3,880,000	3.4

As a validation, a comparison of the calibration value was carried out using a source of ^{137}Cs-zeolite with a standard source of ^{137}Cs solution. Differences in the values of the correction factors using standard sources of ^{137}Cs solution and ^{137}Cs-zeolite for various volumes are shown in Table 2. In the Table 2, shown that there was no significant difference between the calibration factor values obtained using the ^{137}Cs zeolite source and the standard of ^{137}Cs solution. The highest difference between the two types of standard source is around 2.6%, namely for the hospital's dose calibrator with a 15 ml of volume.

Table 2: Difference of R value of some instruments using ^{137}Cs standard source solution and ^{137}Cs-zeolite in vials.

Volume (ml)	Instruments	R value	
		^{137}Cs std sol.	^{137}Cs zeolite
5	Cap. CRC-7BT	1	1.02
	Cap CRC-712M	1.03	1.05
	Hospital Rad.Cal.	1.16	1.13
10	Cap. CRC-7BT	1	1.01
	Cap CRC-712M	1.02	1.05
	Hospital Rad.Cal.	1.17	1.15
15	Cap. CRC-7BT	1	1.01
	Cap CRC-712M	1.03	1.04
	Hospital Rad.Cal.	1.12	1.09
20	Cap. CRC-7BT	1	1.01
	Cap CRC-712M	1.03	1.04
	Hospital Rad.Cal.	1.11	1.09

The uncertainty components for the R-value determined for the gamma-ray spectrometer are shown in Table 3. The uncertainty components for the R-value determined for the Capintec CRC-7BT radionuclide calibrator are shown in Table 4. The uncertainty components for the R-value determined for the hospital radionuclide calibrator are shown in Table 5.

Table 3: Uncertainty components for the R-value determined for gamma-ray spectrometer for ^{137}Cs-zeolite.

Source of uncertainty	Std. uncert. components (%)	
	Type A	Type B
Standard sources		0.5
Half life of Standard		0.12
Efficiency		1.5
Intensity of sample		0.235
Half life of sample		0.0998
Area of sample	0.59	
Dead Time		0.05
Quadratic sum	0.35	2.58
Combined standard uncertainty	1.7	
Expanded uncertainty (k=2)	3.4	

Table 4: Uncertainty components for the R-value determined for Capintec CRC-7BT radionuclide calibrator for ^{137}Cs-zeolite.

Source of uncertainty	Std. uncert. components (%)	
	Type A	Type B
Cal.fact. for gamma spect. Syst.		1.7 (not incl.)
Half life of ^{137}Cs-zeolite		0.0998
Statistic counting	0.6	
Detector response		1.155
Accuracy of reading		1.732
Repeatabiity		0.577
Non linearity		0.35
Mass		0.05
Diff.of gravimetry to volumetric		1
Quadratic sum	0.36	5.80
Combined standard uncertainty	2.5	
Expanded uncertainty (k=2)	5.0	

Table 5: Uncertainty components for the R-value determined for hospital radionuclide calibrator for ^{137}Cs-zeolite

Source of uncertainty	Std. uncert. components (%)	
	Type B	Type B
Cal.fact. for gamma spect. Syst.		1.7
Cal.fact. for Capintec rad cal.		2.5
Nonlinear. for Capintec rad cal.		0.35
Stability of rad cal		0.4
Sample mass		0.05
Sample volume		0.1
Half life of ^{137}Cs-zeolite		0.0998
Statistic counting	0.50	
Quadratic sum	0.25	9.4
Combined standard uncertainty	3.1	
Expanded uncertainty (k=2)	6.2	

4. Conclusions

Preparation of ^{137}Cs source of Nuclear Fuel Element Plate U_3Si_2/Al post-irradiation had been carried out by the cation exchange method using Lampung zeolite. Standardization of ^{137}Cs-zeolite was carried out by gamma spectrometry. The degree of homogeneity of ^{137}Cs-zeolite is below 1.5%. The activity values had a combined uncertainty of 1.7% at k=1. The results were used to calibrate the PTKMR secondary standard ionization chamber. The calibration factor values were not significantly different between using ^{137}Cs solution and ^{137}Cs-zeolite. A ^{137}Cs-zeolite source can be used as a calibrator source and a quality control for nuclear medicine equipments in Indonesia

Acknowledgements

References

Aslina B.G., Liem P.H., 2015. Absolute burnup measurement of LEU silicide fuel plate irradiated in the RSG GAS multipurpose reactor by destructive radiochemical technique. Annals of Nuclear Energy, 85, 613-620.
https://doi.org/10.1016/j.anucene.2015.06.016

Bé, M.-M., Chisté, V., Dulieu, C., Browne, E., Chechev, V., Kuzmenko, N., Helmer, R., Nichols, A., Schönfeld, E. and Dersch, R., 2004. Table of Radionuclides (Volume 2 – A=151 to 242). BIPM Monographie BIPM-5, Bureau International des Poids et Mesures, Sèvres.
https://www.bipm.org/en/publications/monographies

Bé, M.-M., Chisté, V., Dulieu, C., Browne, E., Baglin, C., Chechev, V., Kuzmenko, N., Helmer, R., Kondev, F., MacMahon, D. and Lee, K.B., 2006. Table of Radionuclides (Volume 3 – A=3 to 244). BIPM Monographie BIPM-5, Bureau International des Poids et Mesures, Sèvres.
https://www.bipm.org/en/publications/monographies

BIPM, IEC, IFCC, ILAC, ISO, IUPAC, IUPAP and OIML, 2008. Evaluation of measurement data – Guide to the expression of uncertainty in measurement, JCGM 100:2008.
https://www.bipm.org/documents/20126/2071204/JCGM_100_2008_E.pdf/

CRC-7BT Radioisotope Calibrator Owner's Manual, 1993. Capintec, Inc., Pittsburgh, USA

Kim, J. S., Young, S.J., Soon, D.P., Ha, Y.-K. and. Sung, K., 2015. Analysis of high burnup pressurized water reactor fuel using uranium, plutonium, neodymium, and cesium isotope correlations with burnup. Nuclear Engineering Technology, 47(7), 924-933.
https://doi.org/10.1016/j.net.2015.08.002

Liem, P.H., Amini, S., Hutagaol, H.G. and Sembiring, T.M., 2013. Nondestructive burn-up verification by gamma-ray spectroscopy of LEU silicide fuel plates irradiated in the RSG GAS multipurpose reactor, Annals of Nuclear Energy, 56, 57–65.
https://doi.org/10.1016/j.anucene.2013.01.013

Report of Safety Analysis (Indonesian), Instalasi Radiometalurgi No. 001.001/KN 00 01/BBN 5. Pusat Teknologi Bahan Bakar Nuklir, Badan Tenaga Nuklir Nasional (2021).

Yunoki, A., Miura, T., Sato, Y., Lee, P.-F., Hult, M., Tzika, F., Lutter, G., Marissens, G., Lee, J.-M., Lee, K.B., Nour, S., La Rosa, J., Saegusa, J., Soodprasert, T., Candra, H., Holnisar, Marsoem, P., Wurdiyanto, G., Hamamatsu, S. and Hachinohe, M., 2023. APMP supplementary international comparison of activity measurement of Cs-134 and Cs-137 in brown rice. Metrologia, 60(1A), 06007. https://doi.org/10.1088/0026-1394/60/1A/06007

Zimmerman, B.E., Cessna, J.T., 2000. Experimental determinations of commercial 'dose calibrator' setting for nuclides used in nuclear medicine. Applied Radiation and Isotopes 52, 615–619.
https://doi.org/10.1016/S0969-8043(99)00219-5

Appendix

ICRM 2023 Conference papers published in Applied Radiation and Isotopes (Virtual Special Issue ICRM 2023), ISSN 0969-8043

Session: Aspects of International Metrology

Maria Sahagia, Herceg-Novi summer school, the starting point in the history of the International Committee for Radionuclide Metrology,
https://doi.org/10.1016/j.apradiso.2023.111097... Volume 203, 2024

Romain Coulon, Monica Aguiar Leobino da Silva, Emma Bendall, Denis E. Bergeron, Christophe Bobin, Ivana Bonková, Angus H.H. Bowan, Broda Ryszard, Marco Capogni, Mauro Capone, Pierluigi Carconi, Philippe Cassette, T. Cessna Jeffrey, Emily L. Clark, Sean Collins, Sammy Courte, Marek Czudek, Carlos José da Silva, Johnny de Almeida Rangel, Pierino De Felice, Fuyou Fan, Aldo Fazio, Ryan P. Fitzgerald, Carole Fréchou, Raphael Galea, Vincent Gressier, Akira Iwahara, Steven M. Judge, Christine M.B. Keevers, John Keightley, Karsten Kossert, Matej Krivošík, D.B. Kulkarni, Lizbeth Laureano-Perez, Edyta Lech, Anderson Leiras, Juncheng Liang, Paulo Alberto Lima da Cruz, Ronaldo Lins da Silva, Anna Listkowska, Haoran Liu, Meiling Liu, Joline Lubbe, Carine Michotte, Kimberly Moore, Ole Nähle, Manuel Nonis, Andy Pearce, Leticia Pibida, André L.L. Quadros, Natasha Ramirez, Anuradha Ravindra, Benoit Sabot, Paweł Saganowski, V. Sathian, Michael L. Smith, Ritu Sharma, Marcell P. Takács, Milton W. van Rooy, Robert Shearman, Martin J. van Staden, W.M. van Wyngaardt, Zhijie Yang, Melek Zarifi, Ming Zhang, Tomasz Ziemek, The international reference system for beta-particle emitting radionuclides: Validation through the pilot study CCRI(II)-P1.Co-60,
https://doi.org/10.1016/j.apradiso.2023.110945... Volume 200, 2023

Session: Quality Assurance and Proficiency Tests

W.M. van Wyngaardt, A.H.H. Bowan, E.L. Clark, C.M.B. Keevers, M.L. Smith, M. Zarifi, A. Stopic, Cross-validation of standardisation techniques at ANSTO using cobalt-60 and learnings from the presence and identification of non-gamma-ray emitting impurities,
https://doi.org/10.1016/j.apradiso.2023.111027 .... Volume 201, 2023

Ioana Lalau, Mastaneh Zadehrafi, Constantin Teodorescu, Mihail-Razvan Ioan, Andrei Antohe, Aurelian Luca, Performance evaluation of radon monitors at IFIN-HH, Romania,
https://doi.org/10.1016/j.apradiso.2023.111030... Volume 201, 2023

Hyun Su Lee, Sanghoon Hwang, Minji Han, Byoung-Chul Kim, Jong-Man Lee, Kyoung Beom Lee, Application of high-sensitivity radon monitor on walk-in type radon calibration chamber at KRISS,
https://doi.org/10.1016/j.apradiso.2024.111285... Volume 208, 2024

Session: Alpha- and Beta-Particle Spectrometry

A. Martín Sánchez, R. Mora Rodríguez, Measurement of the intensities of the long-range alpha particles from ^{212}Po, https://doi.org/10.1016/j.apradiso.2023.110953.. Volume 200, 2023

Xavier Mougeot, Atomic exchange correction in forbidden unique beta transitions,
https://doi.org/10.1016/j.apradiso.2023.111018... Volume 201, 2023

Session: Radionuclide Metrology Techniques

Marina F. Koskinas, Denise S. Moreira, Ione M. Yamazaki, Marcelo Colonno, Renato Semmler, Thales S.L. Morais, Mauro S. Dias, Primary standardization and Monte Carlo modeling of (^{243}Am + ^{239}Np) by means of a

Session: Gamma-Ray Spectrometry

Session: Measurement Standards and Reference Materials

Krasimir Mitev, Benoit Sabot, Sylvie Pierre, Marie-Christine Lépy, Philippe Cassette, Towards a radon-in-water primary standard at LNHB,
https://doi.org/10.1016/j.apradiso.2023.111013.. Volume 201, 2023

Y. Jung, S.H. Lee, M.J. Lee, Development of reference material for quality control of uranium analysis in marine sediments, https://doi.org/10.1016/j.apradiso.2023.110979... Volume 200, 2023

S.H. Lee, Y. Jung, M.J. Lee, C.H. Lee, Development of metal radioactive liquid reference material for proficiency test, https://doi.org/10.1016/j.apradiso.2023.110970... Volume 200, 2023

Denis E. Bergeron, Richard Essex, Svetlana Nour, Gordon A. Shaw, R. Michael Verkouteren, Ryan P. Fitzgerald, Gravimetric deposition of microliter drops with radiometric confirmation,
https://doi.org/10.1016/j.apradiso.2023.111025... Volume 201, 2023

D. Tüzün, L. Chambon, Y. Kergadallan, V. Lourenço, Novel production method for traceable surface sources by aluminium functionalisation,
https://doi.org/10.1016/j.apradiso.2023.111045... Volume 202, 2023

Session: Liquid Scintillation Counting Techniques

Philippe Cassette, Vladislav Todorov, Benoit Sabot, Strahil Georgiev, Krasimir Mitev, Uncertainties in TDCR measurement revisited: Contribution of optical effects,
https://doi.org/10.1016/j.apradiso.2023.110992... Volume 201, 2023

C. Bobin, C. Thiam, M.-D. M'Hayham, X. Mougeot, Activity standardization of ^{60}Co and ^{106}Ru/^{106}Rh by means of the TDCR method and the importance of the beta spectrum,
https://doi.org/10.1016/j.apradiso.2023.110993... Volume 201, 2023

R. Broda, T. Ziemek, J. Marganiec-Gałązka, M. Czudek, K. Kossert, A. Listkowska, E. Lech, Z. Tymiński, P. Saganowski, R. Coulon, C. Michotte, Measurement of the activity and determination of the half-life of ^{225}Ac at POLATOM, https://doi.org/10.1016/j.apradiso.2023.110987... Volume 201, 2023

R. Galea, K. Moore, Primary standardization and half-life determination of ^{225}Ac at NRC,
https://doi.org/10.1016/j.apradiso.2023.111105... Volume 203, 2024

Romain Coulon, Sammy Courte, Carine Michotte, Liquid scintillation counting of electrons from internal conversion for quantifying ^{109}Cd activity using a 3-photomultiplier tube system and a specific spectral unfolding, https://doi.org/10.1016/j.apradiso.2023.110882... Volume 199, 2023

Session: Nuclear Decay Data

L. Pibida, D.E. Bergeron, S.M. Collins, P. Ivanov, J.T. Cessna, R.P. Fitzgerald, J. Mewburn-Crook, B.E. Zimmerman, L. King, Absolute emission intensities of the gamma rays from the decay of ^{224}Ra and ^{212}Pb progenies and the half-life of the ^{212}Pb decay,
https://doi.org/10.1016/j.apradiso.2023.111171... Volume 205, 2024

Sylvain Leblond, DDEP re-evaluation of the radioactive decay scheme of ^{137}Cs,
https://doi.org/10.1016/j.apradiso.2024.111191... Volume 206, 2024

B.E. Zimmerman, A new evaluation of the decay data for ^{166}Ho,
https://doi.org/10.1016/j.apradiso.2024.111230... Volume 207, 2024

Denis E. Bergeron, Jeffrey T. Cessna, Ryan P. Fitzgerald, Gulakhshan Hamad, Lizbeth Laureano-Pérez, Leticia Pibida, Brian E. Zimmerman, Liquid scintillation efficiencies, gamma-ray emission intensities, and half-life for Gd-153, https://doi.org/10.1016/j.apradiso.2023.111108... Volume 203, 2024

Session: Low Level Radioactivity Measurement Techniques

International Committee for Radionuclide Metrology (ICRM)
Ljubljana, Slovenia, 2024

ICRM technical series on radionuclide metrology – ISSN 2522-4328
URL: https://physics.nist.gov/ICRM/ICRM_technicalseries_3.pdf

Title of this issue:
Proceedings of the 23rd International Conference on Radionuclide Metrology
and its Applications (ICRM 2023), March 26-31, 2023, Bucharest, Romania
Editors: Aurelian Luca, Brian Zimmerman and Denis Glavič-Cindro
2024

The International Committee for Radionuclide Metrology (ICRM) is an association of radionuclide metrology laboratories whose membership is composed of delegates of these laboratories together with other scientists (associate members) actively engaged in the study and applications of radioactivity.

It explicitly aims at being an international forum for the dissemination of information on techniques, applications and data in the field of radionuclide metrology. This discipline provides a range of tools for tackling a wide variety of problems in numerous other fields, for both basic research and industrial applications. Radionuclide metrology continues to play an important role in the nuclear industry, supporting activities such as radionuclide production, nuclear medicine, measurement of environmental radioactivity and of radionuclides in food and drinking water, decommissioning of nuclear facilities, nuclear security and emergency preparedness, nuclear physics research, etc.